ON PARTIALLY-AVERAGED NAVIER-STOKES TURBULENCE CLOSURES: IMPROVED NEAR-WALL STRATEGIES AND CHARACTERIZATION OF THREE-DIMENSIONAL WAKES

A Dissertation

by

CHETNA PRAKASH KAMBLE

Submitted to the Office of Graduate and Professional Studies of
Texas A&M University
in partial fulfillment of the requirements for the degree of

DOCTOR OF PHILOSOPHY

Co-Chairs of Committee,	Sharath S. Girimaji
	Hamn-Ching Chen
Committee Members,	Diego Donzis
	Prabir Daripa
	Freddie Witherden
Head of Department,	Sharath S. Girimaji

May 2021

Major Subject: Ocean Engineering

ABSTRACT

Challenges in turbulence modeling are often associated with a trade-off between accuracy of flow physics and computational effort. For complex industry-relevant flows, high computational costs require engineers to adopt statistical closures, e.g., Reynolds-averaged Navier-Stokes (RANS) models. These models, however, are unable to capture large-scale multi-point correlations in the flow. On the other hand, high fidelity simulations, e.g., large-eddy simulations (LES) and direct numerical simulations (DNS) are often associated with large computational effort and are currently limited to simple geometries at low Reynolds numbers. Scale-resolving simulations (SRS) have emerged in recent years as physics-based multi-point closures that provide 'accuracy-on-demand'. Partially-averaged Navier-Stokes (PANS) is a bridging-SRS strategy that offers computational accuracy ranging from RANS to DNS as a function of commensurate computational effort by specification of implicit filter parameters (f_k, f_ε). These filter parameters dictate the range of scales resolved in the turbulent flow thereby controlling the accuracy. The effect of unresolved scales on the resolved field is captured using two-equation turbulence closures, e.g. $k-\varepsilon$, $k-\omega$ models. This allows for the cut-off filter to be placed in inertial subrange and only dynamically relevant scales may be resolved reducing overall computational effort compared to LES. Thus, PANS models are well positioned to provide multi-fidelity simulations for numerous marine applications, specifically numerical wave tanks (NWTs). Two major challenges for application of turbulence models in accurate simulations of NWTs include efficient near-wall modeling and reliable representation of wakes. Therefore, this dissertation focuses on advancing the PANS strategy in: (i) near-wall closure and (ii) quantitative analysis of coherent structures in three-dimensional wakes.

The first study develops a PANS two-layer turbulence modelling approach. This closure aims to provide a simple and robust computational strategy to alleviate numerical challenges posed by steep gradients near-wall. This model allows for the near-wall region to be computed with one-equation model while the outer high-Re region is resolved with the PANS $k_u-\varepsilon_u$ model. This wall-resolved PANS (WR-PANS) two-layer model is analyzed in turbulent channel flow for

$Re_\tau = 180 - 950$. The results establish the model as an accurate and computationally feasible approach with inherent ease of application.

For bluff body wakes displaying multi-point coherence, it is imperative to ensure the reliability of coherent structures predicted by PANS simulations. In Study 2, a quantitative framework for assessment of the large-scales structures is proposed in the wake of a sphere at $Re = 3700$ using proper orthogonal decomposition (POD). The simulations are performed using a WR-PANS approach with the PANS $k_u - \omega_u$ closure for the unresolved scales. The results reveal that multi-point correlations in the resolved flow are accurately captured using WR-PANS closures.

In an effort to further reduce the computational burden of resolving the near-wall region, a wall-modeled PANS (WM-PANS) strategy is investigated in Study 3. This model allows for a spatially varying filter in order to compute the near-wall region using RANS and resolve the wake region using high-resolution PANS. The commutation residue arising from the spatial variation of filter parameter is systematically incorporated using energy conservation principle. The theoretical foundation and computational outcome of the model is examined in turbulent channel at $Re_\tau = 950$ and 8000. The model is further investigated in flow past a sphere at $Re = 3700$. The results are highly encouraging.

In the final study, the WM-PANS strategy is applied to flow over a sphere at very high Reynolds number, $Re = 1.14 \times 10^6$. The results further confirm that the WM-PANS strategy is a computationally efficient approach for simulating practical flows. Moreover, quantitative assessment of coherent structures based on the approach outlined in Study 2 demonstrates that reasonably accurate large scales are resolved in this supercritical regime using WM-PANS.

DEDICATION

To aai and her endless sacrifices in making all my dreams come true.

To baba and his unshakable faith in me.

CONTRIBUTORS AND FUNDING SOURCES

Contributors

This work was supported by a dissertation committee consisting of Professor Sharath S. Girimaji [advisor] of the Department of Ocean Engineering, Professor H. C. Chen [co-advisor] of the Department of Civil and Environmental Engineering and the Department of Ocean Engineering, Professor Diego Donzis of the Department of Aerospace Engineering, Professor Prabir Daripa of the Department of Mathematics and Professor Freddie Witherden of the Department of Ocean Engineering.

The analyses depicted in Chapter V were conducted in part by Dr. Pooyan Razi (currently at General Motors) and were published in his doctoral dissertation at Texas A&M University (2017).

All other work conducted for the dissertation was completed by the student independently.

Funding Sources

Graduate study was supported by teaching and research assistantships from the Department of Ocean Engineering at Texas A&M University and scholarships from American Bureau of Shipping and Barrett and Margaret Hindes Foundation.

TABLE OF CONTENTS

Page

LIST OF FIGURES

FIGURE Page

LIST OF TABLES

TABLE Page

1. INTRODUCTION

1.1 Motivation

Numerical Wave Tanks (NWTs) are emerging in recent years as front line computational tools for simulating nearly realistic conditions to study responses of structure in a 'single' or 'two-phase' fluid. These NWTs reduce the capital costs associated with physical wave tanks, along with reducing measurement noise and scaling effects [7]. However, a major challenge for NWTs is accurate modeling of multi-scale turbulence ubiquitous in flows and fluid-structure interaction (FSI) problems. In general, turbulence effects are important in: (i) wave-breaking [8] , (ii) wave-structure interaction [9], (iii) wave-current interaction [10], (iv) wind-wave interaction [11] and (v) wind-structure interaction [12]. Offshore environments are often subjected to complex wave–turbulence interaction, and wave overturning and breaking. Such cases can only be accurately represented by Navier–Stokes equations in conjunction with turbulence models [9]. High fidelity CFD simulations are essential to capture turbulence in the free surface, wave-breaking, wave-runup to evaluate extreme wave loading on offshore structures and survivability [13].

In a numerical towing tank, boundary layers developing on ship's superstructure and small-scales generated due to ship's propeller require high fidelity turbulence closures. Moreover, air wakes around ships in motion, maneuverability and seakeeping under strong winds, capsizing etc., necessitate accurate prediction of ship aero-hydrodynamics [14]. More recently, renewable energy sources, e.g., wave energy converters (WEC) and offshore wind farms have witnessed significant research interest. A recent study of WECs in a Numerical Wave Tank concluded that the turbulence models have a considerable influence on the modeled free surface elevation, the wave excitation forces, and the device dynamics [7]. Full-scale numerical simulations of wind farms in NWTs would require highly accurate turbulence models capable of dealing with spatio-temporal scales ranging from 1km to 1mm in the atmospheric boundary layers and even smaller in blade boundary layers [12]. High fidelity turbulence closures are also required to accurately simulate hydrodynam-

ics of floating offshore wind turbines which in turn affects the power output.

Historically, NWTs have been modeled based on potential flow theory with the assumption of an irrotational and inviscid fluid flow. These assumptions are valid for linear and weakly non-linear wave-structure interaction problems and therefore, are usually restricted to non-breaking waves in a calm marine environment [15]. To capture the highly non-linear phenomena of wave-breaking, green water and extreme body responses, CFD-based Numerical Wave Tanks (CNWTs) have been developed [13]. The effects of turbulence have mostly been modeled using Reynolds-averaged Navier-Stokes closures, e.g. RNG $k-\varepsilon$ model [16], $k-\omega$ model [17]. The attractiveness of RANS closures stem from their ease of application and low computational effort even though eddy-viscosity based turbulence models, e.g. $k-\varepsilon$ model tend to be highly diffusive [18]. Large-Eddy Simulations (LES) can also be employed but their application is limited due to excessive numerical resolution required [18]. Therefore, there is a clear need for multi-fidelity turbulence closures to accurately simulate multi-scale turbulence behavior at modest computational effort for NWTs. These variable resolution models can enhance the results by providing realistic environmental loading and accurate structural responses whilst being cost efficient.

1.2 Background

Along the lines of Occam's razor, Wilcox suggests [19]: *An ideal (turbulence) model should introduce the minimum amount of complexity while capturing the essence of relevant physics.* However, it would be remiss not to include the associated computational effort as a constraint. Therefore, an ideal model should not only claim ease of application but also must capture relevant flow physics in a computationally efficient manner.

Statistical closures, e.g., Reynolds-averaged Navier-Stokes (RANS) model the entire turbulence kinetic energy spectrum and only the averaged quantities are evolved in time. RANS methods have been the turbulence model of choice for scientists and engineers alike to simulate variety of complex industry relevant flows. Indeed, these models perform well in attached flows, however, predict sub-optimal behavior in flows with massive separation due to their inability to recover multi-point physics [20]. Although, some large-scale structure information maybe recovered using

unsteady RANS (URANS), their suppression of three dimensionality in turbulent wakes has been shown in numerous studies [21, 22].

Direct Numerical Simulations (DNS) resolve the entire turbulent kinetic energy spectrum down to the Kolmogorov scales. Therefore, DNS can capture flow physics accurately as dictated by mass (continuity) and momentum (Navier-Stokes) conservation laws. For DNS, the computational cost for simulating turbulent flows increases as $O(Re^{9/4})$. Therefore, a full-scale ship calculation at $Re = 10^9$ would require almost 10^{20} grid points [14]. For complex flows, the applicability of DNS given the current trends in computer hardware is for modest Reynolds numbers at best [23]. Large-Eddy Simulations (LES) on the other hand can resolve most of the energetic scales in the flow and model the scales in the dissipative range as stochastic turbulence. This alleviates the burden to resolve extremely small scales in the flow making LES strategy computationally attractive. However, for very high Reynolds number flows, it can be shown that the computational cost of a wall-resolved LES (WR-LES) can be comparable to DNS [24].

In recent decades, a new turbulence modeling strategy, Scale-resolving simulations (SRS) has garnered significant interest in turbulence modeling community. SRS models are a suite of high efficiency turbulence closure models wherein an optimal balance between accuracy and computational cost can be achieved. These models resolve flow features only on the key parts of the computational domain rendering them more accurate than the RANS closures. Moreover, SRS models can adapt a RANS-like behavior in the region of high computational requirement, e.g., near-wall, making them more computationally attractive than LES.

Scale-resolving simulations are broadly classified in two categories: (i) Zonal SRS (Z-SRS) methods and (ii) Bridging SRS (B-SRS) methods. Z-SRS methods use different turbulence models at different locations in the domain for a faster turn around time. e.g., DES [25], DDES [26] and XLES [27]. These models can adapt RANS like behavior in the regions where the computational solution is expensive (e.g. boundary layers) and regions of negligible impact on the solution (e.g. far-field boundaries). An important element of these models are interface conditions at the boundary of RANS and the high resolution region. This matching is achieved by introducing syn-

thetic turbulence based on the spatio-temporal scales from the RANS model [28]. Bridging-SRS methods include SAS [29], PITM [30] and PANS [31]. These models modify the parent RANS equations in order to resolve more scales in the turbulence flow field.

Partially-averaged Navier-Stokes (PANS) model is a bridging-SRS strategy, developed in Refs. [31, 32, 33, 34], that offers a seamless transition from RANS where all turbulent scales are modeled to DNS where entirety of the turbulence energy spectrum is resolved. PANS closure derives its form to a large extent from the corresponding RANS closures. Therefore, much of the physics incumbent in more advanced RANS models, e.g., realizability, tensor invariance, effects of rotation and buoyancy etc. can be translated directly to PANS [31]. In PANS, scales are resolved 'on-demand' by specification of implicit filter widths; f_k and f_ε. These filter widths modify the corresponding RANS coefficients in order to resolve the requisite range of scales in the flow.

For modeling the effects of unresolved scales, closure can be specified at different levels of sophistication. At the simplest level, a Boussinesq constitutive approximation for unresolved scales can be invoked based on averaging invariance principle [35]. In RANS, Boussinesq constitutive relationship is shown to be ineffectual in flows with sudden changes in mean strain rate, flows with curved surfaces, flows in rotating fluids etc.[19]. In such flows, non-linear constitutive relations [36], algebraic Reynolds stress models [37] or second moment closure (SMC) can be used. The PANS strategy developed from the two equation RANS closure can be extended to the aforementioned higher order closures [31]. However, as the majority of dynamically relevant scales are resolved in PANS, the severity of the deficiencies posed by the Boussinesq approximation for the unresolved scales is tempered. Moreover, adding complexities due to higher order closures in PANS can be counterproductive.

In LES, typically zeroth-order closures are used to model scales in the dissipative range. Higher-order closures in PANS permits the filter placement in the inertial subrange thereby reducing the overall computational effort compared to a conventional LES. Unlike LES, the PANS closures are in general decoupled from the numerical resolution. However, increasing the degree of resolution entails higher grid requirements [33]. Therefore, lowering the filter widths (f_k, f_ε)

increases the accuracy of the simulations (as more scales are resolved); however, it also increases the associated computational costs. Consequently, the choice of optimal filter parameters are often limited by the available computational resources. Nevertheless, PANS models pose less stringent grid requirements compared to LES and can provide higher accuracy than RANS models making them well suited for multi-fidelity turbulence simulations.

1.3 Progress in PANS modelling

Important advancements in the field of modelling using the PANS approach has been made in the last two decades. The following key points highlight the contributions made thus far:

1. **Theoretical Foundation:** The PANS closures as a function of implied cut-off have been systematically derived based on the theoretical framework incumbent in the parent RANS models. Fixed-point analyses are performed to ensure smooth transition from RANS to DNS with decreasing filter widths in the absence of underlying flow instabilities [34]. The physical fidelity of resolved fluctuations is characterized by adapting Kolmogorov hypothesis based on the paradigm that PANS is DNS of a non-Newtonian variable viscosity fluid [38]. It is shown that resolved fluctuations capture higher-order multi-point statistics and behave according to well-known turbulence scaling laws. The effect of spatio-temporal variation of filter is derived by carefully accounting for the commutation residue term using energy conservation principles [39, 40]. The turbulent transport coefficients have been derived based on equilibrium boundary analysis [41]. The framework for the choice of optimal f_k based on the underlying instabilities in the flow field has been developed in Ref. [42].

2. **Verification in benchmark test cases:** PANS closures have been extensively verified in variety of benchmark test cases. Computations of flow past a square cylinder [43, 44], circular cylinder [45, 46, 47], turbulent channel [40, 41] and backward facing step [48, 49] have been conducted. These test cases have served as a foundation for development of new PANS turbulence closures [50, 51].

3. **Application to industry relevant flows:** In recent years, PANS strategies have solidified

their position as an attractive tool to simulate highly complex practical flows at modest computational effort. Encouraging results have obtained in flow scenarios encountered across multiple disciplines: Aeronautics [52, 53, 54], Marine [55, 56], Internal combustion engines (ICE) [57] and renewable energy [58].

We now identify some outstanding issues which need to be addressed to improve the accuracy and efficiency further for use in NWT computations. In the next subsection we outline the key challenges currently facing PANS turbulence models.

1.4 Challenges

1. **Near-wall modeling:** The high Reynolds number simulations in complex flows warrant a cost efficient treatment of very thin boundary layers. The cost to resolve the small scales in the thin boundary layers can be exorbitant [24]. Moreover, steep gradients in these boundary layer can adversely effect the stability of turbulence modelling equations [59]. Although some near-wall closures have been developed in context of PANS [50, 51], the overarching challenge is to ensure both cost effectiveness and robustness of the modeling schemes. Study 1, 3 and 4 of this dissertation address this challenge.

2. **Fidelity of large-scale coherent structures:** Although numerous studies have commented on the ability of PANS in capturing large-scale coherent structures [45, 46], a thorough qualitative and quantitative assessment in the accuracy of these large-scale structure is warranted. Study 2 and Study 4 present a quantitative approach to characterize the large-scale structures in the flow.

Besides these, some other avenues which can further explored in order to enhance the robustness of PANS turbulence models include: identifying optimal f_k for complex flows, higher-order constitutive relationships and transition to turbulence.

1.5 Research objectives

This dissertation is focused toward achieving the following objectives:

1. Develop an accurate and computationally reasonable near-wall approach using a 'two-layer' modeling strategy for PANS,

2. Establish a mathematical framework for quantitative evaluation of coherent structures resolved in PANS for 3D bluff body wakes,

3. Evaluate the theoretical foundation of a wall-modeled PANS approach and,

4. Demonstrate the wall-modeled PANS approach in flow past a sphere in subcritical and supercritical Reynolds number regimes.

The following subsections present the synopsis of the studies performed in order to realize the aforementioned objectives.

1.5.1 Study 1: Two-layer near-wall modeling strategy for PANS closure

The objective of this study is to develop a two-layer PANS closure for improved near-wall simulation capability. In the RANS context, the two-layer turbulence model displays superior near-wall behavior compared with other closures of similar order. Our goal is to adapt these near-wall closure advantages to the PANS-SRS model. In the outer region of the PANS two-layer closure, a PANS $k-\varepsilon$ turbulence model is employed. In the inner layer, an unresolved kinetic energy equation is solved. The eddy viscosity and dissipation are specified using algebraic equations based on known scaling relationships. The proposed model is evaluated in a turbulent channel flow of friction Reynolds numbers in the range of $Re_\tau = 180 - 950$. Comparison with DNS data demonstrates that two-layer PANS is potentially an accurate and robust SRS approach.

1.5.2 Study 2: Characterization of large-scale coherent structures in turbulent wake of a sphere at $Re = 3700$

The large-scale coherent structures in the wake of a sphere at subcritical Reynolds number ($Re = 3700$) are examined at different degrees of resolution (filter size) using SRS. PANS-SRS method is employed to compute the wake flow at four levels of resolution marked by unresolved-to-total kinetic energy ratios: $f_k = 0.5,\ 0.3,\ 0.2,\ 0.1$. The results from the four simulations are used

to compute one-point statistics, frequency spectra and spatio-temporal Proper Orthogonal Decomposition (POD) modes. One-point statistics are reasonably well reproduced (in comparison with existing data) at all degrees of resolution. However, the frequency spectra and POD modes exhibit some degree of dependence on the level of resolution. It is demonstrated that accurate depiction of coherent structures is contingent upon adequately resolving key underlying instabilities. The finest resolution PANS simulation ($f_k = 0.1$) is then used to characterize the large-scale coherent structures in the near-wake of the sphere. The main features of this wake, specifically azimuthal mode shapes, modal energy and frequency content are compared with experiments and numerical simulations of wakes of other axisymmetric bodies resulting in good agreement. Overall, the study demonstrates that PANS can capture key one-point statistics and coherent structure features of complex flows in a cost-efficient manner.

1.5.3 Study 3: PANS closure modeling in near-wall region of steep resolution variation

We seek to investigate the closure model to enable SRS of a turbulent flow to optimally switch-over from RANS calculation at the wall to a specified degree of resolution in the wake or free-stream region. The closure model is derived (i) using the physical principle that the total energy of resolved and unresolved scales should be invariant independent of degree of resolution, and (ii) establishing consistency with equilibrium boundary layer (EBL) scaling of the partially resolved field. The resulting wall-modeled PANS (WM-PANS) is investigated in turbulent channel flow at $Re_\tau = 950$ and 8000. The influence of RANS-SRS switch-over location on the computed flow field is first examined. It is then demonstrated that the mean flow is reproduced quite accurately with modest computational effort without discernible log-layer mismatch. While the Reynolds stresses are also recovered accurately over most of the flow domain, a noticeable 'computational transition' from steady RANS to unsteady SRS flow behavior is observed and underlying physics is examined. Irrespective of the location of computational transition, the unsteady features of the flow away from the wall are well captured. The WM-PANS approach is used to simulate the wake of a sphere at $Re = 3700$. WM-PANS results are in excellent agreement with simulations of wall-resolved PANS (WR-PANS) performed at much finer resolution. Overall, the WM-PANS presents an accurate

and computationally viable option for scale resolving computations of near-wall high-Reynolds number flows.

1.5.4 Study 4: Wall-modeled PANS simulations of turbulent wake of a sphere at $Re = 10^6$

We investigate flow over a smooth sphere at high Reynolds number, $Re = 1.14 \times 10^6$ using the WM-PANS strategy. In WM-PANS, the turbulent boundary layer is computed using a RANS model whereas the scales in the unsteady turbulent wake region are resolved using uniform-f_k (physical resolution) PANS. The integral quantities, statistics and flow structures are investigated at different levels of freestream physical resolution: $f_{k(F)} = 1.00$ (RANS), $f_{k(F)} = 0.70$, $f_{k(F)} = 0.50$, $f_{k(F)} = 0.30$. The integral quantities are very well predicted by all the WM-PANS simulation compared to the numerical studies and the flow statistics converge reasonably beyond $f_{k(F)} \leq 0.50$. The large-scale coherent structures in the wake are examined using a POD approach. Qualitative comparison of the wake configurations in subcritical and supercritical regimes is also presented. Overall, this study demonstrates the efficacy of WM-PANS in capturing important flow features of high Reynolds number flows at modest computational effort.

1.6 Dissertation outline

This dissertation is organized into different chapters. Chapter 2 delineates the mathematical framework of PANS simulations. Chapter 3 presents the development of PANS two-layer modelling approach. The formulation, numerical parameters and results are presented for turbulent channel at different friction Reynolds numbers. This work has been published in the AIAA Journal 2020 [60]. Chapter 4 presents WR-PANS computations of flow past a sphere in the subcritical Reynolds number regime. The details of the POD approach to characterize the large-scale coherent structures in the wake is clearly laid out. This work is published in Physics of Fluids 2020 [61]. Chapter 5 presents the WM-PANS approach adopted to simulate turbulent channel at high Reynolds numbers and flow past a sphere in the subcritical regime. Chapter 6 deals with extension of the WM-PANS modeling strategy to high Reynolds number bluff body wakes. Summary and key conclusions of the studies are present in Chapter 7.

2. DESCRIPTION OF PARTIALLY-AVERAGED NAVIER-STOKES MODEL

The velocity and pressure fields in the incompressible flow regime are governed by the conservation of mass (continuity) and momentum (Navier-Stokes) equations:

$$\frac{\partial V_i}{\partial t} + V_j \frac{\partial V_i}{\partial x_j} = -\frac{\partial p}{\partial x_i} + \nu \frac{\partial^2 V_i}{\partial x_j \partial x_j}, \tag{2.1}$$

$$\frac{\partial V_i}{\partial x_i} = 0; \quad \frac{\partial^2 p}{\partial x_j \partial x_j} = -\frac{\partial V_i}{\partial x_j}\frac{\partial V_j}{\partial x_i} \tag{2.2}$$

Here, V_i and p represent the instantaneous velocity and pressure fields and ν is the fluid kinematic viscosity. In this research work, the directions 1, 2 and 3 refer to the streamwise x, wall-normal y and spanwise z directions respectively. The equations are solved in a Cartesian coordinate system and the dependence of velocity field on the radial (r) and azimuthal (θ) directions (for axisymmetric bodies) is obtained using the following coordinate transformation:

$$\begin{bmatrix} V_r \\ V_\theta \end{bmatrix} = \begin{bmatrix} cos(\theta) & sin(\theta) \\ -sin(\theta) & cos(\theta) \end{bmatrix} \begin{bmatrix} V_y \\ V_z \end{bmatrix} \tag{2.3}$$

A filter operator ($\langle\rangle$) is used to decompose instantaneous velocity and pressure fields into the resolved and unresolved parts [35]:

$$V_i = U_i + u_i, \quad U_i = \langle V_i \rangle, \quad \langle u_i \rangle \neq 0 \tag{2.4}$$

$$p = P + p_u, \quad P = \langle p \rangle, \quad \langle p_u \rangle \neq 0 \tag{2.5}$$

In general, the filtering operator ($<>$) is non-commutative, i.e., it may not commute with the spatial and temporal derivatives. Applying this spatio-temporal filter to the Navier-Stokes and

pressure equations (Eqs. 2.1-2.2), the resolved field takes the form [39]:

$$\frac{\partial U_i}{\partial t} + U_j \frac{\partial U_i}{\partial x_j} = -\frac{\partial \tau(V_i,V_j)}{\partial x_j} - \frac{\partial P}{\partial x_i} + \nu \frac{\partial^2 U_i}{\partial x_j \partial x_j} - F_i, \tag{2.6}$$

$$\frac{\partial^2 P}{\partial x_i \partial x_i} = -\frac{\partial U_i}{\partial x_j}\frac{\partial U_j}{\partial x_i} - \frac{\partial^2 \tau(V_i,V_j)}{\partial x_i \partial x_j} - \frac{\partial F_i}{\partial x_i} \tag{2.7}$$

where $\tau(V_i,V_j)$ is the generalized sub-filter stress (SFS) introduced in Ref. [35] and F_i is the commutation residue term. Eq. 2.7 is the filtered pressure field evolution equation obtained by taking divergence of Eq. 2.6 and applying the continuity equation for filtered velocity, $\partial U_i/\partial x_i = 0$.

The commutation residue term, F_i in Eqs. 2.6 and 2.7 is given by [39]:

$$\begin{aligned} F_i = &\left\langle \frac{\partial V_i}{\partial t} \right\rangle + \left\langle V_j \frac{\partial V_i}{\partial x_j} \right\rangle + \left\langle \frac{\partial p}{\partial x_i} \right\rangle - \left\langle \nu \frac{\partial^2 V_i}{\partial x_j \partial x_j} \right\rangle \\ &- \frac{\partial U_i}{\partial t} - U_j \frac{\partial U_i}{\partial x_j} - \frac{\partial P}{\partial x_i} + \nu \frac{\partial^2 U_i}{\partial x_j \partial x_j} - \frac{\partial \tau(V_i,V_j)}{\partial x_j} \end{aligned} \tag{2.8}$$

When the filter is commutative, $F_i = 0$ and non-zero otherwise. In general, slow changes in physical resolution do not incur much commutation residue ($F_i \approx 0$) and uniform-resolution closure models can be used. However, if the resolution variation in the switch-over region is steep, the commutation residue can be dominant and its effect must be suitably modeled [39].

The generalized second moment of velocity field or sub-filter stress (SFS) is given by [35]:

$$\tau(V_i,V_j) = \langle V_i V_j \rangle - \langle V_i \rangle \langle V_j \rangle \tag{2.9}$$

In principle, SFS can be modeled at different levels of sophistication similar to the closure of Reynolds stress term. In its simplest form, SFS can be modeled via Boussinesq approximation [31, 62]:

$$\tau(V_i,V_j) = -2\nu_u S_{ij} + \frac{2}{3} k_u \delta_{ij}; \quad \text{where} \quad \nu_u = C_\mu \frac{k_u^2}{\varepsilon_u} = \frac{k_u}{\omega_u} \tag{2.10}$$

where ν_u, k_u, ε_u and ω_u are the unresolved eddy viscosity, unresolved kinetic energy, unresolved

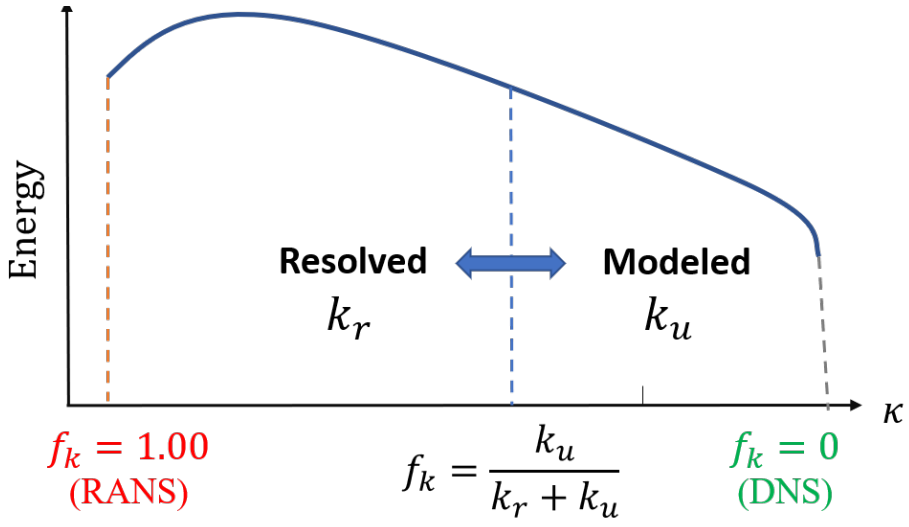

Figure 2.1: Turbulent kinetic energy spectrum

dissipation rate and unresolved specific dissipation rate, respectively. S_{ij} is the resolved strain-rate tensor defined as:

$$S_{ij} = \frac{1}{2}\left(\frac{\partial U_i}{\partial x_j} + \frac{\partial U_j}{\partial x_i}\right) \tag{2.11}$$

In PANS, the range of the resolved and unresolved scales is controlled by the parameters:

$$f_k \equiv \frac{k_u}{k}, \quad f_\varepsilon \equiv \frac{\varepsilon_u}{\varepsilon}, \quad f_\omega = \frac{f_\varepsilon}{f_k} = \frac{\omega_u}{\omega} \tag{2.12}$$

where k is the total turbulent kinetic energy and ε is the total dissipation rate. These ratios dictate the extent of implicit filtering in PANS. Fig. 2.1 illustrates a representative turbulence kinetic energy spectrum. The filter parameter or physical resolution, f_k can vary between $0 \leq f_k \leq 1.0$. In RANS, the entire kinetic energy spectrum is modeled, therefore RANS computations are performed by setting $f_k = 1.0$. On the other hand, the entire kinetic energy spectrum is resolved in DNS simulations; therefore, the turbulence model is not activated which is achieved by setting $f_k = 0$. Please note that f_ε is taken as unity in all the simulations in this research work as dissipation is assumed to occur in the unresolved scales.

Based on the relationships defined in Eqs. 2.10 and 2.12, the unresolved eddy viscosity can be written as:

$$\nu_u = \frac{f_k}{f_\omega}\frac{k}{\omega} = \frac{f_k^2}{f_\varepsilon}\frac{k}{\omega} = f_k^2\frac{k}{\omega} = f_k^2\nu_T \tag{2.13}$$

where ν_T is the total viscosity computed by RANS models. Moreover, the effective Reynolds number (Re_{eff}) of the simulated flow is [38]:

$$Re_{eff} = \frac{V_\infty D}{\nu + \nu_u} = \frac{V_\infty D}{\nu + f_k^2\nu_T} \tag{2.14}$$

Clearly, for high physical resolution (low f_k) simulations, the contribution of the modeled viscosity (ν_u) is small and Re_{eff} approaches the actual Reynolds number of the flow.

The size of the smallest resolved scales for a particular f_k is the computational Kolmogorov length scale given by [38, 42]:

$$\eta_u = \left(\frac{(\nu+\nu_u)^3}{\varepsilon}\right)^{1/4} \tag{2.15}$$

As f_k is reduced, it is clear from Eqs. 2.14 and 2.15 that the size of smallest resolved scales (η_u) in the flow decreases and a wider range of scales are resolved. This increases the computational effort and allows for resolution of dynamically relevant scales increasing the accuracy of coherent structures computed. The smallest physical resolution that is achieved for a given grid is calculated as [33],

$$f_k \geq \frac{1}{\sqrt{C_\mu}}\left(\frac{\Delta}{\Lambda}\right)^{2/3} \tag{2.16}$$

wherein Δ is the smallest grid dimension and $\Lambda = \frac{k^{3/2}}{\varepsilon}$ is the integral length scale of turbulence. Thus, specification of f_k in the simulation is contingent on a balance of available computational resources and the required accuracy of computed physics.

PANS computations can be performed in two ways. In the first approach, f_k is uniform everywhere. This approach is termed as wall-resolved PANS (WR-PANS) and does not involve commutation error or a 'hand-shake' region as the uniform filter commutes with spatio-temporal derivatives. In this approach, $F_i = 0$ in the velocity and pressure evolution equations. Consequently,

uniform f_k closures for unresolved scales developed in Refs. [33, 62] can be employed. Thus far, PANS with spatially uniform f_k has been used to compute various canonical flows to establish the theoretical foundation [40, 42, 45, 48]. Chapters 3 and 4 in this dissertation use the WR-PANS approach for the simulations in these studies. In the second approach, f_k varies in space and/or in time and is termed as wall-modeled PANS (WM-PANS). In regions of resolution variation, $F_i \neq 0$ and additional closure modeling terms arise due to commutation error as shown in Ref. [39]. This region of resolution change is similar to the 'hand-shake' or interface region in hybrid RANS-LES computations. This WM-PANS approach is utilized for closure modelling in Chapters 5 and 6.

3. PARTIALLY-AVERAGED NAVIER-STOKES FORMULATION OF A TWO-LAYER TURBULENCE MODEL[1]

3.1 Introduction

Recent years have witnessed the emergence of Scale-Resolving Simulations (SRS) as key turbulence computational tools due to their 'accuracy-on-demand' nature. Large scale coherent structures are resolved directly while the remaining small scales are modeled as stochastic turbulence. The accuracy of the solution is dependent on the extent of the scales resolved and the fidelity of closure models of the unresolved scales. Partially-Averaged Navier-Stokes (PANS) is a bridging SRS approach initially developed by Refs. [31, 32, 34] who employ a two-equation subgrid closure model for unresolved scales. In PANS, the physical resolution is controlled by the ratios of unresolved to total kinetic energy (f_k) and unresolved to total dissipation (f_ε). The accuracy of PANS turbulence model and computational costs increase with decreasing filter parameter, f_k, as more scales in the energy spectrum are resolved. Studies by Refs. [48, 56, 63] exhibit the effectiveness of PANS in capturing physics for a wide range of industry relevant flows with various PANS subgrid closures. These studies demonstrate the potential benefits of PANS in achieving optimal cost-accuracy balance. The theoretical foundation of PANS is further developed in Refs. [38, 39, 46].

One of the key SRS challenges is accurate, yet computationally reasonable, near-wall closure modeling. Attempts have been made to enhance the near-wall physical fidelity of the scale resolving simulations by Ref. [50] who implement a four-equation $k-\varepsilon-\zeta-f$ model. In this work, the near-wall eddy viscosity is defined in terms of wall-normal fluctuations rather than the total kinetic energy. They also include a hybrid wall treatment to incorporate the low Reynolds number effects. A low Reynolds number variant of the PANS $k-\varepsilon$ model has also been proposed by Ref. [51] to account for the viscous and wall-damping effects where model equations are integrated all the way to the wall.

[1]Reprinted with permission from "Partially Averaged Navier–Stokes Formulation of a Two-Layer Turbulence Model" by Chetna Kamble, Sharath S. Girimaji, and Hamn-Ching Chen, 2020, AIAA Journal, vol. 58, 174–183, Copyright (2019) by American Institute of Aeronautics and Astronautics, Inc [60].

In this study, to provide PANS near-wall closure guidance, we look to other RANS approaches. The $k-\varepsilon$ turbulence model is one of the most extensively used model in industry and is available in nearly all commercial CFD codes. Most importantly, this model is robust over a variety of freestream conditions, a feature that is a key advantage over other popular models, e.g., $k-\omega$ turbulence model [64]. However, the standard $k-\varepsilon$ model is known to be deficient in the near-wall region. It is either coupled with the wall functions or formulated as a low-Reynolds number model for accurate representation of the near-wall behavior. The inherent assumptions of wall functions prohibit them from being universally applicable, especially in separated flows [65]. On the other hand, the low-Reynolds number formulations are computationally expensive. To circumvent these limitations, a two-layer modeling strategy was proposed by Ref. [59] by coupling the standard k-ε model with a near-wall one-equation model of Ref. [66]. In this approach, the two-equation k- ε model is applied to the high Reynolds number region away from the wall. The viscosity dominated near-wall region is modeled with a one-equation model which reduces the physical uncertainties and numerical difficulties of resolving large turbulence gradients. This two-layer model of Ref. [59] has been tested successfully for flow past axisymmetric bodies with complex features including separation, recirculation and reattachment.

The present study has two main objectives: (i) Adaptation of the two-layer turbulence model into the PANS paradigm and (ii) Investigation and validation of the effectiveness of the PANS two-layer model in the benchmark turbulent channel flow. This study aims to incorporate the two-layer model as a strategy to enhance the near-wall modeling of PANS bridging methods by (a) avoiding uncertainties in near-wall boundary conditions of turbulent length scales and, (b) capturing relevant physics of the viscosity dominated near-wall region.

The remainder of the study is arranged as follows: In Section. 3.2, the PANS formulation of the two-layer turbulence model using the approach adopted by Refs. [31, 62] is presented. The details of the numerical setup and convergence study are presented in Section. 3.3. In Section. 3.4, PANS results are compared against DNS studies. The new model is tested in a wall-bounded channel flow of $Re_\tau = 180-950$.

3.2 Theoretical formulation

3.2.1 Formulation of PANS outer layer

The PANS model equations are identical in form to the corresponding RANS counterpart as required by averaging invariance [35]. The RANS two-layer $k-\varepsilon$ model [59] is a standard $k-\varepsilon$ turbulence model in the outer region. Correspondingly, in the outer layer, we propose that the standard two-equation PANS $k-\varepsilon$ model [31] is applicable:

$$\frac{\partial k_u}{\partial t}+U_j\frac{\partial k_u}{\partial x_j}=P_u-\varepsilon_u+\frac{\partial}{\partial x_j}\left[\left(\nu+\frac{\nu_u}{\sigma_{ku}}\right)\frac{\partial k_u}{\partial x_j}\right] \tag{3.1}$$

$$\frac{\partial \varepsilon_u}{\partial t}+U_j\frac{\partial \varepsilon_u}{\partial x_j}=C_{e1}\frac{P_u\varepsilon_u}{k_u}-C_{e2}^*\frac{\varepsilon_u^2}{k_u}+\frac{\partial}{\partial x_j}\left[\left(\nu+\frac{\nu_u}{\sigma_{\varepsilon u}}\right)\frac{\partial \varepsilon_u}{\partial x_j}\right] \tag{3.2}$$

where $P_u=\tau(V_i,V_j)\frac{\partial U_i}{\partial x_j}$ is the production in the unresolved scales. The modified closure coefficient C_{e2}^* is given as,

$$C_{e2}^*=C_{e1}+\frac{f_k}{f_\varepsilon}(C_{e2}-C_{e1}) \tag{3.3}$$

The PANS transport Prandtl coefficients are derived based on consistency with log-law physics [41],

$$\sigma_{ku}=\frac{f_k^2}{f_\varepsilon}\sigma_k \quad \text{and} \quad \sigma_{\varepsilon u}=\frac{f_k^2}{f_\varepsilon}\sigma_\varepsilon \tag{3.4}$$

The values of the other RANS coefficients used in this study are: $C_\mu=0.09$; $C_{e1}=1.44$; $C_{e2}=1.92$; $\sigma_k=1.0$; $\sigma_\varepsilon=1.3$. In the outer region of the boundary layer, the Reynolds number is reasonably high. Thus, f_ε is taken to be unity.

Before proceeding to develop the PANS inner layer equations, we will summarize the RANS inner layer formulation.

3.2.2 Description of RANS inner layer

In the RANS context, closure modeling of near-wall turbulence is achieved via a one-equation model of Ref. [66] derived based on the Kolmogorov-Prandtl turbulence energy hypothesis. This one-equation treatment of the viscosity-dominated regions provides an easier means of imposing

near-wall scaling on the model. Further, it offers a simple means of coupling the inner layer closure with the standard $k-\varepsilon$ model in the outer layer.

In the RANS two-layer model, no modification is made to the turbulent kinetic energy evolution equation in the inner layer:

$$\frac{\partial k}{\partial t}+U_j\frac{\partial k}{\partial x_j}=P-\varepsilon+\frac{\partial}{\partial x_j}\left[\left(\nu+\frac{\nu_t}{\sigma_k}\right)\frac{\partial k}{\partial x_j}\right] \tag{3.5}$$

Dissipation is specified in terms of turbulent kinetic energy and length scale as,

$$\varepsilon=\frac{k^{3/2}}{l_\varepsilon} \tag{3.6}$$

Eddy viscosity is similarly given by,

$$\nu_t=C_\mu\sqrt{k}\,l_\mu \tag{3.7}$$

The length scales of dissipation and eddy viscosity are specified as [59],

$$\begin{aligned} l_\varepsilon &= C_l y\left[1-exp(-R_y/A_\varepsilon)\right] \\ l_\mu &= C_l y\left[1-exp(-R_y/A_\mu)\right] \\ R_y &= \frac{\sqrt{k}y}{\nu} \end{aligned} \tag{3.8}$$

Here, R_y is the turbulence Reynolds number dependent on wall-normal distance, y, and turbulent kinetic energy. The length scales follow a structure similar to the Van Driest-style damping function [67], however, employ R_y instead of y^+ in the exponential term, which extends the applicability of the two-layer model to complex separated flows. The constant C_l is defined as $C_l=\kappa C_\mu^{-3/4}$ where κ is the von Karman constant. A_μ is calibrated to be 70 to recover the log-law constant B = 5.45. Further, $A_\varepsilon=2C_l$ is used to capture the asymptotic behavior of ε in the viscous sublayer.

3.2.3 Formulation of PANS inner layer

Conveying the benefits of the RANS inner layer to SRS closure requires recalibration of the empiricism incumbent in the inner layer equations. Emulating the RANS model development for the inner layer, Eq. 3.1 is utilized to solve for the unresolved kinetic energy, k_u, in the PANS inner layer. Unresolved dissipation, ε_u, is calculated explicitly in terms of the unresolved kinetic energy and a length scale as,

$$\varepsilon_u = \frac{k_u^{3/2}}{l_{\varepsilon u}} \tag{3.9}$$

The eddy viscosity for the unresolved scales is

$$\nu_u = C_{\mu u}\sqrt{k_u}\, l_{\mu u} \tag{3.10}$$

where $C_{\mu u} = C_\mu$ from the fixed point analysis argument of Ref. [34].

Now, the length scales from the corresponding RANS two-layer model must be transformed in the PANS regime. We propose that the length scales follow a structure similar to their RANS counterpart as:

$$\begin{aligned} l_{\varepsilon u} &= F_1(f_k)\, C_l y\,[1 - exp(-R_{yu}/A_\varepsilon)] \\ l_{\mu u} &= F_2(f_k)\, C_l y\,\left[1 - exp(-R_{yu}/A_\mu)\right] \end{aligned} \tag{3.11}$$

where F_1 and F_2 are reduction ratios associated with the unresolved dissipation and unresolved eddy viscosity respectively, and R_{yu} is the turbulence Reynolds number in the PANS inner layer defined as

$$R_{yu} = \sqrt{k_u}y/\sqrt{f_k}\nu \approx R_y \tag{3.12}$$

This definition of R_{yu} preserves the exponential variation of the PANS inner layer length scales to be similar to their RANS counterpart from Eq. 3.8. The expressions of the reduction ratios are not known a-priori and need to be established based on the underlying principles incumbent in the RANS inner layer model and PANS subgrid closures. Further, these reduction ratios depend exclusively on f_k as only the unresolved kinetic energy (k_u) equation is solved in the inner layer

and other turbulent quantities (ε_u and ν_u) are directly specified in terms of k_u.

The inner layer includes viscous sublayer, buffer layer and part of the logarithmic layer. The length scales in the RANS context were derived based on emulating behavior of turbulent quantities at the two extremes of the inner layer, i.e., at the wall and in the log layer. In the following sections, we perform a similar analysis to obtain reduction ratios, F_1 and F_2, for the PANS inner layer formulation.

Length scale modeling in viscous sublayer: Asymptotic behavior of ε_u at the wall

The limiting behavior of turbulence quantities near the wall has been well established in works of Ref. [68]. For the filtered fields, unresolved turbulent kinetic energy $k_u \sim O(y^2)$ and unresolved dissipation $\varepsilon_u \sim O(y^0)$ approaching the wall boundary. Near the wall, the flow quantities are dependent on the wall-normal distance. Here, the Taylor series expansion of instantaneous velocity, V_i, can be written as,

$$V_i(y) = V_i(0) + \frac{\partial V_i}{\partial y} y + O(y^2) \tag{3.13}$$

The no-slip condition at the wall makes $V_i(0) = 0$. Therefore, $\partial V_i / \partial y \approx V_i(y) / y$ and we can get the following relations by simple mathematical manipulations,

$$\langle V_i V_i \rangle = \left\langle \frac{\partial V_i}{\partial y} \frac{\partial V_i}{\partial y} \right\rangle y^2 \quad \text{and} \quad \langle V_i \rangle = \left\langle \frac{\partial V_i}{\partial y} \right\rangle y \tag{3.14}$$

$$\langle V_i V_i \rangle - \langle V_i \rangle \langle V_i \rangle = \left[\left\langle \frac{\partial V_i}{\partial y} \frac{\partial V_i}{\partial y} \right\rangle - \left\langle \frac{\partial V_i}{\partial y} \right\rangle \left\langle \frac{\partial V_i}{\partial y} \right\rangle \right] y^2 \tag{3.15}$$

This formulation directly leads to,

$$\varepsilon_u = \frac{2\nu k_u}{y^2} \tag{3.16}$$

which is the asymptotic limit of unresolved dissipation.

The rationale of the ε_u length scale is studied using this asymptotic behavior. At the wall,

Taylor series expansion of $l_{\varepsilon u}$ leads to,

$$l_{\varepsilon u} = F_1(f_k)\, C_l y \left[1 - 1 + \frac{R_{yu}}{A_\varepsilon} - \ldots\right] \approx F_1(f_k)\, C_l y \left(\frac{R_{yu}}{A_\varepsilon}\right) \tag{3.17}$$

as both kinetic energy and wall-normal distance are negligible at the wall. Substituting the near-wall length scale approximation (Eq. 3.17) in Eq. 3.9 and comparing with Eq. 3.16, we derive the reduction ratio of the unresolved dissipation,

$$F_1(f_k) = \sqrt{f_k} \tag{3.18}$$

At the wall, the behavior of the reduction ratio for the unresolved viscosity, $F_2(f_k)$, is not known and shall be established next based on the log-layer physics.

Length scale modeling in Log layer: Equilibrium boundary layer analysis

The equilibrium boundary layer (EBL) analysis establishes a framework for derivation of model constants in the RANS context. A similar analysis is done for the PANS closure for derivation of coefficients stated in Eqs. 3.3 and 3.4. In this section, we verify the formulation of the length scales via the PANS-EBL analysis.

On an average, neither RANS, and consequently, nor PANS velocity field statistics grow in the equilibrium state of the boundary layer. Therefore, in the outer layer, we have,

$$\frac{Dk_u}{Dt} \approx 0 \tag{3.19}$$

The above argument reduces the k-equation in the equilibrium boundary layer to

$$P_u \approx \varepsilon_u = \frac{u_\tau^3}{\kappa y} \quad \text{and} \quad k_u = f_k \frac{u_\tau^2}{\sqrt{C_\mu}} \tag{3.20}$$

We expect the unresolved dissipation ε_u from the inner layer to reduce to its PANS-EBL representation in the log-layer (Eq. 3.20). Using the EBL representation of k_u, the unresolved dissipa-

tion (Eq. 3.9) can be written as,

$$\varepsilon_u = f_k^{3/2} \frac{u_\tau^3}{C_\mu^{-3/4}} \frac{1}{F_1(f_k) C_l y} \tag{3.21}$$

which should be equal to the EBL representation of ε_u from Eq. 3.20. Simplifying, we obtain the reduction ratio for unresolved dissipation as,

$$F_1(f_k) = f_k^{3/2} \tag{3.22}$$

which differs from $F_1(f_k) = \sqrt{f_k}$ derived from asymptotic behavior of dissipation (ε_u) in the viscous sublayer. This deviation arises due to the assumption of f_k being a spatio-temporal constant. This inconsistency, however, is only concentrated in a very thin layer near the wall with $y^+ < 30$ and doesn't affect the model's performance as will be witnessed in Section 3.4. Therefore, for this representation of PANS two-layer model, we aim to model the scales based on the accurate representation in the log-layer only. However, further calibration of the reduction ratio F_1 is needed to accurately represent the physics of viscous sublayer and buffer layer and will be addressed in future works.

For a seamless transition between the two layers, unresolved eddy viscosity in the inner and outer layer must be equal at the matching location, i.e, in the log layer. The inner layer eddy viscosity (Eq. 3.10) reduces to $\nu_u = C_\mu \sqrt{k_u} F_2(f_k)\ C_l y$ owing to the linear nature of length scales in the log layer. This unresolved eddy viscosity distribution must match the outer layer given in Eq. 2.10. Therefore, using the boundary layer representations of kinetic energy and dissipation (Eq. 3.20), we get,

$$\begin{aligned} \nu_{u-outer} &= C_\mu \frac{k_u^2}{\varepsilon_u} = f_k^2 u_\tau \kappa y \\ \nu_{u-inner} &= C_\mu \sqrt{k_u}\ F_2(f_k)\ C_l y = \sqrt{f_k}\ F_2(f_k)\ u_\tau \kappa y \end{aligned} \tag{3.23}$$

Equating the unresolved eddy viscosity values in both the layers, the reduction ratio F_2 is estab-

lished as

$$F_2(f_k) = f_k^{3/2} \tag{3.24}$$

A detailed analysis of the wall-normal location of the inner and outer layer match is presented later in the study.

In the region of viscous sublayer and buffer layer, the effect of damping functions alter the behavior of the length scales and must be accounted for while analyzing model's performance near the wall.

3.3 Computational setup and numerical convergence study

We examine the PANS two-layer turbulence model for the benchmark test case of turbulent channel flow for friction Reynolds numbers of $Re_\tau = 180 - 950$. Here, Re_τ is based on friction velocity u_τ, half channel width δ and the kinematic viscosity ν. DNS studies by Ref. [69] and Ref. [70] are referenced to validate the PANS two-layer computations.

The computational domain is a rectangular prism defined in a Cartesian coordinate system with origin at the inlet. Periodic boundary conditions are applied in the streamwise (x) and spanwise (z) directions and the no-slip boundary condition is assigned at the walls in the normal (y) direction. A constant pressure gradient is specified in the streamwise direction to drive the flow. An open-source finite volume solver, OpenFOAM, is used for numerical computations with a PISO [71] algorithm suitable for transient flow simulations. Second order accurate schemes are used for both spatial and temporal discretizations with residual tolerance of 10^{-9}.

A structured mesh with hexahedral elements is generated and is refined at the walls of the channel to obtain sufficient grid resolution in the inner layer. A convergence study is performed for $Re_\tau = 590$ to investigate grid dependence of one-point statistics. The details of the study are presented in Table 3.1. The grid elements are varied in y-direction as the statistics are found to be more sensitive to grid refinement in this direction due to large wall-normal gradients. Further, accurate representation of viscous sublayer requires sufficient grid resolution below y^+ of 5. Therefore, first grid point has been maintained at $y^+ < 1$ for all grid configurations for precise

Table 3.1: Parameters for grid convergence for $Re_\tau = 590$; ($\Delta y_c^+ = y$ at the center of channel, L_x and L_z are the domain lengths in streamwise and spanwise directions, t^*_{avg} is the averaging interval)

Grid	Grid size (N_x, N_y, N_z)	(L_x, L_z)	Δt^*	Δx^+	Δy_c^+	Δz^+	t^*_{avg}
G_1	64 X 25 X 64	$2\pi\delta$ X $\pi\delta$	0.00147	57.92	90.27	28.96	59
G_2	64 X 50 X 64	$2\pi\delta$ X $\pi\delta$	0.00089	57.92	46.12	28.96	89
G_3	64 X 100 X 64	$2\pi\delta$ X $\pi\delta$	0.00059	57.92	23.31	28.96	148
G_4	64 X 150 X 64	$2\pi\delta$ X $\pi\delta$	0.00059	57.92	15.60	28.96	177

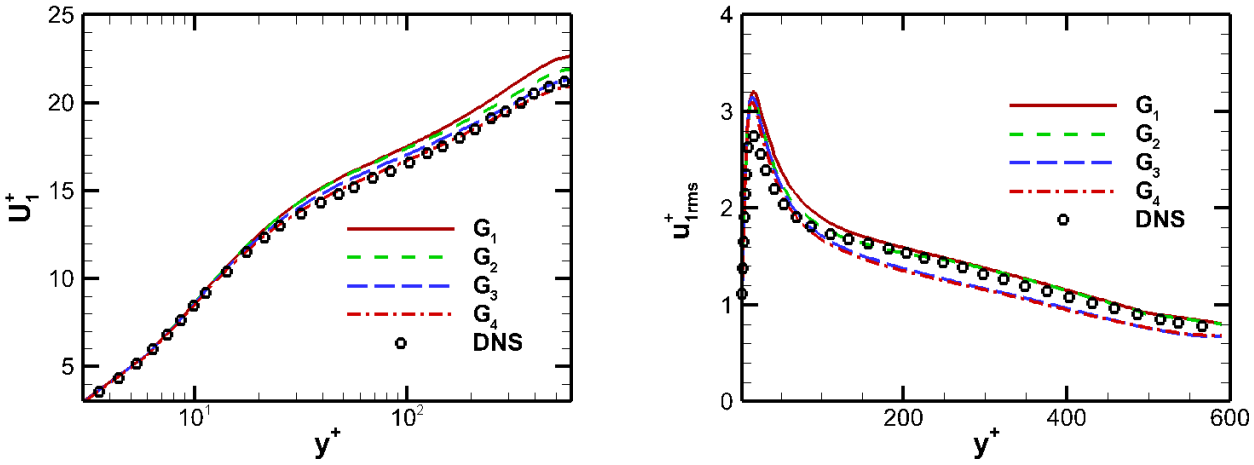

Figure 3.1: Results from the convergence study (Table 3.1); mean streamwise velocity (left) and total (resolved + modeled) streamwise turbulence intensity (right)

depiction of the near-wall behavior. The CPU time is proportional to the number of grid points as finer grids require smaller time steps and longer time duration for averaging. The time units are non-dimensionalised by the friction velocity (u_τ) and δ. The filter control parameter used for all numerical simulations in this section is $f_k = 0.1$, i.e., 90% of the turbulence spectrum is resolved and the remaining is modeled using the PANS two-layer turbulence model. Results for other f_k values will be discussed later in Section 3.4.

The grid sensitivity results are presented in Fig. 3.1 for spatio-temporally averaged mean streamwise velocity and streamwise turbulence intensity profiles. The coarsest grid, G_1, shows largest deviation from the DNS data. In PANS two-layer model, the damping functions reduce

Table 3.2: Parameters of numerical simulations

Case	Re_τ	f_k	Grid size (N_x, N_y, N_z)	(L_x, L_z)	Δt^*	Δx^+	Δy_c^+	Δz^+	t^*_{avg}
C_1	180	0.1	64 X 50 X 64	$4\pi\delta$ X $\frac{4}{3}\pi\delta$	0.00072	35.34	11.88	11.79	10
C_2	395	0.2	64 X 50 X 64	$2\pi\delta$ X $\pi\delta$	0.00118	38.78	26.07	19.38	40
C_3	395	0.15	64 X 50 X 64	$2\pi\delta$ X $\pi\delta$	0.00079	38.78	26.07	19.38	40
C_4	395	0.1	64 X 50 X 64	$2\pi\delta$ X $\pi\delta$	0.00079	38.78	26.07	19.38	60
C_5	590	0.2	64 X 100 X 64	$2\pi\delta$ X $\pi\delta$	0.00088	57.92	23.31	28.96	60
C_6	590	0.15	64 X 100 X 64	$2\pi\delta$ X $\pi\delta$	0.00059	57.92	23.31	28.96	85
C_7	590	0.1	64 X 100 X 64	$2\pi\delta$ X $\pi\delta$	0.00059	57.92	23.31	28.96	148
C_8	950	0.1	70 X 90 X 80	4δ X 2δ	0.00076	54.29	41.61	23.75	190

the effective viscosity near the wall to levels lower than other PANS closures. Therefore, the grid requirement in the inner region increases, resulting in the inadequacy of a very coarse grid to accurately resolve the velocity fluctuations in the inner layer. Nevertheless, the results converge quickly to the DNS profiles with increasing number of grid points in the inner region. Improving the ability of the PANS two-layer model to capture statistics using coarser grids in the inner layer is currently ongoing.

3.4 Results and discussion

The capability of other PANS approaches in capturing the physics of many flow regimes has already been examined extensively from works of Refs. [31, 42, 48, 50, 62]. In this section, we evaluate the capability of PANS two-layer model for predicting one-point turbulence statistics and flow structures in a channel flow. A complete list of the numerical tests performed is presented in Table 3.2.

3.4.1 f_k dependence study

Reducing the filter parameter f_k allows resolution of more scales (higher wavenumbers) incumbent in the fluid flow. However, to ensure that these high wavenumbers are fully resolved, a finer grid resolution is required. Consequently, the optimal f_k is bound by the computational cost. In this section, we present a study to establish the dependency of the flow statistics on the filter

parameter f_k.

In wall-bounded shear flows, the Tollmien–Schlichting (T-S) wave is the underlying instability mechanism which must adequately manifest to capture essential flow features. For $f_k > 0.3$, this important instability is not resolved as the corresponding computational Reynolds number is not sufficient for the T-S waves to become unstable [40]. From the contour plots of unresolved eddy viscosity in Fig. 3.2, it is evident that higher f_k values increase the unresolved eddy viscosity in the system, which dampens perturbations introduced by the instability. Therefore, according to Fig. 3.3, the convergence of statistics is obtained for reduced values of f_k.

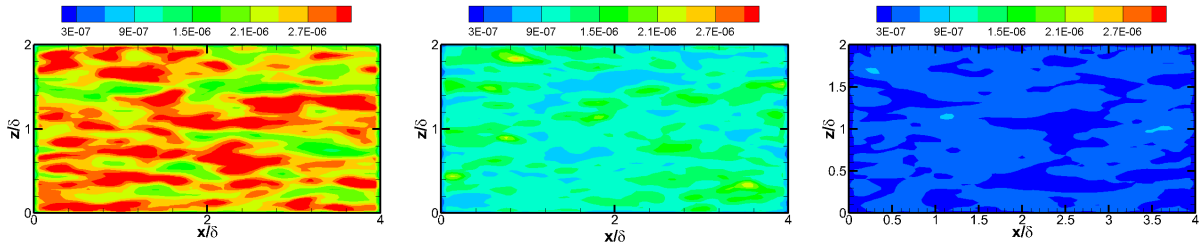

Figure 3.2: Unresolved eddy viscosity contours for C_5 (left), C_6 (middle) and C_7(right) at $y^+ = 40$

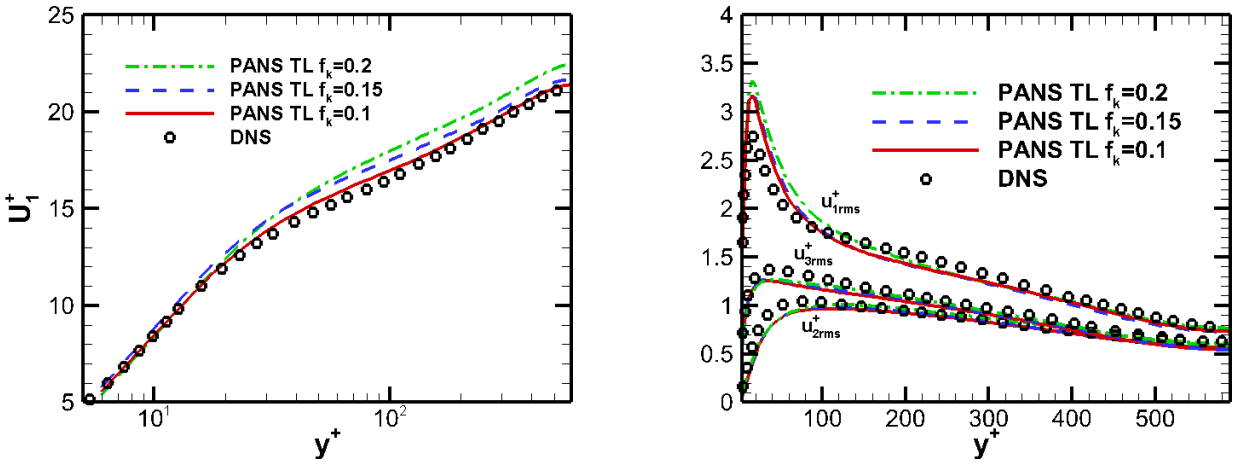

Figure 3.3: Mean streamwise velocity (left) and total (resolved + modeled) turbulence intensities (right) for different spectral cutoff, f_k, for $Re_\tau = 590$

Now, we extend the f_k sensitivity study to visualize turbulence structures in the flow field. Coherent structures such as hairpin vortices are known to drive the dynamics of turbulent channel flow. Near the outer edge of the viscous sublayer, relatively small scale eddies produce the maximum Reynolds stresses via the ejection and sweep mechanisms. In this study, the small scale eddies in the near-wall region are visualized quantitatively by the Q-criterion defined as $Q = \frac{1}{2}(\Omega^2 - S^2)$ where Ω is the antisymmetric and S is the symmetric component of the velocity gradient tensor. The unresolved eddy viscosity plays a crucial role in damping these small scale eddies. From Fig. 3.2, the unresolved eddy viscosity contour plots indicate that reducing f_k increases the effective computational Reynolds number releasing more unsteadiness in the flow field. Thus, from Fig. 3.4, the iso-surfaces and corresponding contour plots at $y^+ = 40$ reveal progressively finer coherent structures with reduction in f_k value.

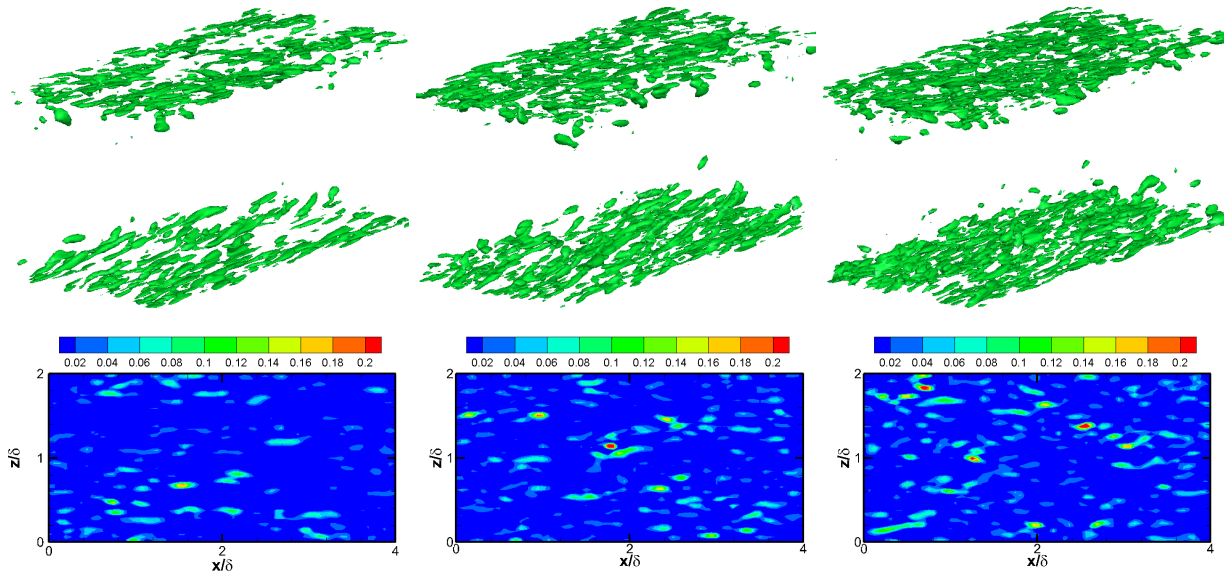

Figure 3.4: Iso-surfaces of second invariant of velocity gradient tensor (Q-factor) for varying spectral cut-off (top) and the corresponding Q-factor contours at $y^+ = 40$ (bottom) for C_5 (left), C_6 (middle) and C_7 (right)

One of the key means of assessing the fidelity of the PANS two-layer model is to ensure that the prescribed (a priori) modeled-to-total kinetic energy and dissipation ratios are recovered. This

is achieved via calculating the a posteriori viscosity reduction ratio (f_ν) using computed fields. It is the ratio of unresolved eddy viscosity (ν_u) to total eddy viscosity (ν_t) defined as,

$$f_\nu = \frac{1}{D_\mu}\frac{\nu_u}{\nu_t} \tag{3.25}$$

where $D_\mu = [1 - exp(-R_{yu}/A_\mu)]$ is the damping function of the unresolved eddy viscosity length scale. Here,

$$\nu_t = C_\mu \frac{k_t^2}{\varepsilon_t} = C_\mu \frac{(k_r + \bar{k_u})^2}{(\varepsilon_r + \bar{\varepsilon_u})} \tag{3.26}$$

$$\text{where} \quad k_r = \overline{U_i U_i} - \bar{U}_i \bar{U}_i \quad \text{and} \quad \varepsilon_r = \nu \left(\overline{\frac{\partial U_i}{\partial x_j}\frac{\partial U_i}{\partial x_j}} - \frac{\partial \bar{U}_i}{\partial x_j}\frac{\partial \bar{U}_i}{\partial x_j} \right) \tag{3.27}$$

where k_r and ε_r are the kinetic energy and dissipation contained in the resolved field. Fig. 3.5 presents the f_ν recovery (a posteriori) value from the simulations for different prescribed f_k filter ratios for $Re_\tau = 395$ and 590. In the outer layer, it is evident that the recovered (a posteriori) value is close to the specified (a priori) value. However, very near the wall f_ν is not very close to the specified value. Nevertheless, through most of the boundary layer, the model functions as dictated by closure physics.

3.4.2 Re_τ dependence study

In this section, the ability of the PANS two-layer model to capture one-point statistics over a range of Reynolds number is investigated. The results obtained from the PANS two-layer computations are averaged temporally and spatially in homogeneous directions to reveal the mean and resolved turbulent fields. The resolved turbulent quantities are then added to the modeled fields to obtain the total turbulence behavior. The normalized streamwise mean velocity has been presented in Fig. 3.6 for different friction Reynolds numbers. The PANS two-layer low Reynolds number run of $Re_\tau = 180$ accurately captures the higher intercept of the logarithmic profile as seen in the results of Ref. [69]. The intercepts remain unaltered for higher Reynolds number computations.

Coefficient of skin friction based on the centerline velocity, $C_f = \tau_w/(\rho U_c^2/2)$, is presented in Fig. 3.6 for different Re_τ and grid sizes (for $Re_\tau = 590$ outlined in Table 3.1). The values from the

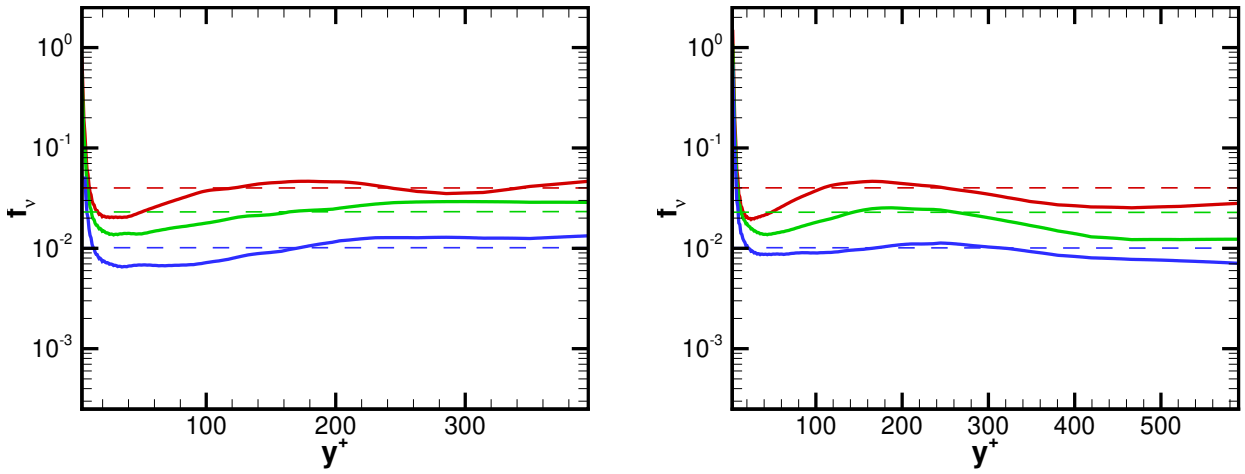

Figure 3.5: f_v recovery plots for $f_k = 0.2$ (red), $f_k = 0.15$ (green) and $f_k = 0.1$ (blue) for $Re_\tau = 395$ (left; $C_2 - C_4$) and $Re_\tau = 590$ (right; $C_5 - C_7$) ; the dashed lines represent the prescribed value of f_v

PANS two-layer computations are in excellent agreement with the DNS data. For $Re_\tau = 590$, the C_f values converge to the DNS values with increasing grid resolution.

Figure 3.7 shows the comparison of streamwise, spanwise, normal rms velocity fluctuations and turbulent shear stresses with the DNS data for $Re_\tau = 180$ and 395. The turbulence stresses for Re_τ of 590 have been presented in detail in Fig. 3.1 and Fig. 3.3. PANS two-layer formulation clearly offers an excellent advantage over the RANS model by accurately predicting the anisotropic behavior of the turbulent stresses.

Profiles of mean streamwise velocity and turbulence intensities have also been presented in Fig. 3.8 for a higher Reynolds number simulation ($Re_\tau = 950$). The profiles are compared to DNS results of Ref. [70]. The results are in a good agreement with the DNS data. For higher Reynolds numbers, $Re_\tau > 1000$, a wall-modeled PANS approach [40] is suggested for computational efficiency.

The invariants of tensor b_{ij} $\left(\equiv \frac{<u_i u_j>}{2k} - \frac{1}{3}\delta_{ij}\right)$ are excellent indicators of the degree of anisotropy in the system. Near-wall turbulence is dominated by $\langle u_1 \rangle$ and $\langle u_3 \rangle$ fluctuations, whereas the wall-normal fluctuation $\langle u_2 \rangle$ is negligible. This behavior manifests as the 2-component (2C) turbulence for small y^+. As the distance from the wall increases, wall-normal fluctuations become dominant

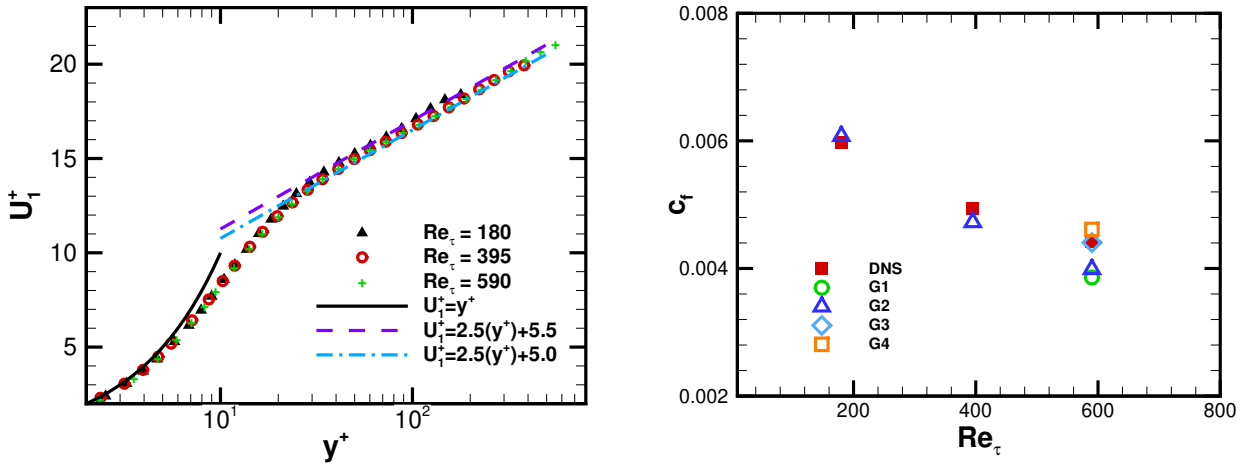

Figure 3.6: Mean streamwise velocity profiles for $Re_\tau = 180$ (C_1), 395 (C_4) and 590 (C_7) (left) and the skin-friction coefficient with respect to the centerline velocity (U_c) (right)

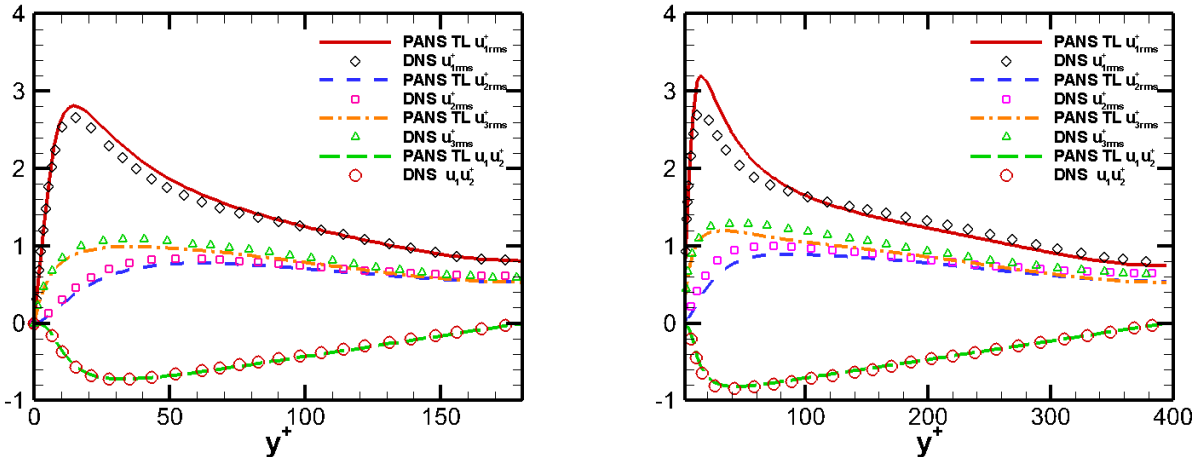

Figure 3.7: Profiles of total (resolved + modeled) turbulence intensities and Reynolds shear stresses for $Re_\tau = 180$ (C_1; left) and $Re_\tau = 395$ (C_4; right)

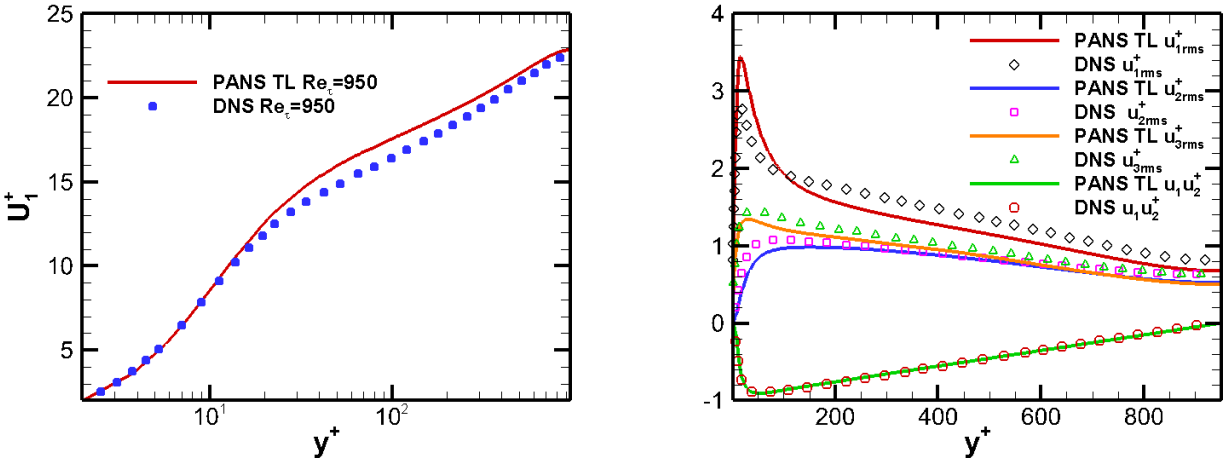

Figure 3.8: Mean streamwise velocity (left) and total (resolved + modeled) turbulence intensities and Reynolds shear stress (right) for $Re_\tau = 950$ (C_8)

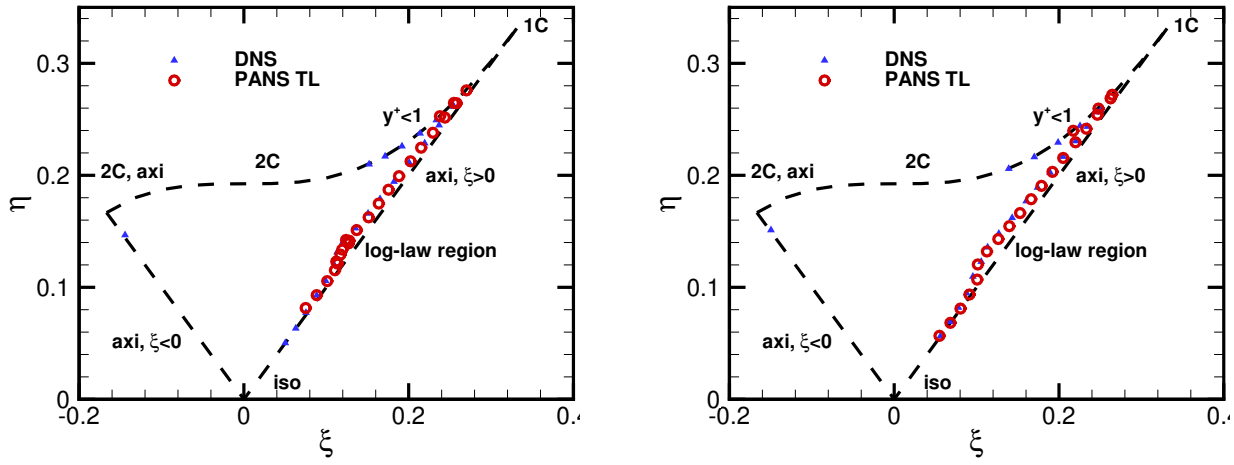

Figure 3.9: Anisotropy invariant map: Lumley triangle for channel flow for $Re_\tau = 395$ (C_4; left) and $Re_\tau = 590$ (C_7; right)

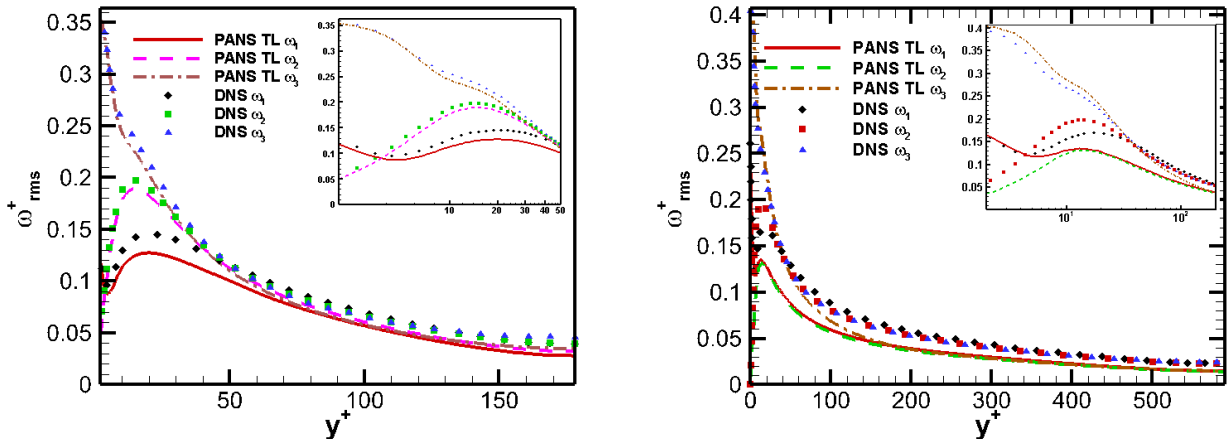

Figure 3.10: Streamwise, normal and spanwise components of normalized rms resolved vorticity fluctuations ω for $Re_\tau = 180$ (C_1; left) and $Re_\tau = 590$ (C_7; right)

and the turbulence tends towards isotropy, i.e, ξ and $\eta = 0$, near the core of the channel. Figure 3.9 presents an invariant map of the PANS Reynolds stress anisotropy tensor as a function of y^+. It is evident that PANS two-layer model captures the invariant behavior extremely well.

Now we examine the character of the fluctuating field generated by PANS computations. Specifically, we examine the vorticity field. The standard deviation of the components of the vorticity vector, $\omega = \nabla \times U$ is presented in Fig. 3.10. For lower Reynolds numbers ($Re_\tau = 180$), the simulations adequately capture the key attributes of the DNS data throughout the domain. For higher Reynolds numbers of $Re_\tau = 395$ (not shown) and 590, the vorticity fluctuations are very well captured by the PANS two-layer model away from the wall. However, the PANS simulations don't reproduce the high values of vorticity fluctuations observed by the DNS simulations in the near-wall region. According to Ref. [72], vorticity fluctuations have significantly larger contributions from smaller scales compared to the velocity fluctuations. The small scales are not fully resolved in the near-wall region due to the numerical and physical constraints leading to the discrepancies observed in Fig. 3.10.

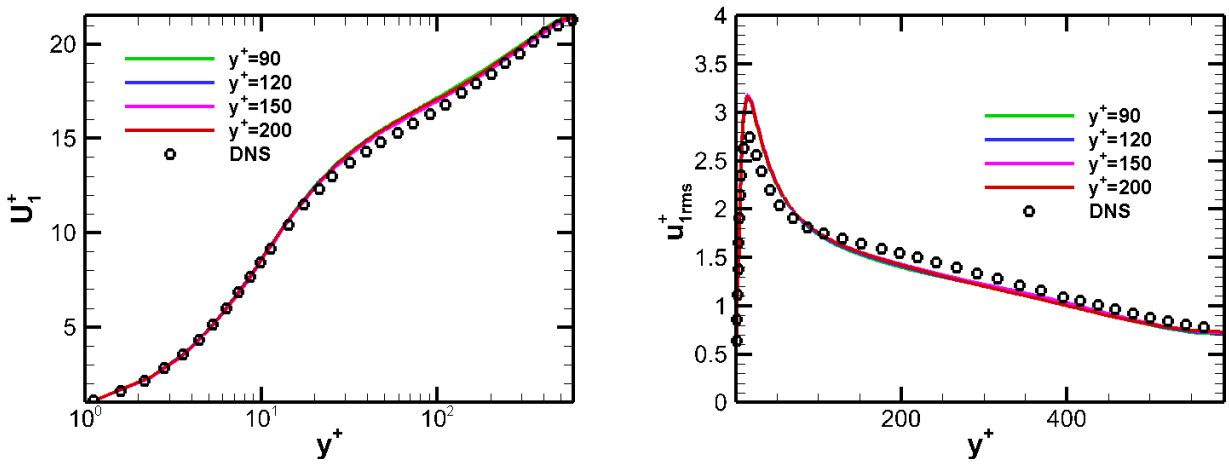

Figure 3.11: Mean streamwise velocity (left) and total streamwise (resolved + modeled) turbulence intensity (right) for different matching locations between the layers for $Re_\tau = 590$

3.4.3 Variation of the matching location between layers

In two-layer models, the matching between the inner and outer layer typically occurs at the edge of the viscous sublayer, i.e., in a region where viscous effects have become negligible to ensure a smooth variation of eddy viscosity. Ref. [59] matched the two layers at preselected grid lines running along the wall where minimum R_y is of the order of 250. The present PANS formulation utilizes the matching criterion proposed by Ref. [65]. This criterion matches the two layers when $\left[1 - exp(-R_{yu}/A_\mu)\right]$ is close to unity so that the viscous effects are small. This leads to effective switching between the layers at $y^+ \approx 90 - 100$. A study of varying the matching location between the inner and outer layers is performed and the results (Fig. 3.11) are found to be nearly independent of the switching location between the layers so long as matching occurs early in the log layer.

4. CHARACTERIZATION OF COHERENT STRUCTURES IN TURBULENT WAKE OF A SPHERE USING PARTIALLY-AVERAGED NAVIER-STOKES (PANS) SIMULATIONS[1]

4.1 Introduction

Turbulent flows such as wakes, jets, mixing layers, internal flows etc., display spatio-temporal coherence manifesting as large-scale structures that drive the flow physics. These coherent structures dictate both the global and local response of the system and hence play a vital role in engineering design considerations. In some engineering applications, it is important to capture the large-scale structures themselves as they directly determine large-scale entrainment leading to mixing. Aircraft wake vortex is another example in which the description of the coherent structures is important. For many other applications, the significance of coherent structures stem from the fact that they strongly influence local flow statistics of importance. Low-order single-point statistical closures such as Reynolds-averaged Navier-Stokes (RANS) models cannot effectively account for the multi-point coherence and yield poor estimates of important integrated parameters (C_d, C_l) and one-point statistics such as mean flow profiles and shear stress distributions. In summation, predictive computations must ensure that the dynamically relevant coherent structures are reasonably resolved for their inherent importance and crucial role in driving global and local flow response.

In turbulent flows with coherent structures, the velocity field (Φ) can be effectively decomposed into three parts as follows:

$$\Phi = \overline{\Phi} + \tilde{\phi} + \phi' \tag{4.1}$$

where the mean field is denoted by $\overline{\Phi}$, coherent structures by $\tilde{\phi}$ and stochastic background turbulence is given by ϕ'. Direct numerical simulation (DNS) resolves all components of the flow field precisely, but the cost can be prohibitive for almost all practical flows [23]. Large eddy simulation (LES) models the dissipative scales of the stochastic field while resolving the remainder of the

[1]Reprinted with permission from "Characterization of coherent structures in turbulent wake of a sphere using partially averaged Navier–Stokes (PANS) simulations" by Chetna Kamble and Sharath S. Girimaji, 2020, Physics of Fluids, vol. 32, Copyright (2020) by AIP Publishing [61].

flow field. While LES computational requirements are lower than those of DNS, the cost can still be too high for most engineering applications.

Scale-resolving simulations (SRS) offer a viable alternative to capture coherent-structure flow physics with reduced computational effort. The subject of this study is the bridging-SRS method [31] in which the cut-off length scale is controlled implicitly by specifying the extent of resolved kinetic energy. Unlike LES, bridging-SRS seeks to model not only the stochastic component of the flow field but also some of the smaller coherent-structure scales. Thus bridging-SRS techniques allow the cut-off filter to be placed in the smaller inertial scales and model the remainder of the turbulent flow field. The reduced computational burden requires that the subgrid closure model be of higher degree of sophistication than what is typically used in LES. The Partially-averaged Navier-Stokes (PANS) method is a bridging-SRS approach in which the subgrid model is developed systematically from RANS closures by accounting for scale-dependent physics [31, 34, 38, 39]. Thus PANS aims for a different balance between cut-off scale and accuracy than LES.

The goal of the study is to examine the ability of PANS-SRS method to capture correct behavior of one-point correlations and coherent structures in complex wakes. Important attributes of PANS in particular and SRS in general are examined for the case of flow past a sphere in the subcritical Reynolds number regime, $Re = 3700$. The specific objectives of the study are to: (i) validate the PANS-SRS using one-point statistics and global parameters; (ii) examine the dependence of large-scale coherent structures on the degree of resolution (or cut-off length scale) and (iii) characterize the coherent structures in the wake of a sphere and compare their features with those of other axisymmetric wakes.

Coherent structures in the wake of a sphere exhibit strong correlations in the azimuthal and radial directions at different downstream locations in the wake. These correlations can be quantitatively examined using a proper orthogonal decomposition (POD) approach [73]. Although, large-scale coherence in the wake of many axisymmetric bodies has been studied in detail [1, 74, 75, 76], the studies in the near-wake region of sphere are scarce. Therefore, we seek to characterize the near-wake coherent structures in the wake of a sphere using modal decomposition and examine

mode shapes/amplitudes.

The remainder of the study is organized as follows: In the next section we present a general discussion of coherent structures in the wake of the sphere and delineate a methodology for quantification of these structures. The turbulence model used is presented in Sec. 4.3. A brief description of simulation setup and grid configuration is outlined in Section. 4.4. Section. 4.5 presents the statistics and structures computed by the PANS-SRS simulations as a function of physical resolution (cut-off scales).

4.2 Coherent structures in the wake of a sphere

Unlike the statistically 2D wakes, the inherent three dimensionality of a sphere's wake renders it an interesting and challenging flow for turbulence model simulations. This flow is characterized by a smooth surface separation wherein the pressure gradient rather than the body geometry determines the separation location. The features of the sphere's wake are highly sensitive to the Reynolds number regime considered. Low Reynolds number laminar flow over a sphere is divided in four distinct regimes [77, 78]: (i) steady axisymmetric ($Re \leq 200$), (ii) steady planar-symmetric ($Re \in [210, 270]$), (iii) unsteady planar-symmetric ($Re \in [280, 375)$) and (iv) unsteady asymmetric ($Re \in [375, 800)$). Whereas high Reynolds number turbulent flow over a sphere is broadly classified in two regimes[5]: (i) subcritical ($Re \in [800, 3.7 \times 10^5)$) and (ii) supercritical ($Re > 3.7 \times 10^5$) where $Re \approx 3.7 \times 10^5$ is the critical Reynolds number where the drag crisis occurs. In this study we consider the coherent structures in the wake of a sphere in the subcritical Reynolds number regime.

Several numerical [5, 78, 79] and experimental [6, 80] studies have been conducted for flow over a sphere in the subcritical regime. With increase in computational power in recent years, DNS studies of a sphere's wake are also available [2, 81, 82]. These studies highlight several key features of flow past a sphere in this regime; (i) smooth separation of a laminar boundary layer, (ii) an axisymmetric free shear layer, (iii) roll-up of detached shear layers due to the Kelvin-Helmholtz (KH) instability, (iv) transition to high intensity turbulence and (v) vortex shedding in a three dimensional turbulent wake.

Behavior of vortical structures in the turbulent wake of a sphere has also been an active area of research [83]. Experiments by Ref. [84] analyzed migration of the vortex-separation point around the sphere for flow in the range $Re \in (400, 5 \times 10^6)$. Flow visualization by Ref. [85] established a wave-like motion exhibited by the wake in the streamwise axis plane. This large-scale waviness has also been confirmed by LES simulations of Ref. [78] and DNS of Ref. [2]. These studies have also established the tendency of the vortical structures to convect downstream in the same plane they are shed. Moreover, analysis of multiple shedding cycles revealed a randomness in the azimuthal shedding location of the vortices from the axisymmetric shear layer leading to a helical appearance of the wake.

For a quantitative analysis of coherent structures, proper orthogonal decomposition (POD) has been widely applied to various axisymmetric flows including jets [75], mixing layers [76] and wakes of axisymmetric bodies [86]. POD is a modal decomposition technique which extracts most energetic structures from a turbulent flow field. In this study, POD analysis is performed on the streamwise velocity fluctuations, u_x. The turbulent flow field (u_x) is decomposed into a set of basis functions, $\psi_i(\mathbf{x},t)$ which are defined by maximization of their normalized mean-square projection on the flow field (quantified by eigenvalue λ) resulting in the following integral equation [87]:

$$\int R_{i,j}(\mathbf{x},\mathbf{x}',t,t')\,\psi_j(\mathbf{x}',t')\,d\mathbf{x}'dt' = \lambda\,\psi_i(\mathbf{x},t) \tag{4.2}$$

where the kernel is a two-point correlation tensor: $R_{i,j}(\mathbf{x},\mathbf{x}',t,t') = \langle u_i(\mathbf{x},t)u_j(\mathbf{x}',t')\rangle$. For fields with finite total energy, i.e, statistically inhomogeneous fields, the Hilbert-Schmidt theory ensures denumerable set of solutions for Eq. 4.2 given by eigenfunctions, $\psi_i^{(n)}(\mathbf{x},t)$ and corresponding eigenvalues, $\lambda^{(n)}$ (Ref. [86]).

Axisymmetric wakes are homogeneous in azimuthal direction (θ) and stationary in time and therefore the Hilbert Schmidt theory doesn't apply. However, the POD modes are essentially Fourier modes in these directions. Now, if the flow field at a given downstream location (x) is considered then the POD description derived from Eq. 4.2 is only solved for radial direction r.

The approach adopted in this study is an amalgamation of works by Ref. [76] and Ref. [88] and is detailed below:

1. Obtain multiple snapshots of the streamwise velocity fluctuations ($u_x(r,\theta,t)$) at fixed downstream locations (x).

2. Expand the fluctuations in azimuthal direction (θ) using Fourier decomposition for each snapshot:

$$\hat{u_x}(r,m,t;x) = \frac{1}{2\pi}\int_0^{2\pi} u_x(r,\theta,t;x)e^{-im\theta}d\theta \tag{4.3}$$

   where m is the discrete azimuthal mode number characterizing the dependence of length scales in θ direction.

3. For each azimuthal mode m, use $\hat{u}(r,m,t;x)$ and perform a Fourier transform in time based on the number of snapshots and windowing using the Welch's algorithm to obtain the corresponding Fourier amplitudes $\tilde{u_x}(r,m,f;x)$.

4. Construct a cross-spectral density tensor, $S_{x,x}(r,r',f,m;x) = \langle \tilde{u_x}(r,m,f;x)\tilde{u_x}(r',m,f;x)\rangle$ and solve the following integral equation in radial direction:

$$\int S_{x,x}(m,f,r,r';x)\psi^{(n)}(m,f,r';x)r'dr' = \lambda^{(n)}(m,f;x)\psi^{(n)}(m,f,r;x) \tag{4.4}$$

   In the non-homogeneous radial direction, there exists a denumerable set of discrete radial POD modes ($\psi^{(n)}(r,m,f;x)$) and modal energy content ($\lambda^{(n)}(m,f;x)$) from the Hilbert-Schmidt theory. The radial POD mode number, n characterizes the dependence of length scales in r direction.

The last two steps are computed using a spectral POD technique outlined in Ref. [88] capable of capturing the spatio-temporal behavior of structures. Based on the above approach, the large scales in axisymmetric wakes are completely described in terms of the azimuthal mode number (m), frequency (f) and the radial mode number (n) at fixed downstream locations (x).

Large-scale coherent structure analysis in axisymmetric wake of a disk [86, 1] and an axisymmetric bluff body with blunt trailing edge [89, 90] reveals dominance of different azimuthal modes as a function of downstream location in the wake. A schematic of the structure of axisymmetric wake of a disk is illustrated in Fig. 4.1 where three dominant azimuthal modes have been identified. The azimuthal mode, $m = 0$, arising from axisymmetric fluctuations due to expansion and contraction of the recirculation bubble, is called the 'bubble-pumping' mode. Although, study by Ref. [74] found negligible contribution from the $m = 0$ mode in the wake of a disk, subsequent studies found this mode to have sufficient energy even in the far wake region [86] of axisymmetric bodies. The azimuthal mode, $m = 1$ is the most dominant mode reported in literature in the wakes of axisymmetric bodies. This anti-symmetric mode is associated with shedding of large-scale coherent structures at the vortex shedding frequency (f_{vs}) and is responsible for the helical shape of the turbulent wake [1]. A low frequency azimuthal mode, $m = 2$ has also been detected in the axisymmetric wake studies [74, 86]. Although the correlation of this mode with the coherent structures in the wake is unclear, this mode appears to be dominant in the far-wake region ($x/D > 30$) when the wake approaches self-similarity [86].

Surprisingly, behavior of modes characterizing the large-scale structures in the sphere's wake has not been investigated thoroughly. Ref. [1] claimed the wake of a sphere to be similar to a disk in terms of modal behavior below $Re_{cr} \approx 2 \times 10^5$. They, however, did not investigate the details of the modal composition in the near-wake region of a sphere. Consequently, there is a clear need to examine the coherent structure dynamics in the wake of a sphere in detail. In the next section we detail the SRS turbulence modeling approach utilized in this study.

4.3 Description of partially-averaged Navier-Stokes (PANS) closure

In the present study, unresolved/modeled scales are computed using a PANS $k_u - \omega_u$ model proposed in Ref. [62]. The unresolved eddy viscosity (ν_u) from Eq. 2.10 is determined as:

$$\nu_u = \frac{k_u}{\omega_u} \tag{4.5}$$

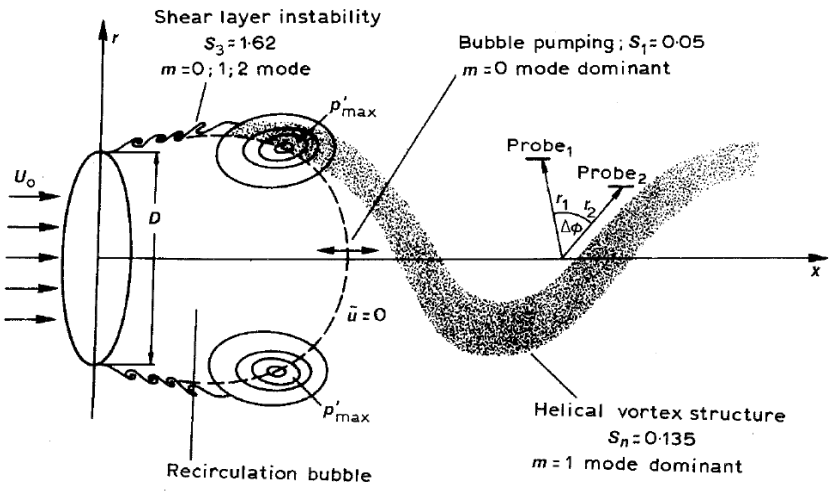

Figure 4.1: Schematic of disk wake structure (Reprinted from Journal of Fluids and Structures, Vol 4, E. Berger, D. Scholz, and M. Schumm, Coherent vortex structures in the wake of a sphere and a circular disk at rest and under forced vibrations, 27, Copyright (1990), with permission from Elsevier [1].)

Here, ω_u is the specific rate of dissipation. Evolution equations for k_u and ω_u are given as:

$$\frac{\partial k_u}{\partial t} + U_j \frac{\partial k_u}{\partial x_j} = P_u - \beta^* k_u \omega_u + \frac{\partial}{\partial x_j}\left[\left(\nu + \frac{\nu_u}{\sigma_{ku}}\right)\frac{\partial k_u}{\partial x_j}\right] \tag{4.6}$$

$$\frac{\partial \omega_u}{\partial t} + U_j \frac{\partial \omega_u}{\partial x_j} = \alpha \frac{P_u \omega_u}{k_u} - \beta' \omega_u^2 + \frac{\partial}{\partial x_j}\left[\left(\nu + \frac{\nu_u}{\sigma_{\omega u}}\right)\frac{\partial \omega_u}{\partial x_j}\right] \tag{4.7}$$

where $P_u = \tau(V_i, V_j)\frac{\partial U_i}{\partial x_j}$ is the production in the unresolved scales. Closure coefficients from Eqs. 4.6 and 4.7 are determined as follows [62]:

$$\beta' = \alpha\beta^* - \alpha\frac{\beta^*}{f_\omega} + \frac{\beta}{f_\omega} \tag{4.8}$$

$$\sigma_{ku} = \frac{f_k}{f_\omega}\sigma_k; \;\; \sigma_{\omega u} = \frac{f_k}{f_\omega}\sigma_\omega \tag{4.9}$$

The remaining RANS $k-\omega$ model coefficients used are: $\beta^* = 0.09$, $\alpha = 5/9$, $\beta = 0.075$, $\sigma_k = 2.0$ and $\sigma_\omega = 2.0$.

4.4 Numerical setup

Flow past a sphere at subcritical Reynolds number, based on freestream velocity (V_∞) and the diameter of the sphere (D), $Re = V_\infty D/\nu$ of 3700 is simulated. In this section, we establish the flow domain and numerical features of this study.

4.4.1 Domain and boundary conditions

A cylindrical computational domain is constructed with the sphere located at $(x,y,z) = (0,0,0)$ as shown in Fig. 4.2. The inlet is at $x/D = -5$ from the sphere and the domain in the wake extends to $x/D = 30$. The cylindrical domain expands to $r/D = 5$ in the radial direction. The equations are solved in a Cartesian coordinate system and the dependence of velocity field on the radial (r) and azimuthal (θ) directions is obtained using the coordinate transformation. Boundary conditions analogous to the DNS of Ref. [2] and the LES of Ref. [78] are used in this study. A Dirichlet boundary condition of uniform flow in streamwise direction, $(U_x, U_y, U_z) = (V_\infty, 0, 0)$, is prescribed at the inlet and the far-field boundaries. Moreover, turbulence intensity, $I = 0.2\%$, eddy viscosity $\nu_T/\nu = 10^{-3}$ and non-dimensional specific rate of dissipation $\omega^* = 20$ are maintained at the inflow boundaries. No-slip boundary condition is specified for velocity at the sphere's surface. Turbulence quantities (k, ν_T) and the normal derivative of pressure are set to zero, whereas the specific dissipation rate, $\omega = 6\nu/\beta d^2$ [19] is used on the surface of the sphere, where d is the distance to nearest cell center from the sphere's surface. A convective boundary condition is employed at the outlet. For the PANS simulations performed in this study, unresolved or modeled turbulence quantities are specified at the boundaries: unresolved turbulent kinetic energy ($k_u = f_k k$) and unresolved specific dissipation rate ($\omega_u = f_\omega \omega$). The unresolved eddy viscosity is then prescribed as $\nu_u = (f_k/f_\omega)\nu_T$.

4.4.2 Numerical schemes

The finite-volume code, OpenFOAM [91] is employed for all the simulations performed in this study. Second-order accurate schemes are chosen for spatial discretization and a second-order implicit backward scheme is used to discretize the temporal derivatives. The Pressure-Implicit

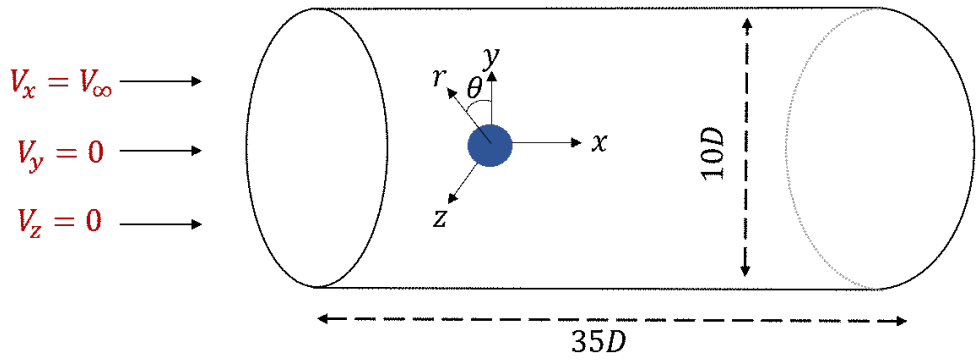

Figure 4.2: Computational domain

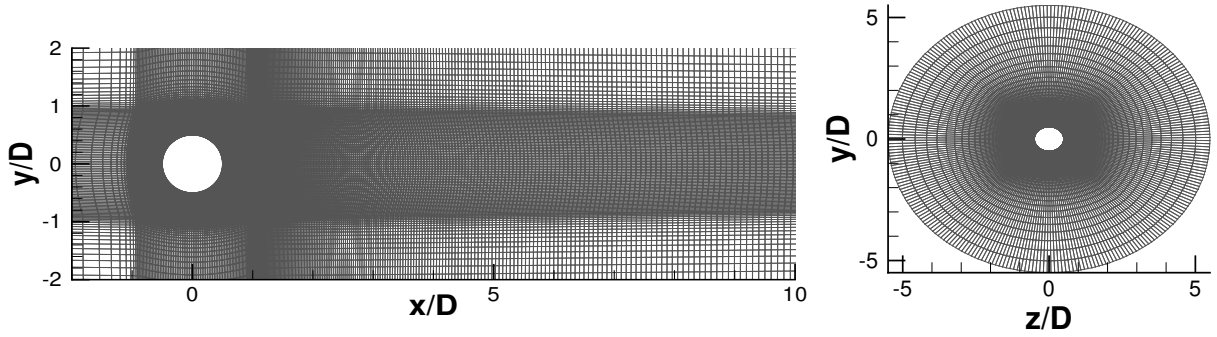

Figure 4.3: Grid configuration: grid resolution near the sphere in the streamwise axis plane (left) and in the cross-sectional plane normal to the streamwise axis (right).

with Splitting of Operators (PISO) algorithm is used for the pressure–velocity coupling [71]. The resulting algebraic equations are solved using a geometric agglomerated algebraic multigrid solver for pressure and an iterative solver using a symmetric Gauss–Seidel smoother for all other flow variables. A tolerance of 10^{-8} is maintained for convergence of all the variables at each time step.

4.4.3 Numerical grid and convergence of flow statistics

A multi-block structured grid within a cylindrical domain is constructed using ANSYS ICEM with hexahedral elements. An overview of the mesh characteristics is presented in Table. 4.1 and the mesh configuration for the g_2 mesh is presented in Fig. 4.3 for both the (x,y) and (y,z) planes. A consistent grid configuration is maintained in the (x,r) plane for each azimuthal angle θ. The sphere is enclosed with a body-fitted radially expanding mesh for $0.5 \leq r/D \leq 1$ with $\Delta r_{max}/D =$

Table 4.1: Mesh parameters; N_t is the total number of cells in the domain, N_{cs} is the total number of cells in the cross-sectional plane (perpendicular to the streamwise axis), $\Delta r^+_{min} = \Delta r_{min}/D$ is the radial displacement of cells adjacent to sphere's surface, $\Delta t^+ = \Delta t V_\infty/D$ is the uniform non-dimensional time step and $\Delta T^+ = \Delta T V_\infty/D$ is the averaging interval for the statistics.

Study	Grid Type	$N_t(10^6)$	N_{cs}	Δr^+_{min}	Δt^+	ΔT^+
PANS ($f_k = 0.5$)	Structured	6.09	12,784	0.003	$3.7X10^{-3}$	200
PANS ($f_k = 0.3$)	Structured	6.09	12,784	0.003	$3.7X10^{-3}$	200
PANS ($f_k = 0.2$)						
g_1	Structured	3.82	12,320	0.01	$3.7X10^{-3}$	150
g_2	Structured	6.18	13,345	0.01	$3.7X10^{-3}$	150
g_3	Structured	7.52	14,981	0.003	$2.96X10^{-3}$	250
PANS ($f_k = 0.1$)	Structured	8.82	17,025	0.003	$1.85X10^{-3}$	300
DNS [2]	Unstructured	9.48	-	-	-	350
DNS [82]	Structured	372.77	80,896	0.0016	-	80
LES [78]	Structured (IBM)	9.08	12,880	-	$1X10^{-2}$	800

0.1 for g_1 mesh. In the near-wake region ($0.5 \leq x/D \leq 5$), approximately $170-250$ nodes are placed in the x-direction with $\Delta x_{max}/D = 0.05-0.11$ for different meshes. While unstructured grids (DNS [2]) or immersed boundary methods (IBMs) used in LES of Ref. [78], require lesser number of grid cells, a Cartesian mesh is considered for seamless compatibility with OpenFOAM solvers. The results from grid resolution study for the case of $f_k = 0.2$ are presented in Fig. 4.4. First-order statistics are compared against the DNS study of Ref. [2]. Better agreement is observed for finer grid resolutions, g_2 and g_3. Therefore, in subsequent sections, results from g_3 mesh are examined for the $f_k = 0.2$ case. Similar study is conducted for PANS $f_k = 0.5, 0.3$ cases and the corresponding meshes presented in Table 4.1 are found optimal.

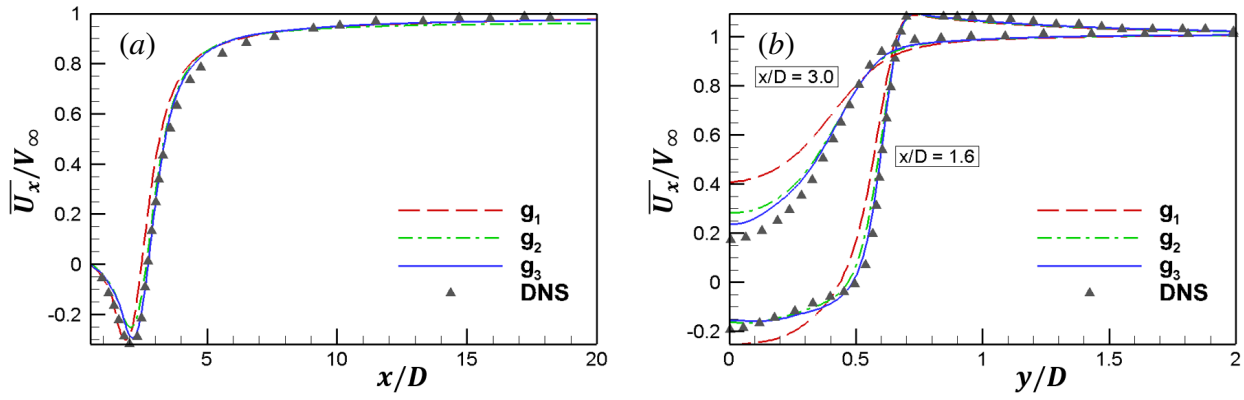

Figure 4.4: Grid convergence study: (a) time-averaged streamwise velocity profile at the centerline and (b) time-averaged streamwise velocity profile at different locations in the near-wake; DNS results from Ref. [2] are used for comparison.

4.5 Results

The objective of this work is to examine the ability of PANS-SRS simulations to capture flow statistics, spectral behavior and large-scale structures as a function of physical resolution, f_k. According to the results of Refs. [42, 46], satisfactory predictions from PANS simulations are observed for $f_k \leq 0.5$ for 2D bluff body wakes. For coarser physical resolutions, $f_k > 0.5$, key instabilities in the flow field are not resolved leading to poor predictions. Therefore, high resolution PANS simulations of statistically 3D wake with $f_k \leq 0.5$ are considered in this study.

We start by examining integral quantities and the first- and second-order statistics computed from the simulations and examine the degree of agreement with established results in literature. Next, we discuss the spectral behavior at specific probe locations. Finally, we perform an investigation of the large-scale coherent structures in the wake of the sphere.

4.5.1 Integral quantities and flow statistics

The integral flow quantities are compared in Table. 4.2. At all f_k values, the PANS quantities compare well with the corresponding DNS data. The separation angle ($\phi_s(^o)$) of about 90^o (for a laminar boundary layer separation) is well captured by all PANS-SRS simulations.

Now, we investigate the effect of physical resolution (f_k) variation on the first- and second-order

Table 4.2: Integral quantities; Time-averaged drag coefficient $\overline{C_d}$, root-mean-square lift coefficient $C_l(RMS)$, Strouhal number S_t, recirculation length L_R, time-averaged base pressure coefficient $\overline{C_{pb}}$ and separation angle $\phi_s(^o)$

Study	$\overline{C_d}$	$C_l(RMS)$	S_t	L_R	$\overline{C_{pb}}$	$\phi_s(^o)$
PANS ($f_k = 0.5$)	0.395	0.0115	0.201	2.23	-0.221	89.97
PANS ($f_k = 0.3$)	0.396	0.0082	0.216	2.24	-0.221	89.82
PANS ($f_k = 0.2$)	0.395	0.0079	0.204	2.26	-0.220	89.83
PANS ($f_k = 0.1$)	0.396	0.0070	0.217	2.24	-0.220	89.79
DNS [2]	0.394	–	0.215	2.28	-0.207	89.4
LES [78]	0.355	–	0.21	2.622	-0.194	90

statistics in the wake of the sphere. The mean pressure coefficient, $\overline{C_p}$ over the sphere's surface is in excellent agreement with the DNS study of Ref. [2] as seen from Fig. 4.5(a). Although minor deviations are observed in the back pressure coefficient, $\overline{C_{pb}}$ (see Table. 4.2), the profile and the pressure minimum location ($\theta_{p_{min}} = 71.5^o$) are captured precisely for all f_k. The time-averaged streamwise velocity ($\overline{U_x}$) profile along the wake centerline is presented in Fig. 4.5(b). The recirculation bubble is estimated with reasonable accuracy at all resolutions. A maximum error of 28% (for PANS $f_k = 0.5$) is observed in the minimum mean streamwise velocity ($\overline{U_x}$) at $x/D = 2.13$ on the wake centerline compared to the DNS study. For finer f_k resolutions, the agreement is significantly better.

Mean streamwise ($\overline{U_x}$) and radial ($\overline{U_r}$) velocity profiles at different downstream locations in the wake are illustrated in Fig. 4.6. The 'U' shaped profile inside the recirculation region (see, Fig. 4.6(a)) is well replicated at all resolution levels. The simulations deviate from the DNS results at $x/D = 5.0$ as seen in Fig. 4.6(g). All PANS simulations compute a lower velocity deficit compared to the DNS along with a slower recovery in the radial direction. For the low resolution runs ($f_k = 0.5, 0.3$), higher velocity fluid in the wake's core is observed at $x/D = 10$ (Fig. 4.6(i)).

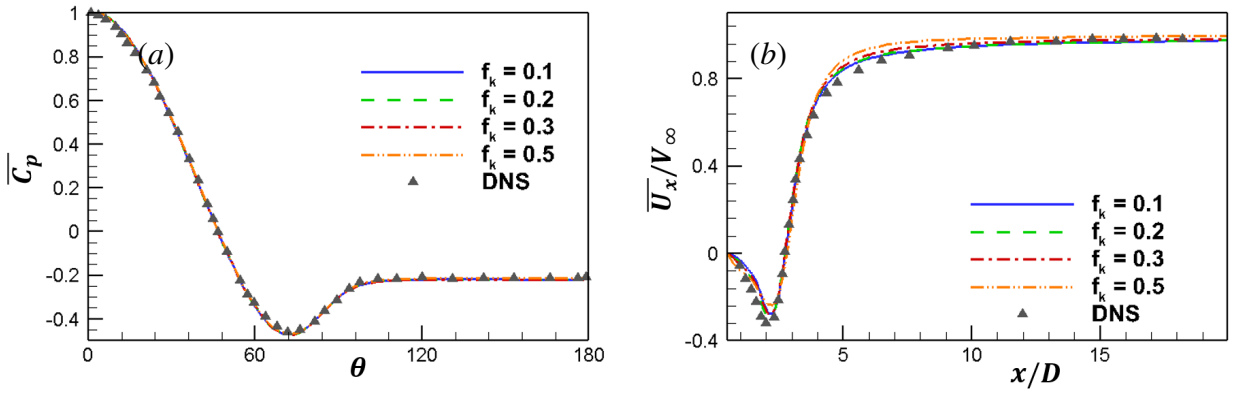

Figure 4.5: (a) Mean pressure coefficient around the sphere and (b) streamwise velocity profile in the centerline for different physical resolutions (f_k) compared to DNS of Ref. [2].

For simulations with $f_k \leq 0.2$, the mean streamwise velocity profiles recover well and are in good agreement with DNS. The radial velocity ($\overline{U_r}$) profiles show slight deviations from the DNS values, especially for $f_k = 0.5$ simulation.

Profiles of the total turbulent kinetic energy (k_T/V_∞^2) at different downstream locations are shown in Fig. 4.7. The second-order quantities have contributions from both resolved flow fluctuations and the modeled quantities. In the immediate vicinity of the sphere ($x/D = 1.6$), streamwise fluctuations ($\overline{u_x u_x}$) dominate in the separating shear layers ($r/D = 0.6$) arising from the underlying KH instability. This instability generates smaller scales in the recirculation region aiding the transition to turbulence beyond $x/D = 2.0$. At the end of the recirculation region, peak values of turbulent stresses ($\overline{u_x u_x}$, $\overline{u_r u_r}$ and $\overline{u_x u_r}$) are obtained between $x/D = 2.0 - 3.0$ leading to a corresponding peak in total turbulent kinetic energy (Fig. 4.7(c)). As smaller scales are generated at the location of transition to turbulence, a larger averaging window is required for finer physical resolution simulations (see, Fig. 4.7(b)) for convergence of higher order statistics. Beyond the recirculation region, the turbulent kinetic energy is convected downstream by the large-scale motions. Overall, the results improve substantially with decreasing f_k.

Based on the results in this section, it is clear that the integral quantities and one-point flow statistics are reasonably captured by the PANS simulations at most physical resolutions, f_k. In the

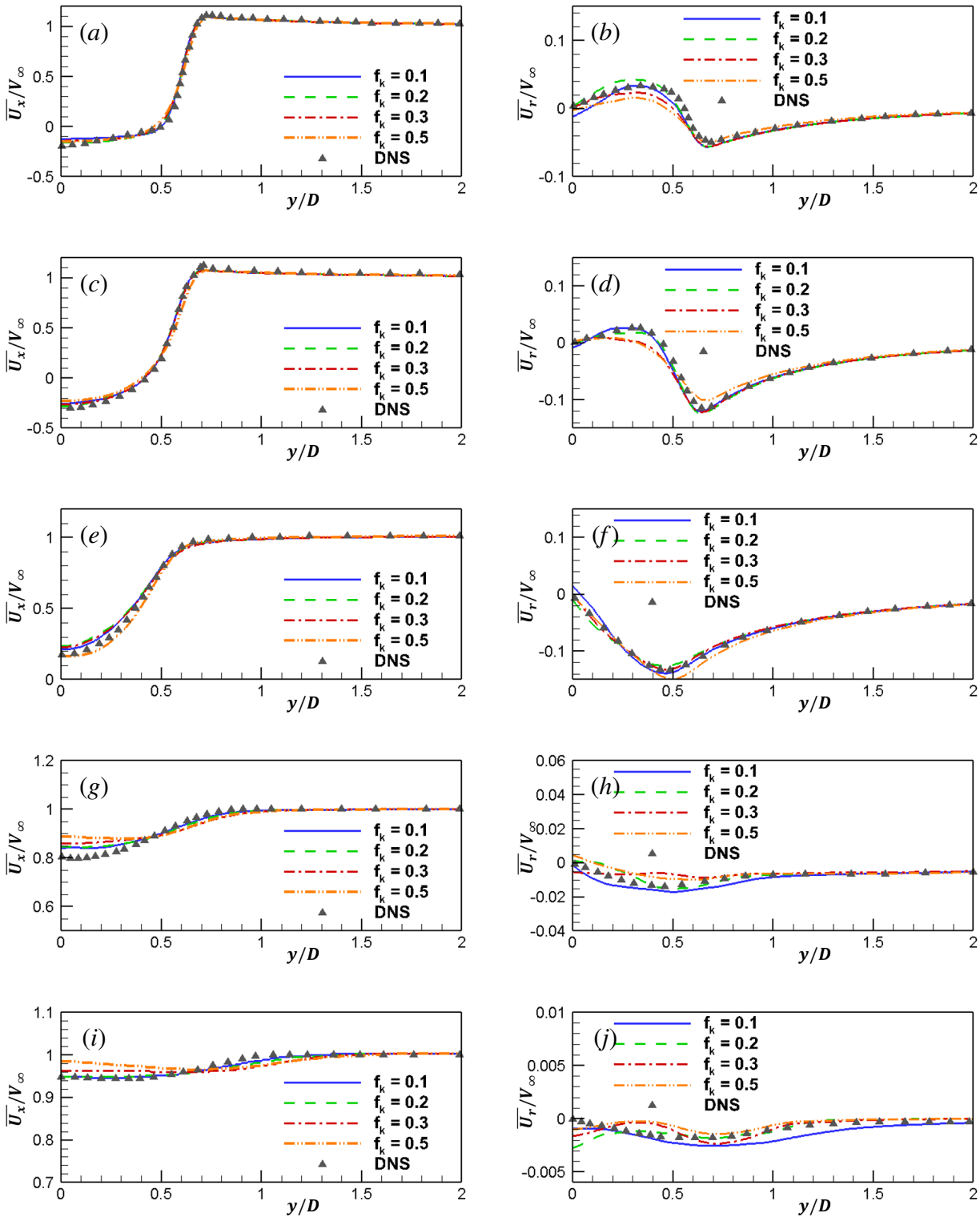

Figure 4.6: Time-averaged streamwise and radial velocity profiles in $z = 0$ plane for $x/D = 1.6$ ((a),(b)), $x/D = 2.0$ ((c),(d)), $x/D = 3.0$ ((e),(f)), $x/D = 5.0$ ((g),(h)) and $x/D = 10.0$ ((i),(j)). Results are compared to DNS of Ref. [2].

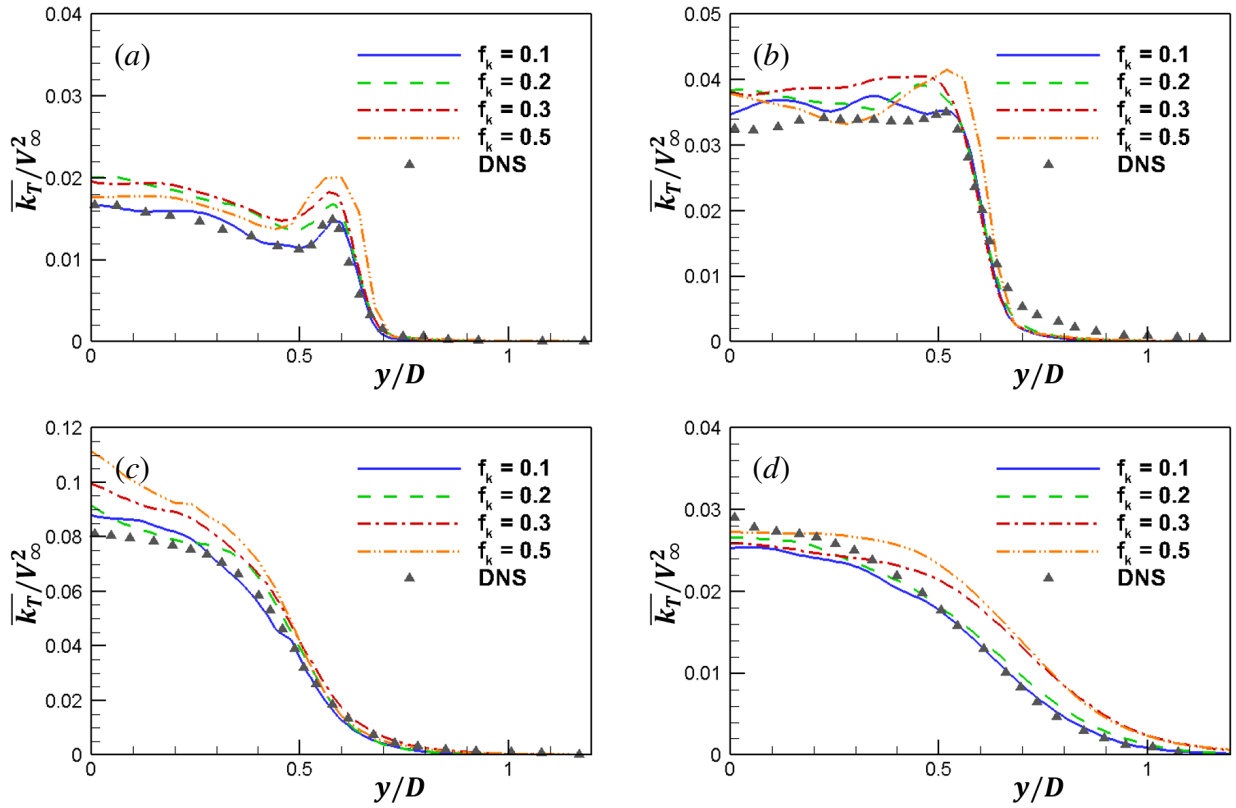

Figure 4.7: Total turbulent kinetic energy, k_T (resolved + modeled (k_u)) in $z = 0$ plane for (a) $x/D = 1.6$, (b) $x/D = 2.0$, (c) $x/D = 3.0$ and (d) $x/D = 5.0$. Results are compared to DNS of Ref. [3].

next sub-sections, we assess the ability of PANS to resolve key instabilities in the flow and capture large-scale coherent structures at different resolutions (f_k values).

4.5.2 Resolution of key instabilities and spectral behavior

Flow past a sphere exhibits two main instabilities[5]; (i) a large-scale instability associated with shedding of coherent structures from the end of the recirculation region and (ii) a small-scale instability associated with pulsation of the detached shear layer due to formation and spatial development of Kelvin-Helmholtz (KH) rollers. The first large-scale vortex shedding instability manifests as a progressive wave motion beyond critical Reynolds number, $Re_{c1} = 280$. Beyond the second critical Reynolds number, $Re_{c2} = 800$, the second small-scale instability (spiral mode) is present on the periphery of the recirculation region. Toward resolution of these key instabilities, it is essential to ensure that the effective computational Reynolds number (Re_{eff}) obtained from Eq. 2.14 exceeds the critical Reynolds number of these instabilities [46]. The small-scale KH instability acts along the locus of inflection-point for the velocity field ($\partial^2\overline{U_x}/\partial r^2 = 0$). To ensure this instability fully manifests, $Re_{eff} > Re_{c2}$ around the inflection line. The contours of the effective computational Reynolds number are presented in Fig. 4.8. The results clearly illustrate the ability of PANS simulations with $f_k \leq 0.3$ to capture both the key instabilities in the flow reasonably well. Although for the $f_k = 0.5$ simulation the inflection line doesn't encounter a region where $Re_{eff} \leq 800$, the low Re_{eff} inside the recirculation region (Fig. 4.8(a)) clearly prohibits the underlying KH instability to develop completely.

The Welch's power spectral density distributions [92] of the radial velocity component (U_r) are presented in Figs. 4.9-4.10 at different probe locations (see, Fig. 4.8) in the wake. The first probe (Probe A) is placed at $x/D = 1.0, r/D = 0.6$ which is in the separated axisymmetric shear layer to capture the Kelvin-Helmholtz roll-up. This instability manifests as intermittent bursts of high amplitudes in the radial velocity time series. The PANS radial velocity spectra capture this instability as a broadband frequency centered around $f_{KH}D/V_\infty = 0.65 - 0.71$. These peaks are slightly lower from the value of $f_{KH}D/V_\infty = 0.72$ found in the DNS study [2]. A scatter in the values of this frequency is reported in the literature [77, 80]. This key instability is not distinctly

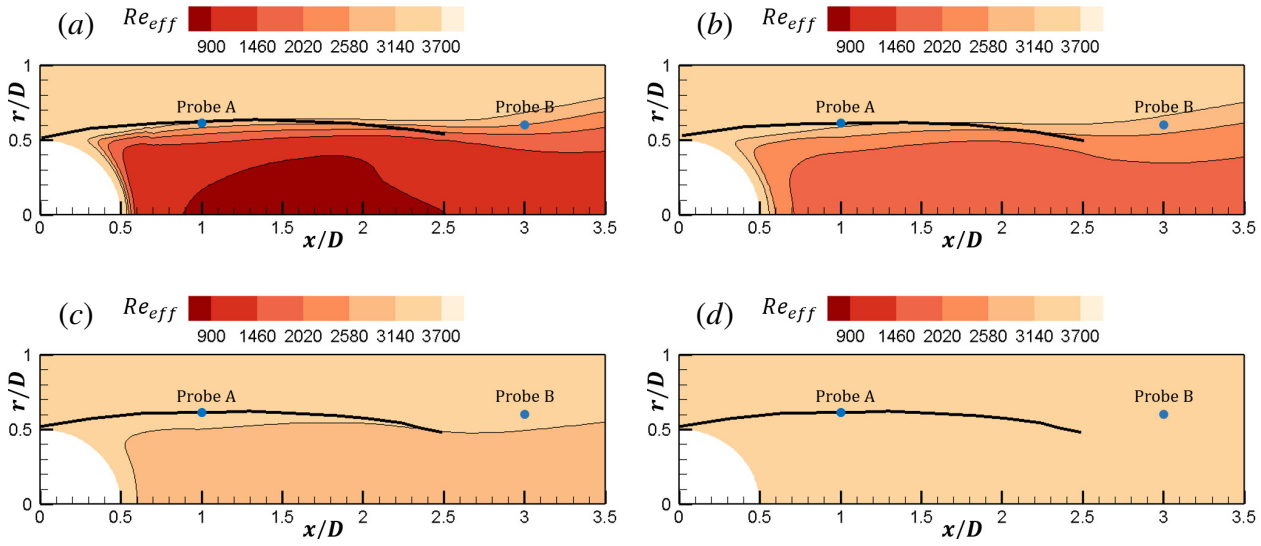

Figure 4.8: Contours of effective computational Reynolds number, Re_{eff}; (a) $f_k = 0.5$, (b) $f_k = 0.3$, (c) $f_k = 0.2$ and (d) $f_k = 0.1$. The dark line is the inflection line where $\partial^2 \overline{U_x}/\partial r^2 = 0$.

captured in the PANS $f_k = 0.5$ simulation (Fig. 4.9(a)) due to a higher eddy viscosity (ν_u) generated in the system (Eq. 2.13). The large-scale instability manifests as a vortex shedding f_{vs} frequency in the energy spectra and the value of $f_{vs}D/V_\infty \approx 0.21$ (Ref. [2]) has been reasonably captured by all PANS f_k simulations as shown in Fig. 4.9 (Probe B).

4.5.3 Large-scale vortex structures in the wake of a sphere

Qualitative aspects of the axisymmetric wake of a sphere are examined in detail at different physical resolutions. We now present a brief summary of the findings:

1. The vortex detachment location in the azimuthal direction (θ_s) based on the highest out-of-plane vorticity content is obtained at the downstream location $x/D = 3.0$. The detachment location (θ_s) is found to be randomly distributed in time for all f_k simulations.

2. The vortical structures are traced throughout their shedding cycle (T_s) along with their maximum out-of-plane vorticity content in the plane along the streamwise axis. The maximum vorticity content stays in the same plane throughout T_s for the vortical structures. This highlights the tendency of vortices to stay in the 'shedding plane' as they convect downstream.

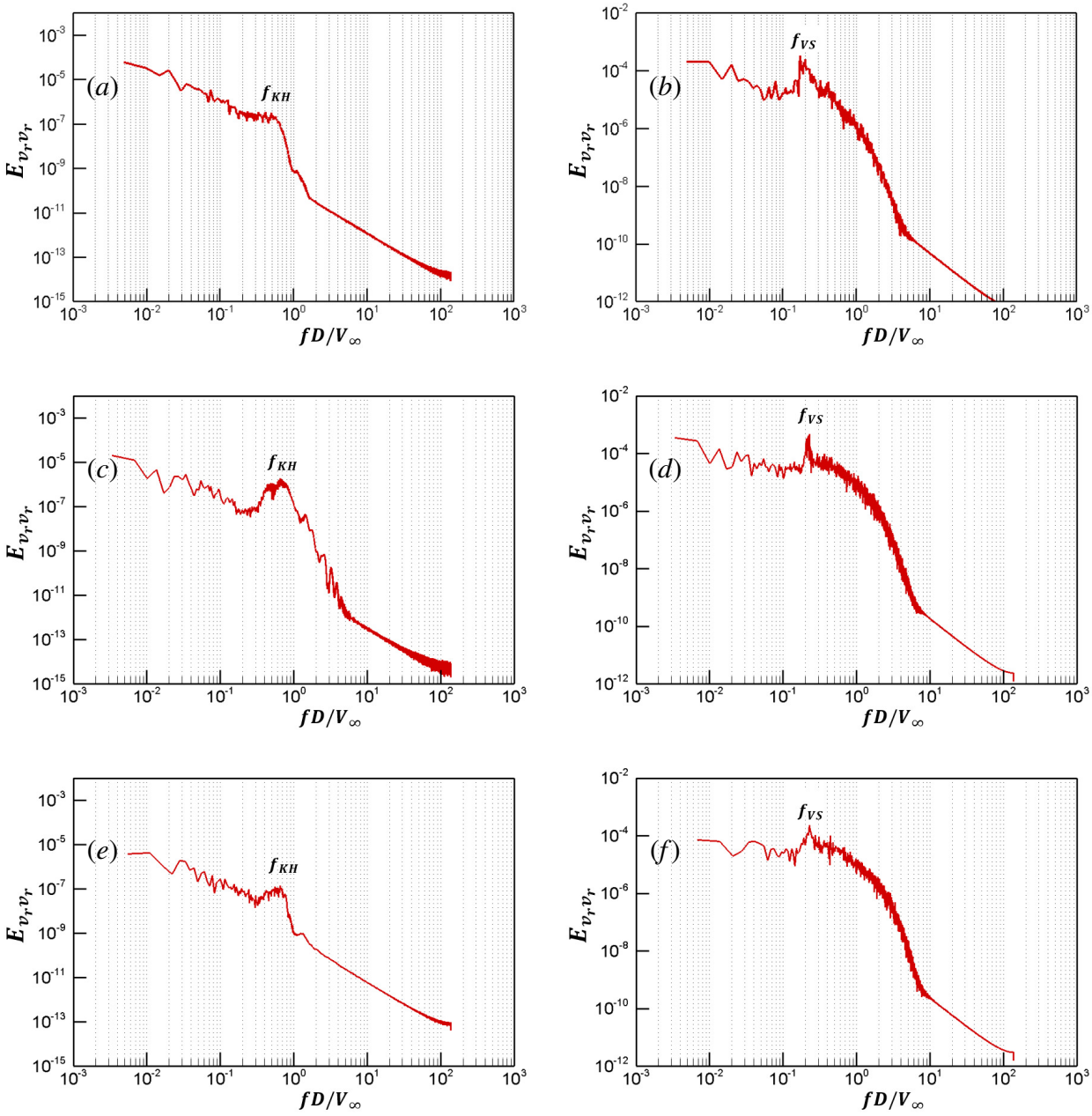

Figure 4.9: Caption on the next page.

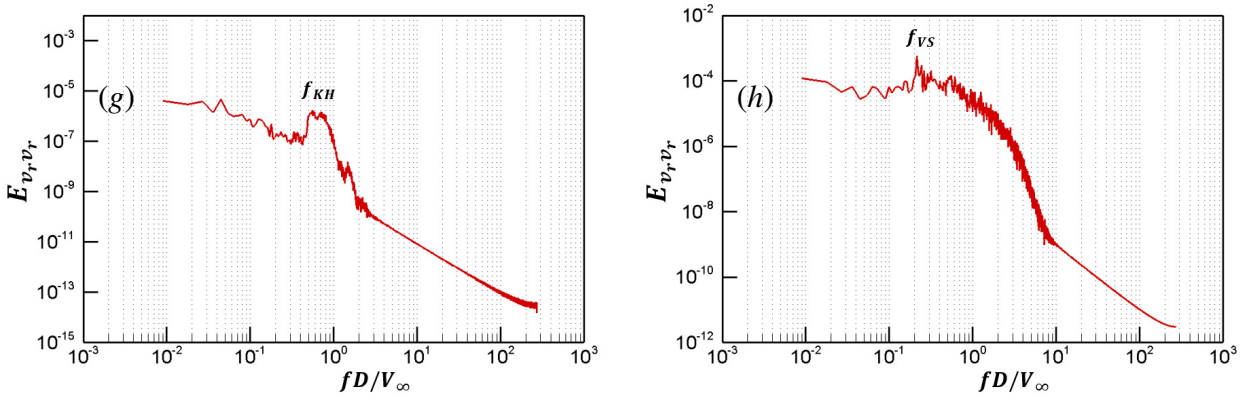

Figure 4.10: Radial velocity spectra at different probe locations in the wake; Probe A: $x/D = 1.0$, $r/D = 0.6$ ((a) $f_k = 0.5$, (c) $f_k = 0.3$, (e) $f_k = 0.2$, (g) $f_k = 0.1$) and Probe B: $x/D = 3.0$, $r/D = 0.6$ ((b) $f_k = 0.5$, (d) $f_k = 0.3$, (f) $f_k = 0.2$, (h) $f_k = 0.1$). The spectra are averaged from data at eight equally-spaced locations in azimuthal direction. (Caption also includes Fig. 4.9)

These findings are in accordance with the results of Ref. [5] and Ref. [78]. Iso-surfaces of $Q = \frac{1}{2}(\Omega^2 - S^2)$ where Ω and S are the antisymmetric and symmetric components of the velocity gradient tensor, are presented in Fig. 4.11 for different PANS simulations. An axisymmetric vortical structure in the detached shear layers is readily discernible from the figure which corresponds to the presence of vortex tubes [5]. These tubes then coalesce to form the large-scale structures which are shed quasi-randomly in the wake. Hairpin-like structures in the wake are seen in all PANS simulations. As the physical resolution improves (reduction in f_k), a wider range of scales are observed in the wake.

We quantify the structures generated from the PANS simulations using a POD technique. This procedure, outlined in Section. 4.2, is applied at fixed downstream locations in the wake to examine near-wake coherent structures at different degrees of physical resolution, f_k. Based on eigenvalue decomposition of the cross-spectral density tensor, $S(r, r', m, f; x)$ (Eq. 4.4), the radial POD modal energy content $\lambda^{(n)}(m, f; x)$ and corresponding mode shapes ($\psi^{(n)}(r, m, f; x)$) can be obtained as a function of azimuthal mode (m) and frequency (f). As the POD arranges the modes based on their energy content, only the first few radial POD modes are analyzed to establish the ability of PANS to capture the dominant coherent structures at different resolutions. Based on the analysis in

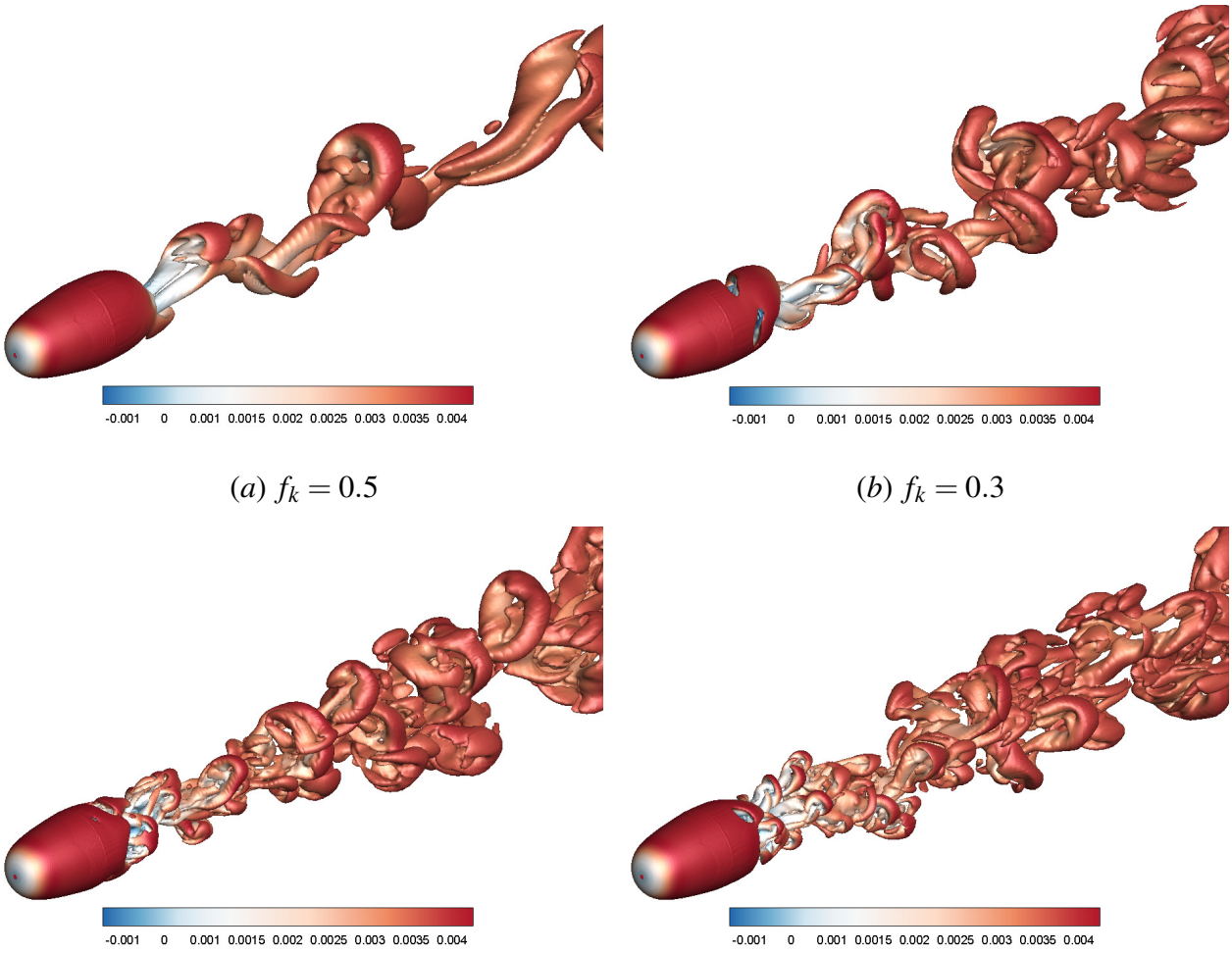

(*a*) $f_k = 0.5$ (*b*) $f_k = 0.3$

(*c*) $f_k = 0.2$ (*d*) $f_k = 0.1$

Figure 4.11: Instantaneous Q-factor iso-surfaces for different f_k ((a) $f_k = 0.5$, (b) $f_k = 0.3$, (c) $f_k = 0.2$ and (d) $f_k = 0.1$) simulations colored with resolved streamwise velocity U_x.

this study, the first radial POD mode ($n = 1$) contains approximately $80 - 85\%$ of the total energy in the radial direction for the peak frequency over different azimuthal mode number (m) for all f_k simulations. Therefore, in the subsequent analysis, only the first radial POD mode ($\psi^1(r,m,f;x)$, $\lambda^1(m,f,;x)$) is investigated in detail. The data from the numerical domain is mapped onto a cylindrical polar grid with $r \in [0,\ 1.5D]$, $\theta \in [0^o,\ 360^o]$ and $z \in [1D,\ 10D]$. The snapshots are obtained at four stations in the wake of the sphere; (i) inside the recirculation region, $x/D = 2.0$, (ii) just outside the recirculation region, $x/D = 3.0$, (ii) in the near-wake region, $x/D = 5.0$ and (iv) in the intermediate wake region, $x/D = 10.0$. A total of approximately 2000 snapshots at $\Delta t_{snaps} = 30V_\infty/D$ on a polar grid ($N_r = 50$, $N_\theta = 180$) with $\Delta r/D = 0.03$ and $\Delta\theta = 2^o$ are used to perform POD for all f_k resolutions.

We first investigate the spectral behavior of the azimuthal modes (m) using eigenspectra, $\lambda^1(m,f;x)$ as a function of normalized frequency at different downstream locations as presented in Fig. 4.12 for $f_k = 0.1$ simulation. Studies by Ref. [1] and Ref. [89] report the first azimuthal mode $m = 0$ oscillates at a low frequency of $S_t = 0.05 - 0.06$. From Fig. 4.12, a concentration of energy at frequency of around $S_t = 0.05$ can be deduced at $x/D = 5.0$ and 10.0. The most widely studied mode in the wake is the $m = 1$ mode associated with the large-scale vortex shedding. Fig. 4.12 clearly illustrates this oscillatory mode to peak at the natural shedding frequency of $S_t = 0.21$ at all downstream locations. Ref. [86] establish that the azimuthal mode $m = 2$ peaks at a near-zero frequency beyond $x/D = 30.0$. This low-frequency peak is captured at $S_t = 0.1$ by Ref. [89]. In the present PANS simulations, this peak is observed at the downstream stations, $x/D = 5.0$ and 10.0. With the temporal frequency behavior of the modes established, we now investigate the mode shapes of different azimuthal modes at their corresponding peak frequencies, i.e., $fD/V_\infty = 0.05$ for $m = 0$, $fD/V_\infty = 0.21$ for $m = 1$ and $fD/V_\infty = 0.1$ for $m = 2$.

The eigenfunctions ($\psi^1(r,m,f;x)$) obtained from the PANS simulation of $f_k = 0.1$ at different locations in the wake are presented in Fig. 4.13. These modes shapes are pre-multiplied by $r^{1/2}$ to make the kernel in Eq. 4.4 Hermitian symmetric [86]. Inside the recirculation region, at $x/D = 2.0$, the mode $m = 1$ lacks a clear defined shape as small-scales are generated inside the bubble

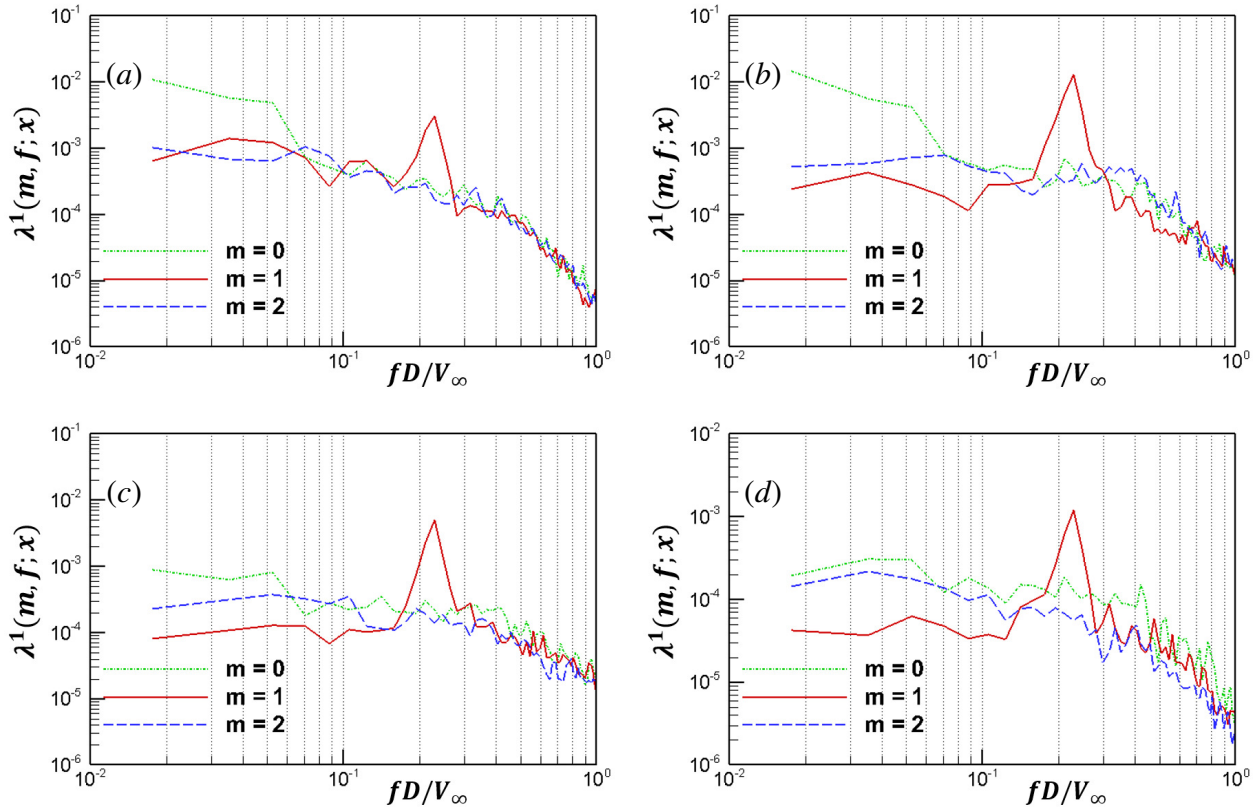

Figure 4.12: Eigenspectra $\lambda^1(m,f;x)$ at different downstream locations; (a) $x/D = 2.0$, (b) $x/D = 3.0$, (c) $x/D = 5.0$ and (d) $x/D = 10.0$ in the wake for PANS $f_k = 0.1$ simulation.

that interact with and distort the large-scale structures (Fig. 4.13(b)). At locations beyond $x/D \geq 3.0$, a signature anti-symmetric pattern of the $m = 1$ mode is clearly observed (Fig. 4.13(e), (h), (k)). The $m = 2$ mode retains its shape at all locations in the wake unaffected by the small-scale dynamics inside the recirculation region. A comparison of eigenfunctions for different physical resolution (f_k) at different locations in the wake is presented in Fig. 4.14. The results clearly illustrate a monotonic convergence of shapes of the large-scale behavior with improving physical resolution (decreasing f_k). The low resolution simulation of $f_k = 0.5$ fails to capture the mode shapes accurately, especially inside the recirculation region. Clearly, the mode shapes expand in radial direction as the wake grows and at $x/D = 10.0$ (Fig. 4.14(j), (k), (l)) large-scale structures diffuse more rapidly for coarser f_k simulations due to higher effective viscosity.

In order to analyze the kinetic energy distribution in different azimuthal modes (m), eigenspectra ($\lambda^{(n)}(m, f; x)$) integrated over frequency, ξ is proposed [76, 86]:

$$\xi^{(n)}(m; x) = \frac{\sum_f \lambda^{(n)}(m, f; x)}{\sum_n \sum_m \sum_f \lambda^{(n)}(m, f; x)} \tag{4.10}$$

The resulting normalized quantity illustrates the relative importance of the azimuthal modes governing the large-scale physics at different locations in the wake. The results for the first radial POD mode, $\xi^1(m; x)$ are presented in Fig. 4.15. The PANS $f_k = 0.2$ and $f_k = 0.1$ cases capture the dominance of $m = 0$ mode inside the recirculation bubble as illustrated in Fig. 4.15. The results clearly display convergence of modal energy content for higher physical resolutions ($f_k = 0.2,\ 0.1$). The PANS $f_k = 0.3$ results show slight dominance of the $m = 1$ mode compared to the $m = 0$ mode at $x/D = 2.0$. For the low-resolution PANS simulations, small-scales inside the recirculation region are not captured in detail which leads to inconsistent energy allocation among the modes. Note that the over-estimation of $m = 0$ mode by PANS $f_k = 0.5$ simulation at $x/D = 2.0$ is entirely due to the inability of $f_k = 0.5$ simulation to resolve small-scales at this location (also see Fig. 4.14(a)).

We can further examine the distribution of azimuthal modes in detail based on $\xi^1(m; x)$ by isolating results of PANS $f_k = 0.1$ simulation from Fig. 4.15. Inside the recirculation bubble, at

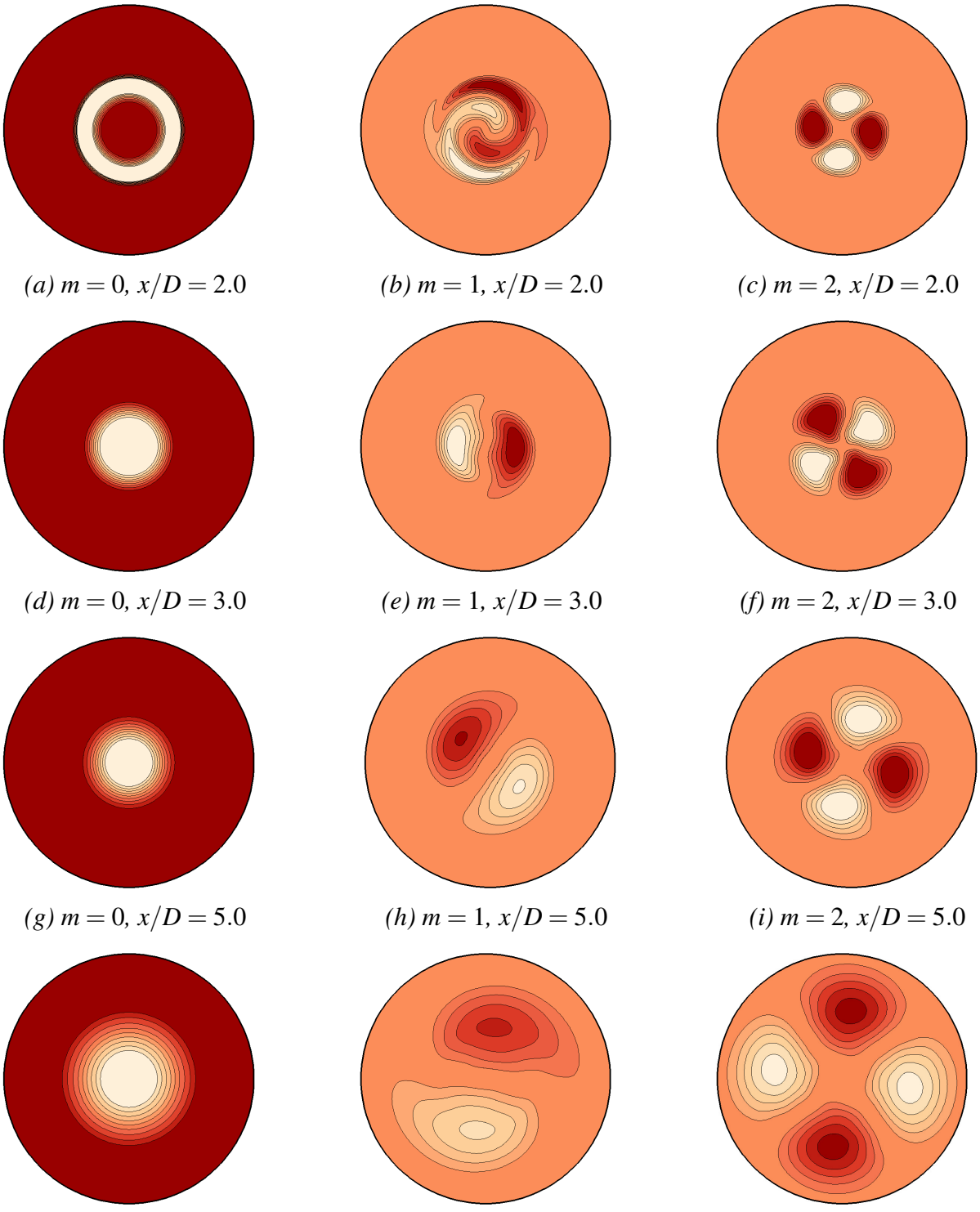

(a) $m = 0$, $x/D = 2.0$ *(b)* $m = 1$, $x/D = 2.0$ *(c)* $m = 2$, $x/D = 2.0$

(d) $m = 0$, $x/D = 3.0$ *(e)* $m = 1$, $x/D = 3.0$ *(f)* $m = 2$, $x/D = 3.0$

(g) $m = 0$, $x/D = 5.0$ *(h)* $m = 1$, $x/D = 5.0$ *(i)* $m = 2$, $x/D = 5.0$

(j) $m = 0$, $x/D = 10.0$ *(k)* $m = 1$, $x/D = 10.0$ *(l)* $m = 2$, $x/D = 10.0$

Figure 4.13: Azimuthal mode shapes ($r^{1/2}\psi^1(r,m,f;x)$) for $m = 0$ ((a), (d), (g) and (j)), $m = 1$ ((b), (e), (h) and (k)) and $m = 2$ ((c), (f), (i) and (l)) at different locations in the wake of the sphere. Results are obtained from PANS $f_k = 0.1$ simulation.

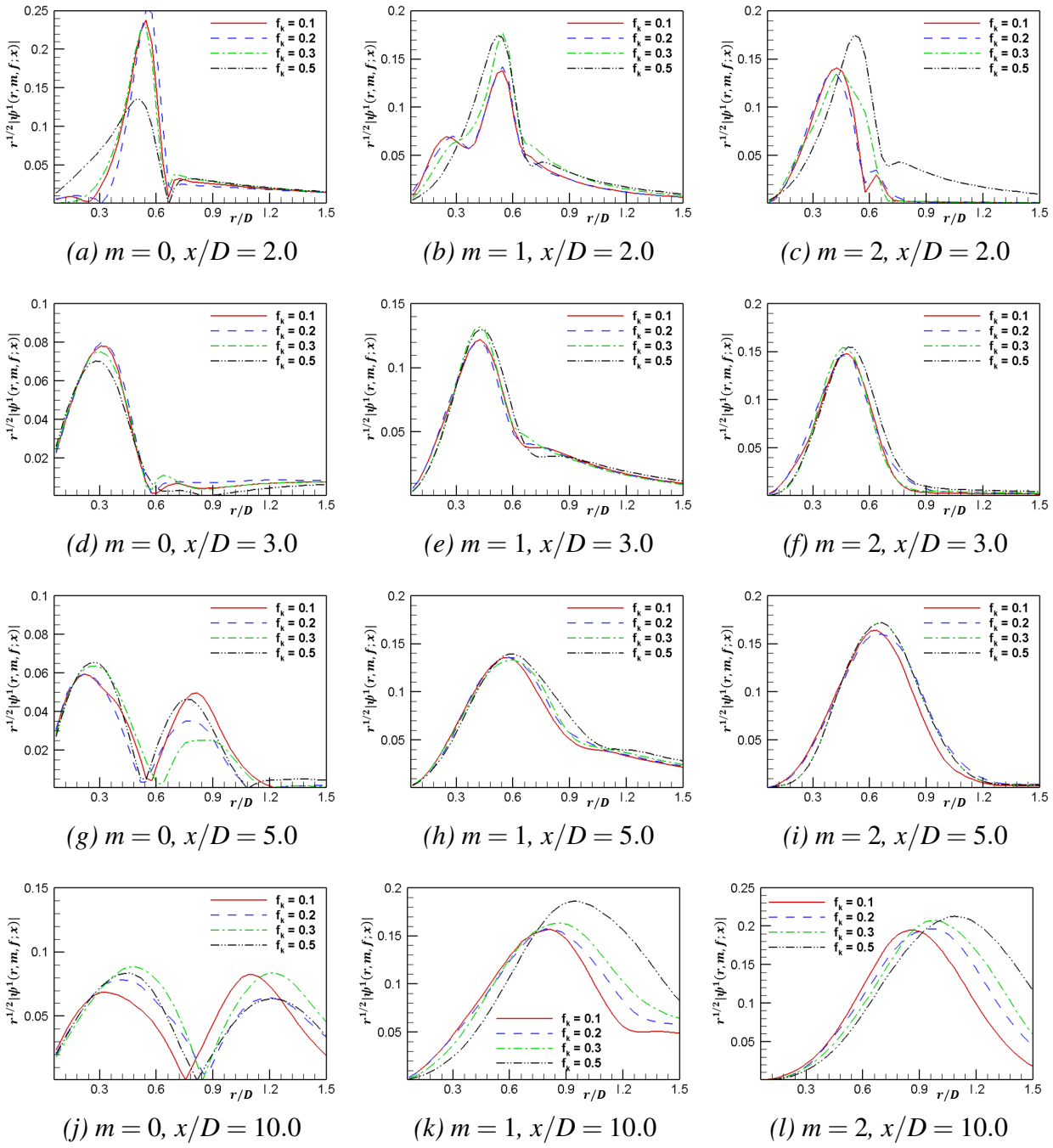

(a) $m = 0$, $x/D = 2.0$ (b) $m = 1$, $x/D = 2.0$ (c) $m = 2$, $x/D = 2.0$

(d) $m = 0$, $x/D = 3.0$ (e) $m = 1$, $x/D = 3.0$ (f) $m = 2$, $x/D = 3.0$

(g) $m = 0$, $x/D = 5.0$ (h) $m = 1$, $x/D = 5.0$ (i) $m = 2$, $x/D = 5.0$

(j) $m = 0$, $x/D = 10.0$ (k) $m = 1$, $x/D = 10.0$ (l) $m = 2$, $x/D = 10.0$

Figure 4.14: Comparison of azimuthal mode shapes ($r^{1/2}\psi^1(r,m,f;x)$) for $m = 0$ ((a), (d), (g) and (j)), $m = 1$ ((b), (e), (h) and (k)) and $m = 2$ ((c), (f), (i) and (l)) at different locations in the wake for different PANS simulations.

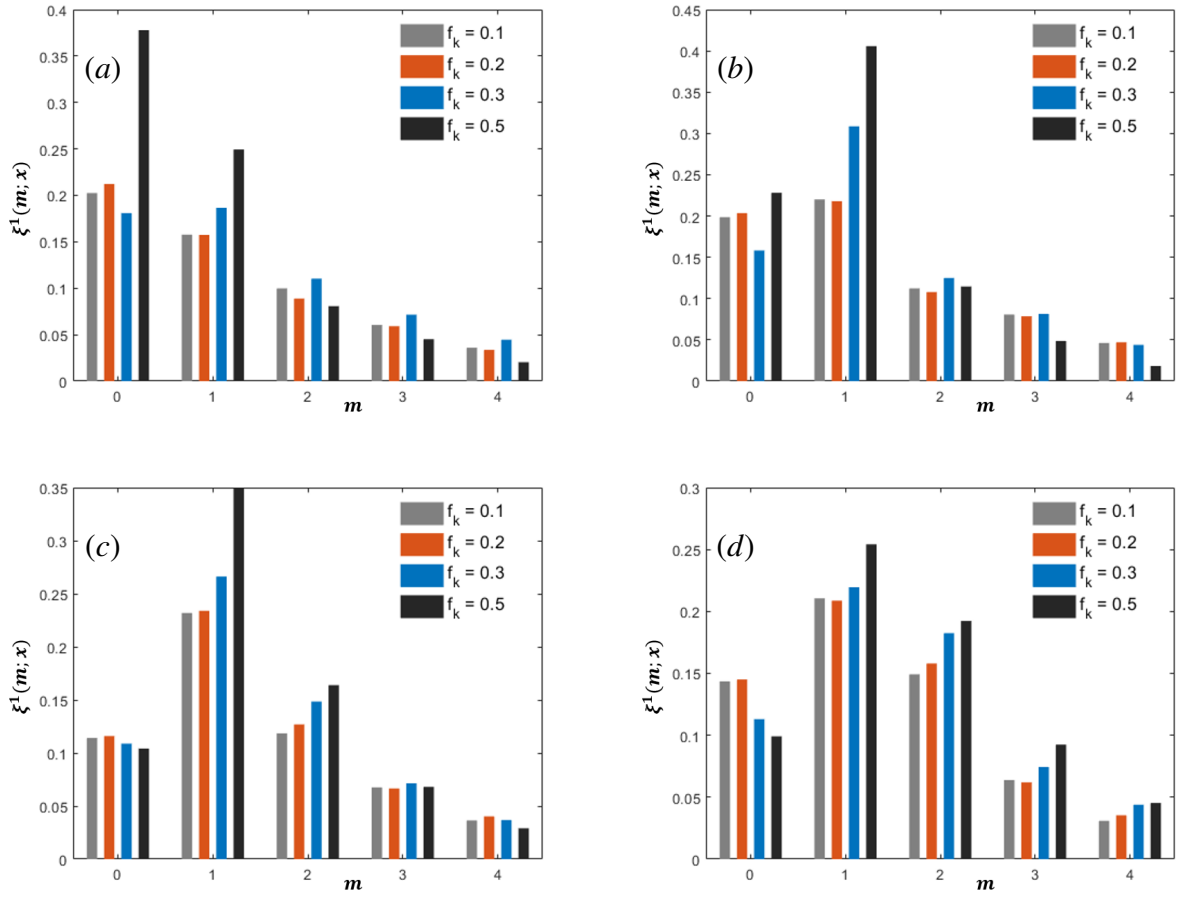

Figure 4.15: Eigenspectrum integrated over frequency ($\xi^1(m;x)$) as a function of azimuthal mode number (m) at different locations: (a) $x/D = 2.0$; (b) $x/D = 3.0$; (c) $x/D = 5.0$ and (d) $x/D = 10.0$ for different physical resolution, f_k.

$x/D = 2.0$, the mode $m = 0$ corresponding to the expansion and contraction of the recirculation bubble is dominant which is consistent with the findings in the axisymmetric wake of a disk [1]. Just beyond the recirculation bubble ($x/D = 3.0$), dominance of $m = 1$ mode is observed as the hairpin vortices start to shed at the end of the recirculation bubble. A significant contribution from $m = 0$ mode is still expected at this location due to its close proximity to the recirculation bubble which is clearly predicted by the high resolution PANS simulations. This is in accordance to the results of Ref. [1] who found the wake of a disk inside the recirculation region dominated by the pumping mode and immediately outside by the helical mode. For downstream locations $x/D > 3.0$, a significant dominance of $m = 1$ mode is expected in the fully-developed wake region. In our analysis, $m = 2$ mode appears to become second-most dominant at $x/D \geq 5.0$. According to the POD analysis of axisymmetric far-wake of a disk, $m = 2$ becomes dominant beyond $x/D \geq 50$ [5]. The contribution of $m = 1$ mode to total energy appears to reduce between $x/D = 5.0$ and $x/D = 10.0$. At $x/D = 10.0$, the coarsening of the grid diffuses the coherent structures leading to lesser energy content in $m = 1$ mode computed by the POD. Based on the analysis, it is evident that the large-scale physics in the near-wake region of a sphere is similar to that of the axisymmetric wake of a disk. The azimuthal modes ($m = 0, 1, 2$) constitute approximately 50% of kinetic energy fluctuations across all the downstream locations in the wake. Moreover, the azimuthal mode ($m = 1$) comprises of approximately 25% of the total energy in the wake after the recirculation region (Fig. 4.15). Although the large-scale dynamics in the flow field are governed by the first three azimuthal modes, higher modes ($m > 2$) contribute significantly to the overall energy content making the reduced order modeling of such flows challenging.

5. CLOSURE MODELING IN THE NEAR-WALL REGION OF STEEP RESOLUTION CHANGE

5.1 Introduction

Steep spatial changes of flow features in the near-wall region renders direct numerical simulations (DNS) of turbulent boundary layers computationally prohibitive at high Reynolds numbers. Even wall-resolved large-eddy simulations (WR-LES) can be very expensive in the Reynolds number range of most boundary layers in practical flows [25]. At the other extreme of the closure modeling spectrum, Reynolds-averaged Navier-Stokes (RANS) models capture the mean-flow and turbulent shear stress profiles accurately [19] at very modest computational cost. The qualified success of RANS models is due to the fact that important closure coefficients are derived based on equilibrium boundary layer (EBL) scaling laws. Thus motivated, many authors in literature have attempted to adapt EBL analysis for obtaining accurate sub-grid wall closures for LES [24, 93, 94]. The resulting methods called wall-modeled LES (WM-LES) have less stringent resolution requirements near the wall and potentially yield reasonable results.

Aside from LES, other computational strategies classified in the general category of scale-resolving simulation (SRS) have emerged over the last two decades. The SRS approaches can be broadly divided into two main groups: zonal and bridging methods. In zonal methods, LES and RANS approaches are used in different parts of the flow field. Zonal SRS (Z-SRS) approach employs RANS at the wall and LES at the interior regions of the flow [25]. The computational domain interfacing between RANS and LES regions is variously called grey-area, hand-shake region, etc. One of the enduring challenges in the Z-SRS approach is to model the grey-area in a physically reasonable manner. Bridging methods [30, 31], on the other hand, use the same model form throughout the computational domain, but the closure coefficients are functions of the implied filter-width to accommodate scale-dependent physics. In principle, at the limit of large filter-width, the bridging-SRS (B-SRS) reverts to RANS and at the limit of small filter-width, B-SRS tends to

DNS. The zonal and bridging SRS approaches have distinctly different near-wall strategies.

As in the case of LES, the B-SRS near-wall computation can employ either the wall-resolved (WR-SRS) or the wall-modeled (WM-SRS) strategies. In WR-SRS, the degree of flow resolution is nearly uniform throughout the flow domain. As in WR-LES, the computational burden of WR-SRS can be significant. For computational expediency, WM-SRS seeks to emulate RANS behavior near the wall and then smoothly switch-over to a scale-resolving computation in the interior of the domain. In both LES and B-SRS, the wall-modeling strategy transfers the burden from large computational effort to higher fidelity closure models in the near wall region.

The objective of this work is to develop a near-wall closure model to account for the effects of steep change in resolution (implied filter-width) to enable accurate and computationally viable WM-SRS. The study involves three distinct steps: (i) closure model development in the switch-over region; (ii) examination of the effect of commutation residue in the switch-over region on the simulated flow physics; and (iii) assessment of the WM-SRS in turbulent channel flow at $Re_\tau = 950,\ 8000$ and wake of a sphere at Reynolds number $Re = 3700$.

In the model development stage, we first identify the form and function of the commutation residue that arises when a spatially varying filter is applied to the Navier-Stokes equations in the switch-over region. Then, the model is derived by utilizing two important physical considerations: (i) the total kinetic energy contained in the resolved and unresolved scales of motion must be invariant of the filter-width and its spatial changes; and (ii) the equilibrium boundary layer (EBL) scalings of filtered flow fields is preserved [41]. The closure models are developed in the context of B-SRS approach called the partially-averaged Navier-Stokes (PANS) method [31].

This study is organized as follows. Development of near-wall physics modeling of the commutation residue is performed in Section. 5.2. Section. 5.3 contains a brief description of the numerical method for implementing the WM-SRS. The results are presented in Section. 5.4.

5.2 Near-wall closure modeling

The near-wall region is characterized by presence of steep variations of flow variables and small turbulence length scales. In wall-resolved PANS (WR-PANS), a constant f_k value is used at

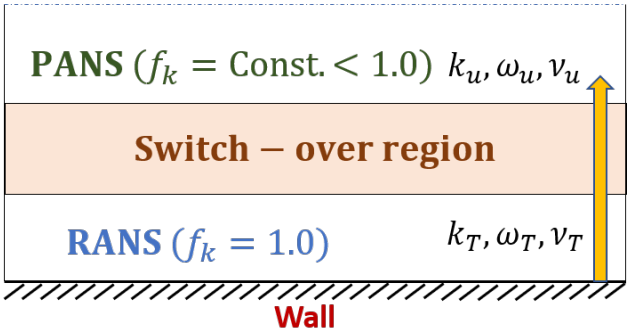

Figure 5.1: RANS-SRS switch-over region near-wall

the wall and interior regions. This entails very small grids near the wall rendering the calculations computationally expensive.

In this study, we propose a wall-modeled PANS (WM-PANS) approach which permits f_k variation from a value of unity near the wall to a smaller value in the outer region. As the near-wall region is completely modeled using the RANS approach ($f_k = 1$), WM-PANS has significantly less stringent grid requirements. Hence, there is a compelling need for developing closure models that enable high-fidelity WM-PANS simulations.

In a typical wall modeled SRS computation, the boundary-layer is divided into three distinct computational regions as shown in Fig. 5.1: Near-wall RANS zone of $f_k = 1$, the grey area (or the switch-over region) and outer SRS region of $f_k < 1$. The simulated flow undergoes a change in description from a steady flow at the wall to highly resolved unsteady flow in the outer region. Closure modeling in the switch-over region represents one of the modern challenges in practical turbulence flow computations.

5.2.1 Closure-modeling in region of varying f_k

As mentioned previously, in the case of varying resolution (varying f_k), the cut-off filter does not commute with spatio-temporal derivatives leading to extra forcing terms in the governing equations. While modeling the commutation terms for temporal variation in f_k is discussed in Ref. [39], here we develop closure models of terms that arise due to a spatio-temporal variation of f_k. As

in Ref. [39], the mathematical framework for these closures comes from 'commutation residue' formulation and the physical principle emerges from the requirement that the total kinetic energy (resolved + unresolved) must be independent of changes in f_k.

We first proceed to formulate the commutation terms in the unresolved scales due to a spatio-temporally varying f_k. The unresolved scales are modeled according to the Boussinesq closure (Eq. 2.10). The unresolved kinetic energy evolution equation is derived as (see Appendix A for details):

$$\frac{\partial k_u}{\partial t} + U_j \frac{\partial k_u}{\partial x_j} = P_u - \beta^* k_u \omega_u + \frac{\partial}{\partial x_j}\left[(\nu + \nu_u/\sigma_{ku})\frac{\partial k_u}{\partial x_j}\right] + P_{Tr} + D_{Tr} \tag{5.1}$$

where P_{Tr} is additional source term arising due to spatio-temporal variation of f_k in the advective term derived as:

$$P_{Tr} \equiv \frac{k_u}{f_k}\left(\frac{\partial f_k}{\partial t} + \overline{U_j}\frac{\partial f_k}{\partial x_j}\right) \tag{5.2}$$

where $\overline{U_j}$ is the mean velocity component. Similarly, the commutation residue due to spatial variations of f_k in the diffusion term is:

$$D_{Tr} \equiv -\frac{k_u}{f_k}\frac{\partial}{\partial x_j}\left(\nu_u^* \frac{\partial f_k}{\partial x_j}\right) - \frac{2\nu_u^*}{f_k}\left(\frac{\partial k_u}{\partial x_j} - \frac{k_u}{f_k}\frac{\partial f_k}{\partial x_j}\right)\frac{\partial f_k}{\partial x_j};\;\; \nu_u^* = \nu + \frac{\nu_u}{\sigma_{ku}} \tag{5.3}$$

The P_{Tr} and D_{Tr} terms account for the additional energy exchange between the resolved and unresolved scales in the switch-over region.

The specific rate of dissipation, ω_u model equation for the case of uniform f_k is given in Ref. [62]. For WM-PANS case, this evolution equation becomes (see Appendix B for full details):

$$\frac{\partial \omega_u}{\partial t} + U_j \frac{\partial \omega_u}{\partial x_j} = \alpha \frac{\omega_u}{k_u} P_u - \beta' \omega_u^2 + \frac{\partial}{\partial x_j}\left[(\nu + \nu_u/\sigma_{\omega u})\frac{\partial \omega_u}{\partial x_j}\right] + D_{Tr\omega} \tag{5.4}$$

where the additional term, $D_{Tr\omega}$ is derived to be:

$$D_{Tr\omega} = -\frac{\omega_u}{k_u}(P_{Tr} + D_{Tr}) \tag{5.5}$$

It is important to note that in regions of negligible f_k variation, the P_{Tr}, D_{Tr} and $D_{Tr\omega}$ terms vanish and the k_u (Eq. 5.1) and ω_u equation (Eq. 5.4) revert to their corresponding uniform-f_k formulations (Eqs. 4.6 and 4.7). We next seek to account for the effect of varying resolution on the resolved flow field.

5.2.2 Effect of varying f_k on resolved flow field

The energy in the resolved flow field ($E_r = \frac{1}{2}U_iU_i$) can be calculated from Eq. 2.6 as:

$$\begin{aligned}\frac{\partial E_r}{\partial t} + U_j\frac{\partial E_r}{\partial x_j} = &-\frac{\partial}{\partial x_j}(\tau(V_i,V_j)U_i) + \frac{\partial U_i}{\partial x_j}\tau(V_i,V_j) \\ &- \frac{\partial P}{\partial x_i}U_i + \nu\frac{\partial^2 E_r}{\partial x_j\partial x_j} - \nu\frac{\partial U_i}{\partial x_j}\frac{\partial U_i}{\partial x_j} - F_iU_i\end{aligned} \tag{5.6}$$

The various terms on the right hand side of equation (5.6) are: turbulent transport of resolved kinetic energy, negative of kinetic energy production, resolved field pressure work, viscous diffusion, dissipation and finally, F_iU_i represents the change in resolved energy due to the commutation residue.

5.2.3 Closure modeling of F_i

Within the Boussinesq framework, varying f_k modifies the eddy viscosity in the system capturing the dynamics introduced by the commutation term. Therefore, the commutation residue term, F_i, in the resolved flow equation (Eq. 2.6) may be modeled as a gradient transport term [39]:

$$F_i = -\frac{\partial}{\partial x_j}(2\nu_{Tr}S_{ij}) \tag{5.7}$$

where ν_{Tr} is termed as the commutation viscosity. Thus, the resolved flow equation, Eq. 2.6 can be written as:

$$\frac{\partial U_i}{\partial t} + U_j\frac{\partial U_i}{\partial x_j} = -\frac{\partial P}{\partial x_i} + \frac{\partial}{\partial x_j}(2(\nu+\nu_u+\nu_{Tr})S_{ij}) \tag{5.8}$$

Total energy conservation dictates that $E_r + k_u$ must remain conserved invariant of the cut-off

(f_k) location and its variations. Using Eq. 2.10 and Eq. 5.7, the evolution equation for the resolved kinetic energy (E_r) from Eq. 5.6 can be written as:

$$\frac{DE_r}{Dt} = -\frac{\partial PU_i}{\partial x_i} + U_i \frac{\partial}{\partial x_j}(2(\nu + \nu_u + \nu_{Tr})S_{ij}) \tag{5.9}$$

The additional viscous term in the resolved flow energy equation due to the commutation residue is decomposed as:

$$U_i \frac{\partial}{\partial x_j}(2\nu_{Tr}S_{ij}) = \frac{\partial}{\partial x_j}(2\nu_{Tr}U_iS_{ij}) - 2\nu_{Tr}S_{ij}S_{ij} \tag{5.10}$$

The transport of resolved kinetic energy by the commutation term is represented by the first term in the RHS of Eq. 5.10. The second term describes the energy exchange between resolved and unresolved scales. Using Eq. 5.1, the following equality must hold in order to conserve the total energy:

$$2\nu_{Tr}S_{ij}S_{ij} = P_{Tr} + D_{Tr} \tag{5.11}$$

which leads to the following expression for commutation viscosity:

$$\nu_{Tr} = \frac{P_{Tr} + D_{Tr}}{2S_{ij}S_{ij}} \tag{5.12}$$

Energy transfer to the resolved scales is associated with a negative ν_{Tr}, while a positive value corresponds to energy transferred from the resolved scales to the unresolved scales.

Eqs. 5.1, 5.4, 5.8 and 5.12, with the commutation terms derived in Eqs. 5.2, 5.3 and 5.5 establish the WM-PANS model. While the formulation presented herein is in the context of PANS, the approach is applicable for all bridging SRS methods.

5.2.4 Spatial variation of physical resolution

In WM-PANS, the characteristics of the switch-over region must be explicitly defined. As in the case of other hybrid SRS schemes (e.g., DES), a blending function between the steady RANS region and the high fidelity region away from the wall must be prescribed. A hyperbolic tangent

function offers a suitable profile for a smooth f_k variation and has been widely used as a blending function in different turbulence models (e.g., DES [25], $k-\omega$ SST [64]). The following function satisfactorily describes the variation of f_k with respect to normalized wall-normal distance, y^+:

$$f_k(y^+) = a_1 - a_2 \tanh\left(\frac{y^+}{\gamma} - c\right);\ a_1 = \frac{1+f_{k(\mathrm{F})}}{2};\ a_2 = \frac{f_{k(\mathrm{F})}-1}{2} \tag{5.13}$$

Here, $f_{k(\mathrm{F})}$ is the value of f_k, i.e., the value of physical resolution in the unsteady freestream region. Parameters a_1 and a_2 are selected to ensure $f_k \approx 1$, i.e., steady RANS region close to the wall. The constants, γ and c, control the width and location of the grey region respectively. Specification of these parameters for the switch-over region depends on available computational resources and the required accuracy of the computed physics. It is evident that as we approach the near-wall region, $f_k(y^+) = 1$ and the Eq. 5.1 and Eq. 5.4 to corresponding RANS equations as the constants computed from Eq. 4.8 and 4.9 revert to the RANS $k-\omega$ values and Eqs. 5.2, 5.3 and 5.5 reduce to zero. The influence of modifying the width (γ) and location (c) of the switch-over region will be analyzed in detail in Section. 5.4.

5.3 Simulation procedure

Unsteady simulations are performed using a finite volume code OpenFOAM [91]. Pressure-velocity coupling is achieved using a Pressure-Implicit with Splitting of Operators (PISO) solver [71]. Second-order accurate schemes are used for spatial and temporal discretization. Two different incompressible flow configurations are used to assess the fidelity of the WM-PANS approach proposed in Section. 5.2: (i) wall-bounded turbulent channel flow, and (ii) flow past a sphere at $Re = 3700$. The domain, boundary conditions and numerical settings for each flow type are presented in the following subsections.

5.3.1 Turbulent channel flow

Periodic boundary conditions are applied in the streamwise as well as spanwise directions. The flow is driven by a constant pressure gradient in the streamwise direction. This pressure gradient is applied as a source term to the streamwise momentum equation. The algebraic equations resulting

Table 5.1: Grid resolution for turbulent channel flow simulations (Δ_x^+ and Δ_z^+ are non-dimensional grid cell sizes in streamwise and spanwise directions, L_x and L_z are domain sizes in streamwise (x) and spanwise (z) directions; N_x, N_y and N_z denote the grid points in x, y and z directions respectively, δ is the channel half-height)

Re_τ	**Model**	N_y	Δ_x^+	Δ_z^+	L_x/δ	L_z/δ	N_x	N_z
950	WM-PANS	101	59.1	29.5	4	2	64	64
8000	WM-PANS	181	497.5	248.4	4	2	64	64

from the discretization schemes are solved using BiConjugate Gradient (BiCG) matrix solver with a Diagonal-based Incomplete LU preconditioner. An iterative tolerance of 10^{-9} is specified for all variables at each time step.

A structured mesh with hexahedral elements is employed in the domain with a uniform grid spacing in both the streamwise and spanwise directions. In the wall-normal direction, the grid cells are clustered near the wall to obtain sufficient resolution in the near-wall region. Table. 5.1 summarizes different test cases with their specific grid resolutions. It is worth noting that significantly coarse grid resolutions are utilized for the WM-PANS simulations compared to the corresponding DNS studies (see, Ref. [4, 70]), particularly at high Reynolds numbers.

5.3.2 Flow past a sphere at $Re = 3700$

Flow past a sphere in the subcritical Reynolds number regime, $Re = 3700$ (based on freestream velocity, V_∞ and the diameter of the sphere, D) is simulated. A cylindrical computational domain is constructed with the sphere located at the origin. The inlet is located at $x/D = -5$, and the outlet is at a distance of $x/D = 30$ from the sphere. The cylindrical domain radially extends to $r/D = 5$.

A uniform velocity in the streamwise direction, $(V_\infty, 0, 0)$ is specified at the inlet and the far-field boundaries with a turbulence intensity of $I = 0.2\%$. Eddy viscosity of $\nu_t/\nu = 10^{-3}$ and non-dimensional rate of dissipation, $\omega^* = 20$ are prescribed at the inflow regions. Zero gradient boundary conditions are specified at the outlet. No slip boundary conditions are specified on the sphere. A geometric agglomerated algebraic multigrid (GAMG) solver is used to solve the alge-

Table 5.2: Grid parameters for flow past a sphere ($Re = 3700$); N_t is the total number of cells in the domain, N_{cs} is total number of cells in the cross-sectional plane (perpendicular to the streamwise axis), $\Delta r^+_{max} = \Delta r_{max}/D$ is max radial displacement of cells in $0.5 \leq r/D \leq 1$, $\Delta t^+ = \Delta t V_\infty/D$ is uniform non-dimensional time step and $\Delta T^+ = \Delta T V_\infty/D$ is the averaging interval for the statistics

Study	Grid Type	$N_t(10^6)$	N_{cs}	Δr^+_{max}	Δt^+	ΔT^+
$G1$	Structured	1.51	8,770	0.041	5.5×10^{-3}	60
$G2$	Structured	4.83	12,320	0.024	5.5×10^{-3}	60
$G3$	Structured	6.09	12,784	0.016	3.7×10^{-3}	200
DNS [2]	Unstructured	9.48	-	-	-	350
DNS [82]	Structured	372.77	80,896	-	-	80

braic equation for pressure and an iterative solver with a Gauss-Seidel smoother is used for all other variables. A tolerance of 10^{-8} is maintained for iterative convergence for all flow variables at every time step.

A multi-block structured grid within the cylindrical domain is constructed using hexahedral elements. An overview of the mesh characteristics is presented in Table. 5.2. A consistent grid configuration for each azimuthal angle (θ) is maintained. A body-fitted radially expanding mesh around the sphere is generated with $\Delta r_{min}/D = 0.003$ (normalized radial displacement of the first cell center from the sphere surface) for all the meshes presented in Table. 5.2.

For both flow types, CFL is maintained at a value of less than unity to ensure numerical stability. The various quantities specified at the inlet are: (i) turbulent kinetic energy, $k_u = f_{k(F)}k$, (ii) specific dissipation rate, $\omega_u = (1/f_{k(F)})\omega$, and (iii) unresolved eddy viscosity, $\nu_u = (f^2_{k(F)})\nu_t$. In the above expressions, $f_{k(F)}$ is the freestream value of f_k in the domain. The specific dissipation rate at the wall is calculated as $\omega = 80\nu\Delta r^{-2}_{min}$ [19].

5.4 Results

This section examines the ability of WM-PANS to capture flow statistics, integral quantities and turbulence spectral characteristics in comparison with established numerical studies. Two benchmark flow types are evaluated: (i) Turbulent channel flow at very high Reynolds numbers

(up to $Re_\tau = 8000$), and (ii) Flow past an axisymmetric body of sphere in the subcritical Reynolds number regime.

5.4.1 Turbulent channel flow

5.4.1.1 Analysis of flow behavior in the switch-over region

According to the results of Ref. [40], a 'twitch' in the velocity and stress profiles is observed coinciding with the switch-over region. Here, we investigate the underlying reason using the simulations of $Re_\tau = 8000$ with different f_k profiles as presented in the Fig. 5.2(a). These different cases represent switch occurring progressively farther from the wall (c) and over a wider (γ) grey zone. Fig. 5.2(b) presents the mean streamwise velocity profiles obtained for different f_k variations for $Re_\tau = 8000$. All the simulations are able to capture the log-law behaviour reasonably well. A slight disagreement in the switch-over region is noticeable. An explanation of this disagreement follows.

Fig. 5.3 illustrates the streamwise Reynolds stress profiles for $Re_\tau = 8000$ for different cases outlined in Fig. 5.2(a). From the DNS results, it is evident that the peak of the streamwise stresses occurs in the buffer region, i.e., $y^+ \approx 15$. To examine the location of WM-PANS peak, we use the paradigm that PANS is DNS of a variable viscosity fluid [38]. Accordingly, we define the effective y^+ as follows:

$$y^+_{eff}\,(\text{PANS}) = \frac{u_\tau y}{(\nu + \nu_u + \nu_{Tr})} \tag{5.14}$$

It is immediately evident that the peak value in all cases occurs at $y^+_{eff} \approx 15$. The computational viscous sublayer and computational buffer layer in the WM-PANS simulations extend further into the outer region of the channel according the prescribed f_k variation. As soon as the unsteady PANS region is reached, the instabilities manifest and the peak values in the streamwise turbulence stresses are observed at the location of $y^+_{eff} \approx 15$. As the distance of the switch-over location (c) from the wall is increased (*Case A*3), the width of the viscous sublayer and early buffer region increases as well. In DNS, the flow transitions naturally from buffer layer to log-layer behavior. In WM-PANS however, this transition is forced to occur rapidly and at a location further away

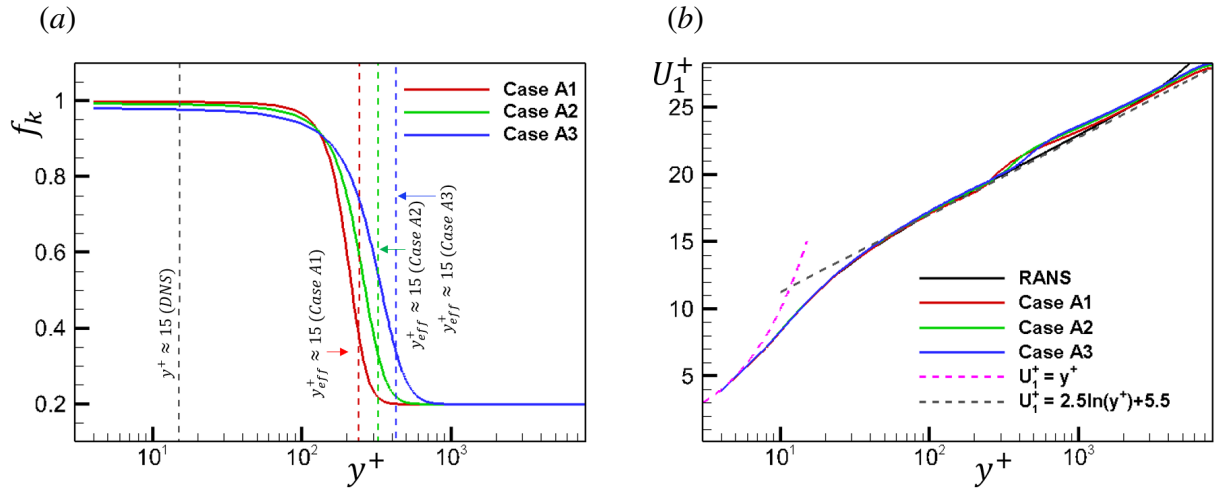

Figure 5.2: WM-PANS simulation for $Re_\tau = 8000$: (a) Prescribed f_k variations and (b) profiles of mean streamwise velocity in wall-normal direction.

from the wall dictated by the f_k prescription. This causes a twitch in the flow statistics in the switch-over region. The model recovers to the correct log-law behavior quickly. We believe that the twitch cannot be completely avoided in any switch-over zone. Its effect can be minimized by having a more gradual change in f_k but this affects the size of the grey zone.

Fig. 5.4 illustrates the spanwise vorticity contours in the $x-y$ plane for *Case A*1 and *Case A*3. The contours clearly indicate that the steady RANS region contains negligible vortical fluctuations. However, as the f_k is spatially reduced along the wall-normal direction (y^+), the instabilities are released leading to formation of multi-scale turbulence structures in the interior of the channel. It is evident that the resolution of structures is directly dependent on the switch-over location. Therefore, this switch-over region can be characterized as a computational non-turbulent/turbulent (NT/T) interface [95] where a sharp increase in fluctuating vorticity is seen (Fig. 5.4) as the f_k value is reduced, i.e., resolution increases. When the computational buffer-layer is narrow (small γ), the unsteady structures are exclusively in the computational log-layer region. When this layer is wider (larger γ), some of the vortical structures penetrate into the switch-over region. This leads to a decrease in the twitch observed in the flow statistics (*Case A*3).

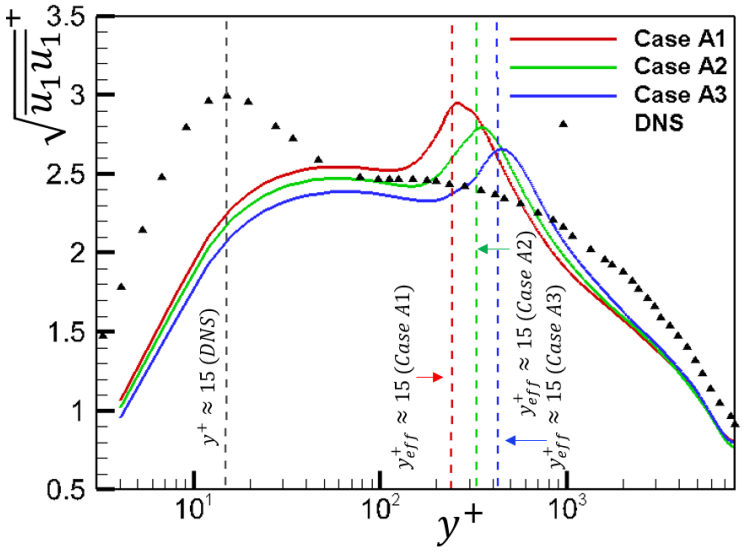

Figure 5.3: WM-PANS simulation for $Re_\tau = 8000$: Profiles of streamwise Reynolds stresses. DNS result of Ref. [4] is used for comparison. The results clearly demonstrate a 'twitch' in the computational buffer layer.

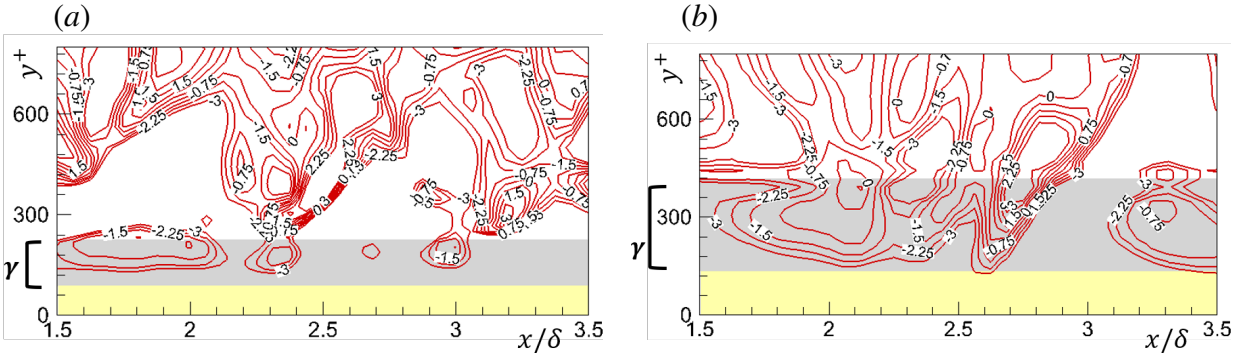

Figure 5.4: Spanwise vorticity ($\omega_z \delta / U_c$) contours (red) in x-y plane for: (a) *Case A*1 and (b) *Case A*3 for $Re_\tau = 8000$. The yellow shaded region is the steady RANS region, white region is the unsteady PANS region and the switch-over region is denoted by the grey shaded area with width (γ); U_c is the velocity in center of the channel.

Table 5.3: Variation of switch-over region: y_s^+ is the center of the switch-over region

Study	c	γ	y_s^+
Case B1	1.8	23.75	50.2
Case B2	5.0	23.75	149.2

5.4.1.2 Flow structures for varying switch-over region location

In order to examine the unsteadiness captured in the WM-PANS, two simulations are performed with different spatial f_k variations near the wall at $Re_\tau = 950$. The details are specified in Table. 5.3.

For Case B1, the resolution control parameter (f_k) transitions in the range of $20 < y^+ < 100$, whereas for the second case the numerical transition from steady to unsteady part occurs within $100 < y^+ < 250$. In Fig. 5.5, iso-surfaces of the second invariant of the velocity gradient tensor, Q are presented for the two cases. As is evident from the figure, a considerable amount of unsteadiness is resolved using the f_k distribution for Case B1 where the switch-over region occurs in the buffer layer. The spectral behavior of streamwise velocity fluctuations (u_1) at $y^+ = 25$ and $y^+ = 500$ are presented in Fig. 5.6. The absence of high frequency fluctuations for Case B2 clearly illustrates its inability to resolve small temporal scales in the buffer region and early log-layer region near-wall. However, in the PANS region beyond the switch-over location, i.e., $y^+ = 500$ (Fig. 5.6 (b)), the temporal spectra reveal nearly identical unsteadiness for both cases.

Therefore, it is evident that even though structures near-wall are not captured in Case B2, the WM-PANS recovers sufficient unsteadiness away from the wall irrespective of the switch-over region location. However, the switch-over region must ensure that at least part of the region of instability is resolved using high resolution PANS for the underlying instabilities to manifest. This serves as the foundation for the analysis of large-scale structures in Chapter. 6.

5.4.2 Flow past a sphere at $Re = 3700$

Now, we evaluate the ability of WM-PANS approach to capture the flow past a sphere at $Re = 3700$. At this Reynolds number, the boundary layer separation is laminar and the transition to

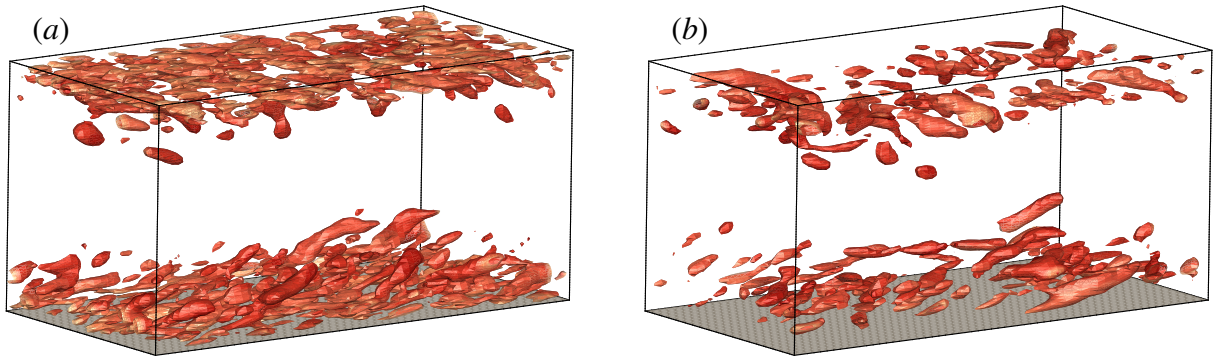

Figure 5.5: Q iso-surfaces (colored with streamwise velocity) (a) Case B1 and (b) Case B2

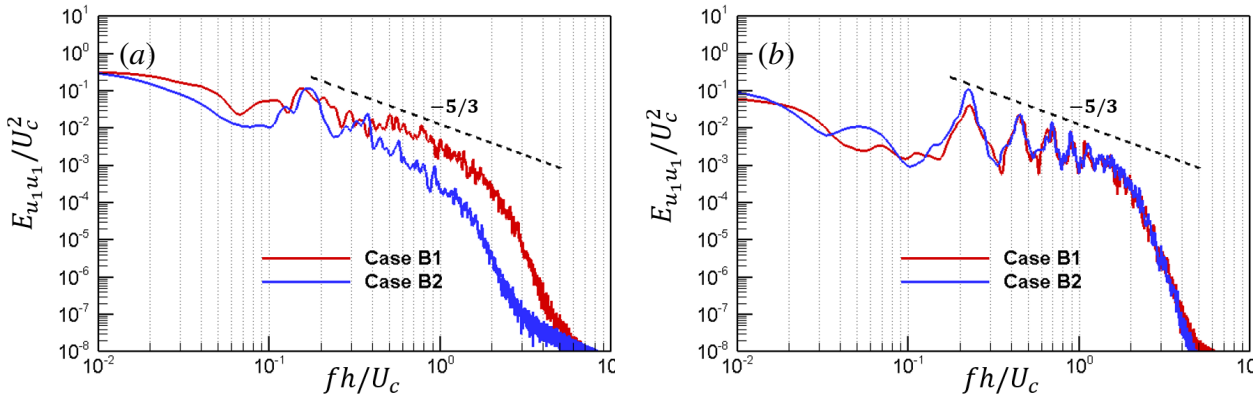

Figure 5.6: Temporal spectra of streamwise velocity fluctuations for Case B1 and Case B2 at (a) $y^+ = 25$ and (b) $y^+ = 500$

Table 5.4: Integral quantities; Time-averaged drag coefficient $\overline{C_d}$, root-mean-square lift coefficient $C_l(RMS)$, Strouhal number S_t, recirculation length L_R, time-averaged base pressure coefficient $\overline{C_{pb}}$ and separation angle $\phi_s(^o)$

Study	$\overline{C_d}$	$C_l(RMS)$	S_t	L_R	$\overline{C_{pb}}$	$\phi_s(^o)$
WR-PANS ($G1$)	0.422	0.0115	0.221	2.03	-0.221	90.17
WR-PANS ($G2$)	0.405	0.0115	0.201	2.15	-0.221	89.98
WR-PANS ($G3$)	0.396	0.0082	0.216	2.24	-0.221	89.82
WM-PANS ($G1$)	0.395	0.0079	0.214	2.27	-0.220	89.83
WM-PANS ($G2$)	0.396	0.0070	0.217	2.27	-0.220	89.79
DNS [2]	0.394	–	0.215	2.28	-0.207	89.4
LES [78]	0.355	–	0.21	2.622	-0.194	90

turbulence occurs in the separated axisymmetric shear layer. According to the results of Ref. [61], flow physics in the wake of the sphere in the subcritical regime was accurately captured with WR-PANS at $f_k \leq 0.3$. Here we perform WM-PANS simulation of the same flow with significantly lesser number of grid points as outlined in Table 5.2. We ensure that the underlying instabilities are resolved by maintaining $f_{k(F)} = 0.3$ in the wake region.

The spatial variation of physical resolution ($f_k(r^+)$) is presented in Fig. 5.7(a). This f_k variation ensures that the location of transition to turbulence in wake is sufficiently removed from the switch-over region so that the small-scale instabilities in the wake manifest completely.

The integral quantities are compared with the established numerical studies in Table 5.4. It is evident that WM-PANS compares extremely well with the DNS data even at extremely coarse mesh resolution (see, Table 5.2). WR-PANS results at the same numerical resolutions are also presented for comparison. On coarse grid resolutions ($G1, G2$), the WR-PANS simulations overpredict the drag coefficient ($\overline{C_d}$) and underpredict the recirculation region (L_R). This is due to the fact that the grid resolution is not adequate for the specified uniform-$f_k = 0.3$ near-wall for WR-PANS.

Now, we evaluate the efficacy of WM-PANS approach in capturing first and second order statistics in wake of the sphere. Fig. 5.7(b) presents the plot of mean streamwise velocity ($\overline{U_x}$) along

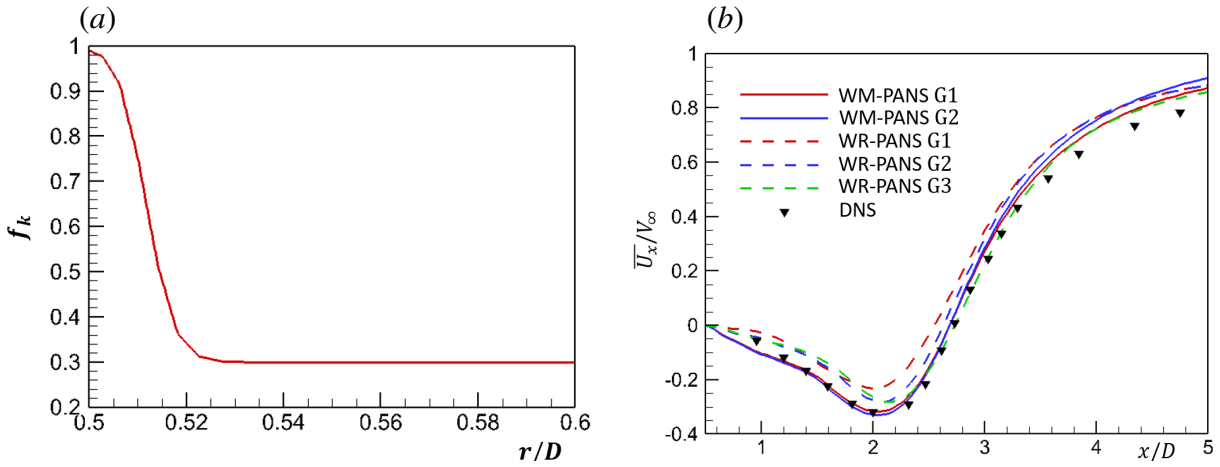

Figure 5.7: (a) Variation of physical resolution, f_k along non-dimensionalized wall-normal direction and (b) mean streamwise velocity profile in the centerline for different simulations compared to DNS of Ref. [2].

the wake centerline for the different simulations performed in this study. The WM-PANS results are in excellent agreement with the DNS results. Again, on coarse grids, the WR-PANS simulations incur a significant error (23.8% for $G1$) in estimation of the minimum $\overline{U_x}$ at $x/D = 2.13$.

First- and second-order statistics at different downstream locations in the wake are presented in Fig. 5.8. The location $x/D = 1.6$ is inside the recirculation region adjacent to the sphere. At this location the small-scales are formed which eventually lead toward breakdown to turbulence at $x/D \approx 2.3$. The $'U'$ shape of the mean streamwise profile is captured reasonably well by all simulations (Fig. 5.8(a)). Major differences in the estimated values of $\overline{U_r}$ is observed in WR-PANS simulations compared to the DNS study. It is evident that the given numerical resolution is insufficient for WR-PANS simulations to accurately estimate the behavior of small scales inside the recirculation region. WM-PANS simulations capture the behavior with reasonable accuracy. The coarse grid (WM-PANS $G1$), however, shows deviations from the DNS data for the total turbulent kinetic energy ($\overline{k_T}$) as shown in Fig. 5.8 (e). The second-order statistics have a stronger dependence on the numerical resolution as the small scale fluctuations must be sufficiently resolved by the given grid. Figs. 5.8 (b), (d), (f) illustrate first- and second-order statistics at the downstream location of $x/D = 3.0$, just the outside the recirculation region. At this location, the breakdown to

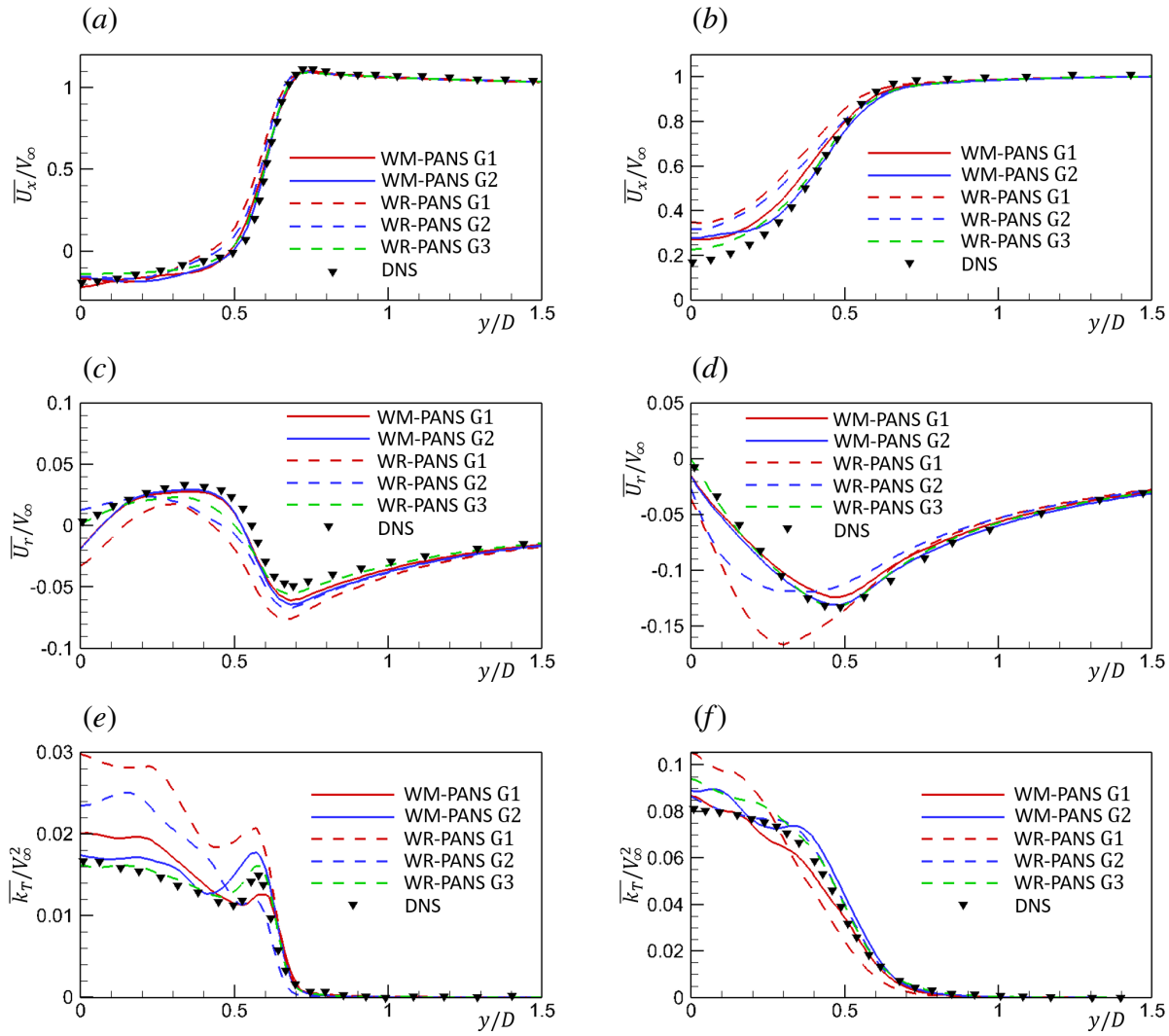

Figure 5.8: Time-averaged streamwise velocity ($\overline{U_x}$), radial velocity ($\overline{U_r}$) and total turbulent kinetic energy, k_T (resolved + modeled (k_u)) profiles in $z = 0$ plane for $x/D = 1.6$ $((a),(c),(e))$ and $x/D = 3.0$ $((b),(d),(f))$. Results are compared to DNS [2].

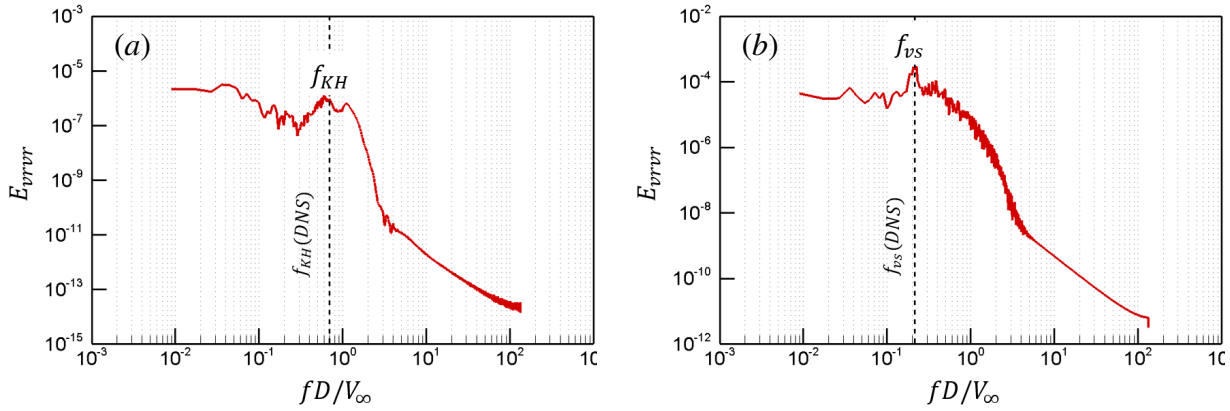

Figure 5.9: Radial velocity spectra at different probe locations in the wake; (a) Probe 1: $x/D = 1.0$, $r/D = 0.6$ and (b) Probe 2: $x/D = 3.0$, $r/D = 0.6$ for WM-PANS $G1$. The spectra are averaged from data at eight equally-spaced locations in azimuthal direction.

turbulence is complete and the small-scales coalesce into large scales which are shed periodically into the helical wake. Figs. 5.8 (d), (f) show significant deviations for the WR-PANS $G1$ simulation in estimation of flow statistics compared to DNS.

Fig. 5.9 presents the radial velocity (U_r) spectra at different probe locations in the wake for WM-PANS $G1$ simulation. Two key underlying instabilities: (i) small-scale Kelvin-Helmholtz (f_{KH}), and (ii) large-scale vortex-shedding (f_{vs}) instabilities are present in the wake of the sphere in the subcritical regime [61]. WM-PANS captures the key instabilities in the wake reasonably well at the coarse grid resolution ($G1$). The intermittent K-H instability along the periphery of the axisymmetric shear layer (i.e., along the inflection line) is captured as a broadband peak in Fig. 5.9 (a). It is important to note that the prescribed f_k variation (Fig. 5.7 (a)) ensures that the regions of development of key instabilities in the flow completely lie in the unsteady PANS region.

Fig. 5.10 presents the iso-surfaces of second invariant of velocity gradient tensor, Q colored with the streamwise velocity (U_x). It is immediately evident that WM-PANS on the coarse mesh ($G1$) is able to qualitatively capture large scales in the wake similar to the WR-PANS on the finest mesh ($G3$). Naturally, resolution of smaller spatial scales require high grid resolution in the wake. A quantitative analysis of the coherent structures resolved by the WM-PANS approach in the wake of a sphere in supercritical Reynolds number regime is present in Chapter. 6.

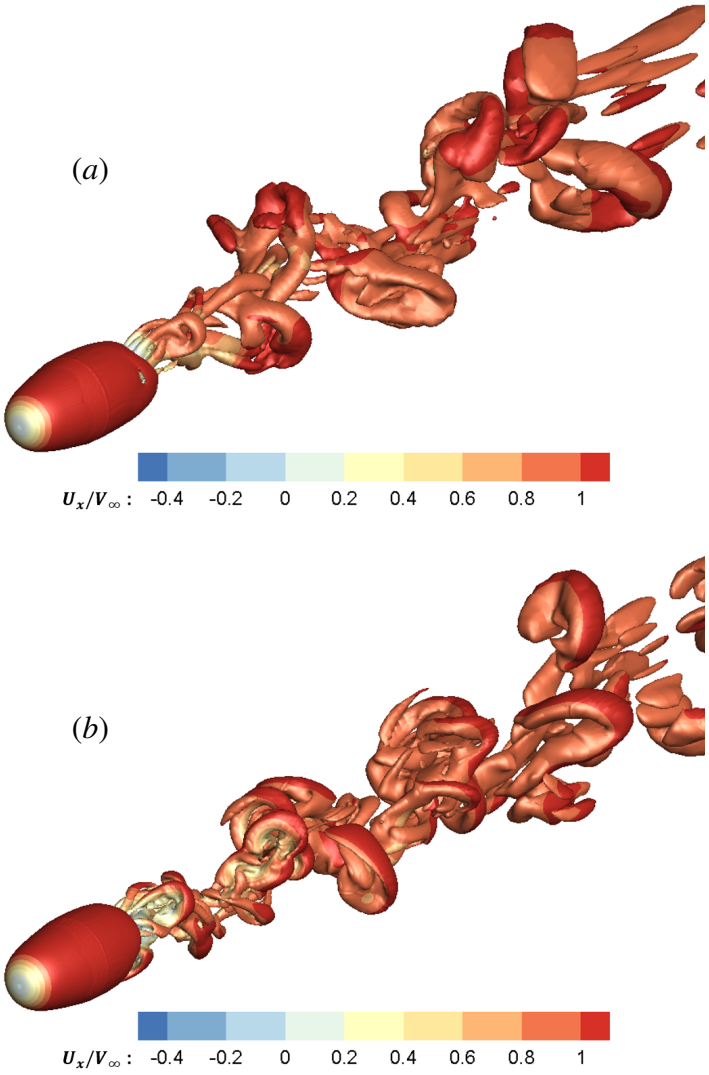

Figure 5.10: Instantaneous Q-factor iso-surfaces colored with resolved streamwise velocity U_x for (a) WM-PANS $G1$ and (b) WR-PANS $G3$

6. WALL-MODELED PARTIALLY-AVERAGED NAVIER-STOKES SIMULATIONS OF TURBULENT WAKE OF A SPHERE AT $Re = 10^6$

6.1 Introduction

Flow past a smooth sphere remains one of the most challenging problems for many turbulence models. This simple geometry exhibits variety of complex flow phenomenon including transition to turbulence, smooth-surface separation and a complex three-dimensional wake. In the subcritical Reynolds number regime, $Re < 3.7 \times 10^5$, the boundary layer remains essentially laminar and transition to turbulence occurs in the separated shear layers. As the Reynolds number increases, the location of transition to turbulence moves toward the sphere and at the critical Reynolds number $Re_{cr} = 3.7 \times 10^5$ the transition occurs in the boundary layers exhibiting the well-known 'drag-crisis'. Beyond Re_{cr}, i.e., in the supercritical Reynolds number regime, the boundary layer is turbulent prior to separation and vortices are shed from the sphere into a fully turbulent wake.

Although, numerous numerical and experimental investigations of flow past a sphere in the subcritical Reynolds number regimes are present in the literature [2, 78, 96], the studies in the supercritical regime are relatively scarce. The earliest experimental investigation of flow past a sphere at high Reynolds numbers is presented in Ref. [6]. In this study, a high-pressure wind tunnel is used to measure integral quantities (total drag, skin friction and static pressure) for the Reynolds number range $5 \times 10^4 \leq Re \leq 6 \times 10^6$. Ref. [85] visualized the turbulent wake of a sphere in a wind tunnel for the Reynolds number in the range 10^4 to 10^6. The results show a pair of streamwise vortices a short distance away from streamwise axis. The results also indicated a side force on the sphere between $3.8 \times 10^5 < Re < 10^6$. Detached eddy simulations (DES) of Ref. [5] also exhibit a tilting of the wake and array of hairpin vortices that are shed at the same azimuthal angle over long periods of time.

It is widely acknowledged that Reynolds-averaged Navier-Stokes (RANS) models predict the turbulent boundary layer growth and certain aspects of separation well [20]. They, however, fail

to estimate the large separation regions and unsteadiness in the flow and therefore their merit in complex flows of engineering interest is limited. Large-Eddy Simulations (LES) on the other hand resolve a large range of scales in the flow, but, are computationally challenging for complex engineering flows. In wall-resolved LES, the cost to resolve the small scale eddies in the attached boundary layers is $\Delta_x\Delta_y\Delta_z \propto Re_L^{1.8}$ [24] which is excessive for high Reynolds number flows of $O(10^6)$. Therefore, there has been a considerable interest in turbulence modeling practices which are computationally economical and resolve important flow physics.

Scale-Resolving Simulations (SRS) offer 'accuracy-on-demand' wherein only the energy containing scales are resolved and dynamically passive scales are modeled. Unlike LES, the cut-off between the resolved and unresolved scales can be positioned in the inertial range thereby decreasing the cost of computations significantly. Partially-averaged Navier-Stokes (PANS) method is bridging-SRS approach that can provide accuracy ranging from RANS to DNS with proportional computational effort [31, 34]. PANS methods utilize an implicit filtering technique wherein the closure coefficients in RANS turbulence models are modified to resolve the requisite range of scales in the flow. PANS turbulence closures have been successfully applied to a wide range of complex industry relevant flows ([63, 56]) and have been shown to satisfy turbulence scaling laws [38].

The wall-resolved PANS (WR-PANS) models prescribe uniform filter parameters throughout the domain which can translate to high computational cost in the near-wall region at high Reynolds number. Therefore, similar to the modeling rationale in hybrid turbulence closure (e.g., DES), a variable-resolution wall-modeled PANS (WM-PANS) strategy can be adopted. This technique developed in Ref. [97] employs a steady RANS in the near-wall region and models the outer region as high-resolution PANS. Therefore, the computational cost associated with resolving small scales in the near-wall region is greatly reduced and high-resolution is only applied to the region of interest away from the wall. The WM-PANS strategy has been applied to high Reynolds number channel flow, a low Reynolds number flow over smooth hump and flow past a sphere in subcritical regime with reasonable success [40, 97].

The WM-PANS approach is ideal for turbulence closure in the supercritical Reynolds number regime at lower computational effort. We propose the following objectives of the study: (i) evaluate the WM-PANS approach in the fully turbulent wake of a sphere at $Re = 1.14 \times 10^6$ and (ii) analyze the organization of large scale structures in this Reynolds number regime. This study is organized as follows: In Section. 6.2, we present the WM-PANS equations. Section. 6.3 delineates the numerical setup employed in this study. In Sec. 6.4, the results obtained from the WM-PANS simulations are presented. We also characterize the differences in the wake structures observed in subcritical and supercritical Reynolds number regimes.

6.2 Wall-Modeled PANS (WM-PANS) equations

The wall-modeled PANS (WM-PANS) equations used in this study are presented in Chapters. 2 and 5. High Reynolds numbers and steep f_k variation can lead to very high values of the $P_{Tr} + D_{Tr}$ term which can make the numerical solution unstable. Therefore, we propose two limiters on ν_{Tr} to ensure physical consistency:

$$\nu_{Tr} < \frac{\nu_u}{f_k^2} \text{ (Limiter 1)}; \quad \nu_u + \nu_{Tr} + \nu \geq \nu \text{ (Limiter 2)}; \tag{6.1}$$

Limiter 1 ensures that the commutation viscosity is always smaller than the total (or RANS) eddy viscosity. Limiter 2 ensures that the total viscosity in the system is always above the kinematic viscosity of the fluid. This situation arises when the negative value of ν_{Tr} is greater than $\nu_u + \nu$ due to very steep spatial variation of f_k in the domain. The above limiters ensure robustness of the turbulence modeling scheme.

6.3 Numerical setup

Flow around a sphere at the Reynolds number, $Re = 1.14 \times 10^6$ based on the freestream velocity (V_∞), diameter (D) and the kinematic viscosity (ν) is simulated. Experimental results by Ref. [6] and numerical results by Ref. [5] are used to compare the integral flow quantities.

6.3.1 Domain and boundary conditions

The sphere is enclosed in a cylindrical domain with inlet located at $x/D = -5$ and the outlet extends to $x/D = 30$ with the sphere located at the origin. The domain radially expands to $r/D = 5.0$.

A constant inflow velocity, $(V_\infty, 0, 0)$ is specified at the inlet and the far field boundaries and a non-reflecting advective boundary condition is applied at the outlet. No-slip and impermeability boundary conditions are prescribed on the sphere wall. A zero gradient boundary condition for pressure is specified at all the boundaries. In the present study, a fully turbulent boundary layer is simulated and therefore a turbulence intensity of $I = 1\%$ is maintained at the inlet. The turbulent kinetic energy at the inlet is determined based on: $k = 1.5(V_\infty I)^2$. A non-dimensional eddy viscosity ($\nu_t/\nu = 1.0$) is prescribed at the inlet. This eddy viscosity value ensures that the flow field is turbulent prior to entering the boundary layers. The unresolved specific dissipation rate (ω) at the inlet and the far-field boundaries is then determined using $\omega = k/\nu_t$. The specific dissipation rate at the wall is determined by $\omega = 80\nu\Delta r_{min}^{-2}$ [19], where Δr_{min} is the distance of cell center adjacent to the sphere from the sphere's surface. The inlet and far field values are multiplied with $f_{k(F)}$ to obtain their corresponding PANS counterpart: $k_u = f_{k(F)}k$, $\omega_u = (1/f_{k(F)})\omega$ and $\nu_u = (f_{k(F)}^2)\nu_t$ where $f_{k(F)}$ is the value of f_k in the freestream region.

6.3.2 Solver settings

An open source finite-volume code, OpenFOAM [91] is used to perform unsteady transient simulations for incompressible flow. The pressure-velocity coupling is achieved using a pressure-implicit splitting of operators (PISO) algorithm [71] with two inner corrector loops. A geometric agglomerated algebraic multigrid (GAMG) solver is used to solve the algebraic equations for pressure with iterative tolerance of 10^{-8}. For other flow variables (U, k, ω), an iterative solver with a Gauss-Seidel smoother is applied with a tolerance of 10^{-7} every time step. An implicit backward scheme is utilized for time integration. Second-order schemes are used for all spatial discretizations.

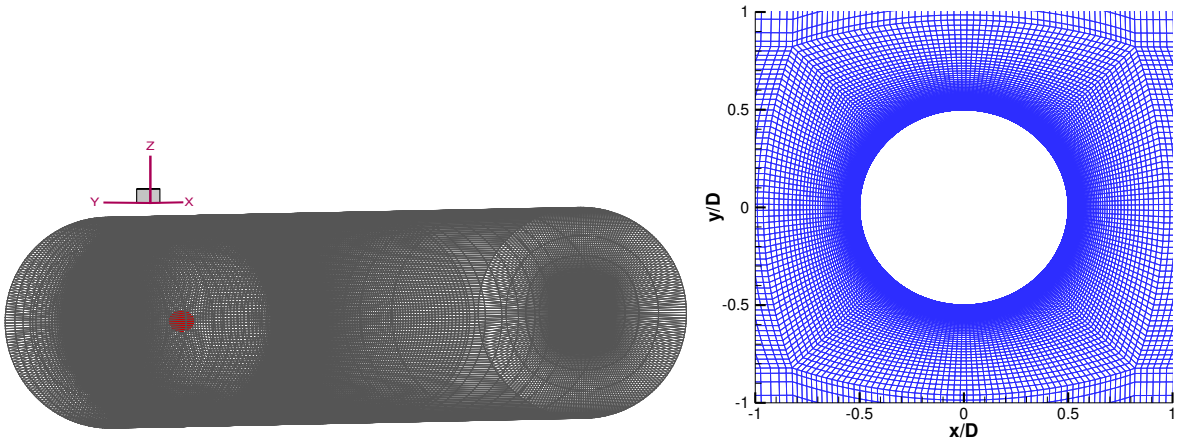

Figure 6.1: Grid configuration of the domain (left) and grid resolution near the sphere in the cross-sectional plane normal to streamwise axis (right).

6.3.3 Mesh characteristics and convergence study

A multiblock structured grid using hexahedral elements is constructed using ANSYS ICEM. The sphere is enclosed in a body-fitted radially expanding mesh from $0.5 \leq r/D \leq 1.0$ with minimum $\Delta r^+ = u_\tau \Delta r_{wall}/\nu \approx 1$ near the sphere surface and the friction velocity is estimated as $u_\tau = 0.04 V_\infty$ similar to the DES computations [5]. Fig. 6.1(a) illustrates the grid configuration in the entire domain and the mesh characteristics are presented in Table. 6.1. The near wake region ($1.0 \leq x/D \leq 5.0$) has a $\Delta r_{min}/D = 0.03$ and $\Delta r_{max}/D = 0.12$ with approximately 100 grid points in the streamwise direction for the G_3 mesh. A consistent grid configuration is maintained in the azimuthal (θ) direction. The grid configuration near the sphere is shown in Fig. 6.1(b). The grid is clustered near the sphere with approximately 30 points in the turbulent boundary layer and an exponential stretching is imposed.

A grid convergence study is performed for the $f_{k(F)} = 0.5$ case and the mean pressure coefficient ($\overline{C_p}$) around the cylinder (azimuthally averaged) and the mean streamwise velocity ($\overline{U_x}$) profiles are presented in Fig. 6.2. The coarse mesh G_1 overpredicts the back pressure coefficient ($\overline{C_{pb}}$) and predicts a smaller recirculation region compared to the finer meshes, G_2 and G_3. In Fig. 6.2(b), $f_{k(F)} = 1.00$ (RANS) case is also presented for comparison. Based on the analysis,

Table 6.1: Grid parameters; N_t is the total number of cells in the domain, N_{cs} is total number of cells in the cross sectional plane (perpendicular to the streamwise axis), $\Delta r_{max}/D$ is max radial displacement of cells in $0.5 \leq r/D \leq 1$, $\Delta t^+ = \Delta t V_\infty/D$ is uniform non-dimensional time step and $\Delta T^+ = \Delta T V_\infty/D$ is the averaging interval for the statistics

Study	$N_t(10^6)$	N_{cs}	$\Delta r_{max}/D$	Δt^+	ΔT^+
RANS ($f_{k(F)} = 1.00$)	3.52	10,981	0.028	2.82×10^{-3}	28.2
PANS ($f_{k(F)} = 0.70$)	3.52	10,981	0.028	2.82×10^{-3}	28.2
PANS ($f_{k(F)} = 0.50$)					
G_1	1.71	8,770	0.058	2.82×10^{-3}	21.15
G_2	2.45	9,352	0.045	1.41×10^{-3}	21.15
G_3	3.52	10,981	0.028	1.41×10^{-3}	28.2
PANS ($f_{k(F)} = 0.30$)	5.40	12,320	0.018	9.12×10^{-4}	21.15
DES [5]	1.16	-	-	0.02	30

G_3 mesh configuration is used to analyze the integral quantities, statistics and flow structures for $f_{k(F)} = 0.5$ case.

In the next section, we investigate the integral quantities, flow statistics in the turbulent wake and flow structures for different physical resolution (f_k) variations. It must be emphasized that f_k represents prescribed physical resolution which is the implied cut-off scale. The numerical resolution on the other hand is indicated by grid size.

6.4 Results

The WM-PANS simulation results are presented in this section. The physical resolution is varied from $f_k = 1.00$ (RANS) to a smaller value $f_{k(F)}$ in the freestream region. The location of the switch-over region is clearly dictated by the regions of instability in the fluid flow. According to Ref. [97], a good agreement between numerical studies and the WM-PANS is achieved even for the switch-over region located at $y^+ = 300$ for high Reynolds number turbulent channel flow. Therefore, in the present study, f_k is varied gradually with the switch-over location ranging from $r^+ = 200 - 450$ for different $f_{k(F)}$ cases. Largest width of the switch-over region is prescribed

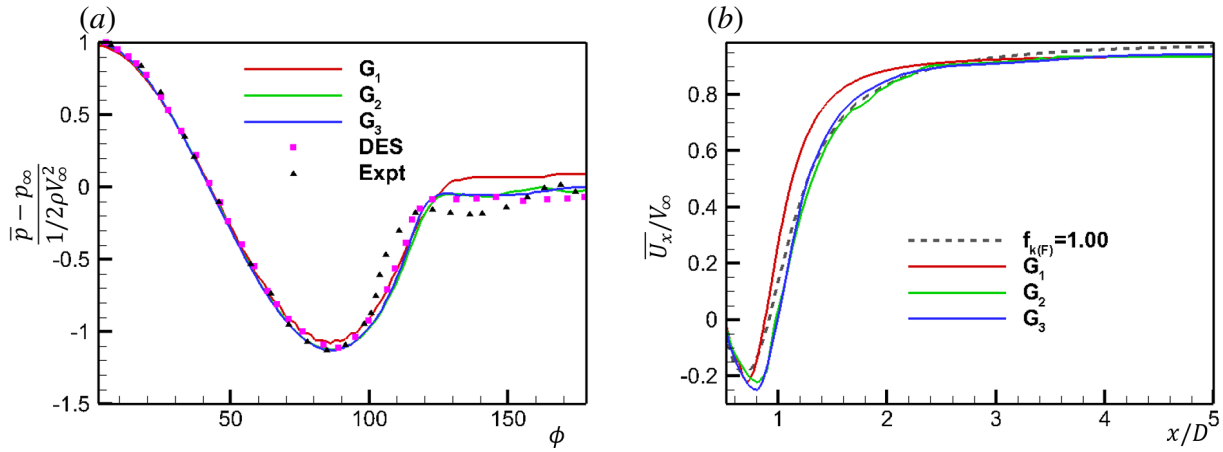

Figure 6.2: Grid convergence study: (a) mean pressure coefficient around the sphere and (b) time-averaged streamwise velocity profile in the centerline for $f_{k(F)} = 0.5$. DES of Ref. [5] and experiments of Ref. [6] are used for comparison.

Table 6.2: Variation of switch-over region

Study	c	γ	r_s^+
PANS ($f_{k(F)} = 0.70$)	5	57	200.8
PANS ($f_{k(F)} = 0.50$)			
Case 1	3.5	68.4	178.6
Case 2	4.28	79.8	364.8
PANS ($f_{k(F)} = 0.30$)	3.8	114	438.1

for $f_{k(F)} = 0.30$ case to avoid steep gradients in the governing equations. Table. 6.2 presents the parameters for spatial variation of f_k.

6.4.1 Variation of switch-over region and model consistency

The sensitivity of the WM-PANS in the switch-over region is investigated for two different f_k variations prescribed in Table. 6.2. The switch-over region varies from $110 < r^+ < 200$ in Case 1 and from $150 < r^+ < 400$ for Case 2. The results from both the f_k variations are presented in Fig. 6.3. The prescription of f_k must ensure that the key underlying instabilities in the flow

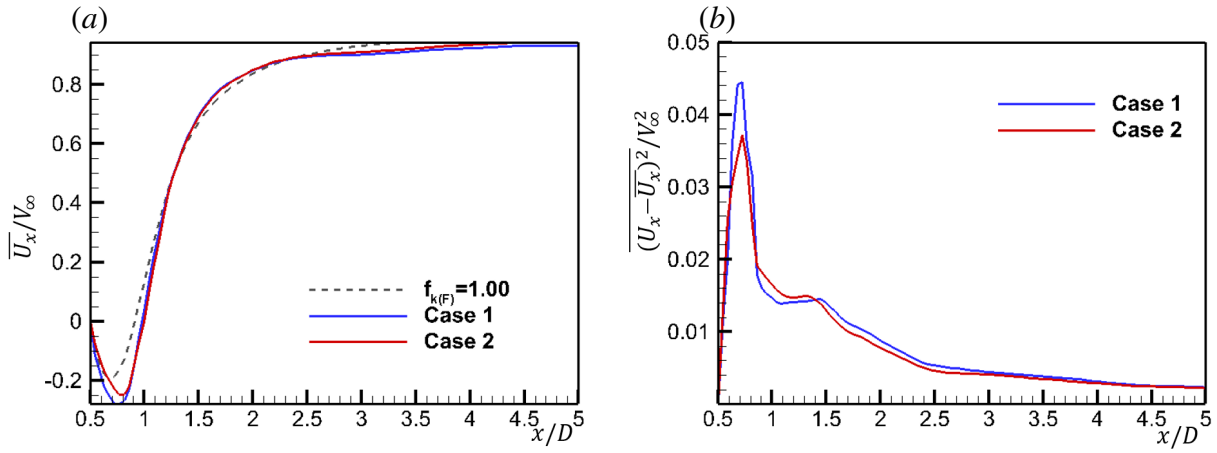

Figure 6.3: (a) Mean streamwise velocity profile and (b) mean resolved streamwise turbulent stress profile in the centerline for different f_k variations

field are adequately resolved [97]. Therefore, these f_k prescriptions ensure that model switches to high-resolution PANS in the log-layer region. Fig. 6.3(a) presents the mean streamwise velocity profiles ($\overline{U_x}$) in the centerline for the two cases. Beyond the recirculation region ($x/D \geq 1$) both the simulations compute identical velocity profiles. Inside the recirculation region, slightly larger values are observed in Case 1 as compared to Case 2. Similarly, a larger peak value of the resolved streamwise turbulent stress is observed for the Case 1 (Fig. 6.3(b)). These differences arise due to the different switch-over regions and the corresponding numerical resolutions in this region. As concluded in Ref. [97], earlier switch-over between the RANS and PANS regions improves accuracy, however, is associated with higher computational effort. Therefore, delaying the switch-over location can be preferable, especially in very high Reynolds number flows, as the flow statistics are reasonably predicted in the wake. The remainder of WM-PANS results for the $f_{k(F)} = 0.5$ case are computed using f_k variation prescribed for Case 2.

Recovery of the prescribed physical resolution, f_k in a simulation is an important consistency check in establishing the model's fidelity. This check ensures that the model performs as expected and requisite range of scales are resolved in the flow. In this study, an external consistency check

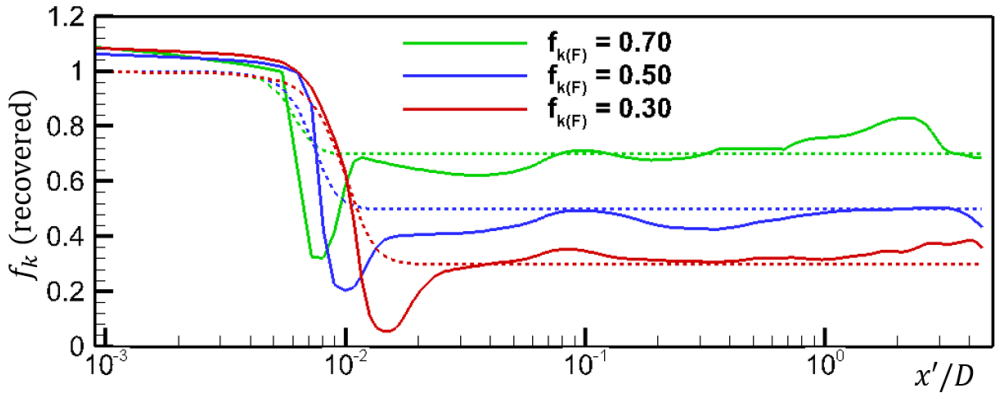

Figure 6.4: External consistency check: recovery of a-priori prescribed f_k ($x = x' + 0.5D$); the dashed lines denote f_k prescribed in the domain according to Table. 6.2 for different WM-PANS computations.

is performed based on $f_{k(F)} = 1.00$ (RANS) eddy viscosity (ν_t) as:

$$f_k(\text{recovered}) = \sqrt{f_\nu} = \sqrt{\frac{\nu_u + \nu_{Tr}}{\nu_t}} \tag{6.2}$$

Fig. 6.4 presents the f_k recovery profiles along the wake centerline for different WM-PANS simulations. The results clearly indicate that the simulations are able to capture the RANS viscosity levels near the sphere. The disagreement observed in the switch-over region is due to the large gradients in the D_{Tr} term. This behavior is also observed in the turbulent channel flow simulations for $Re_\tau = 8000$ [97]. Nevertheless, this disagreement is only confined to the region in the immediate vicinity of the sphere and all the simulations recover the freestream $f_{k(F)}$ prescribed a-priori in the domain according to Table. 6.2.

6.4.2 Flow statistics and integral quantities

The first- and second-order statistics are presented in Figs. 6.5 and 6.6. Mean streamwise velocity ($\overline{U_x}$) along the centerline shows a smaller recirculation region predicted by $f_{(k(F))} = 1.00$ (RANS) and $f_{(k(F))} = 0.70$ simulations. The recirculation region expands as the freestream f_k values are reduced and converges for $f_{k(F)} \leq 0.5$. Fig. 6.5(b) presents the total turbulent kinetic energy ($\overline{k_T}$) profile in the centerline. The results show high turbulent kinetic content near the end

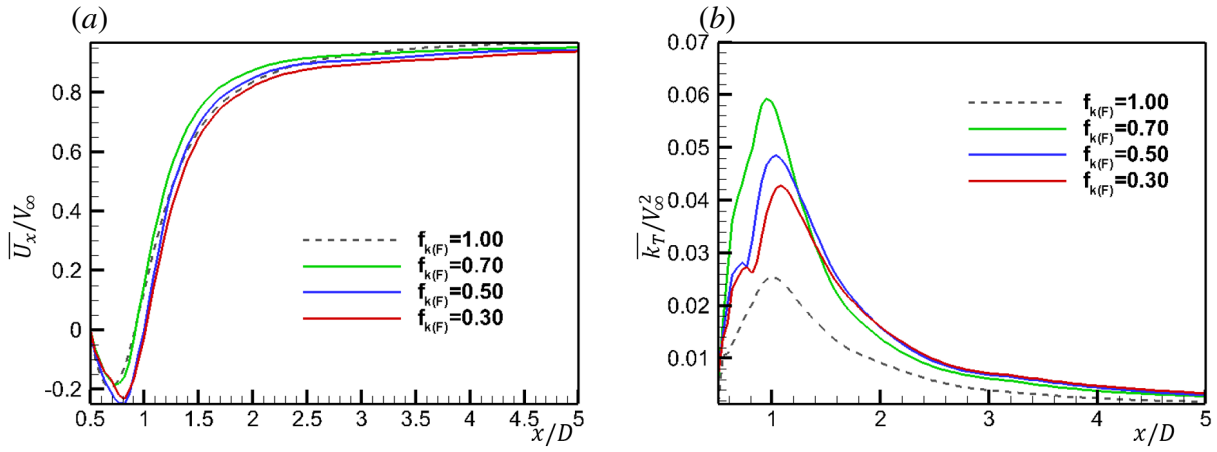

Figure 6.5: (a) Mean streamwise velocity profile and (b) total turbulent kinetic energy ($k_T = k_r$ (resolved) $+ k_u$) in the centerline for different $f_{k(F)}$ simulations

of recirculation bubble ($x/D \approx 1.0$) similar to the DES results of Ref. [5]. Fig. 6.6(a) shows the streamwise velocity profile inside the recirculation region at $x/D = 0.7$. This region is characterized by the 'U' shape of the streamwise velocity profile adjacent to the sphere for the subcritical Reynolds number case [61]. In the supercritical regime, the 'U' shape of the profile is not evident as the flow is fully turbulent in recirculation region. Moreover, higher momentum transfer leads to a smaller velocity deficit in the wake compared to the subcritical regime [61]. The statistics converge for high resolution WM-PANS cases ($f_{(k(F))} = 0.50,\ 0.30$) compared to the low resolution $f_{(k(F))} = 0.70$ case (see, Fig. 6.6(b)).

The mean pressure coefficient ($\overline{C_p}$) around the sphere is presented in Fig. 6.7(a). The results are compared to numerical [5] and experimental [6] studies. The pressure coefficient is predicted well by all WM-PANS simulations compared to the established studies. The angle of minimum pressure coefficient is well captured with a maximum error of 4% in the $\overline{C_p}$ value for the $f_{k(F)} = 0.70$ case. WM-PANS results slightly overpredict the $\overline{C_p}$ values beyond separation ($\phi \geq 120^o$). This disagreement is expected as the small scales generated beyond separation lie predominantly in the RANS and switch-over regions of the WM-PANS model and therefore are not adequately resolved. It should be noted that the DES computations also show similar disagreements with the

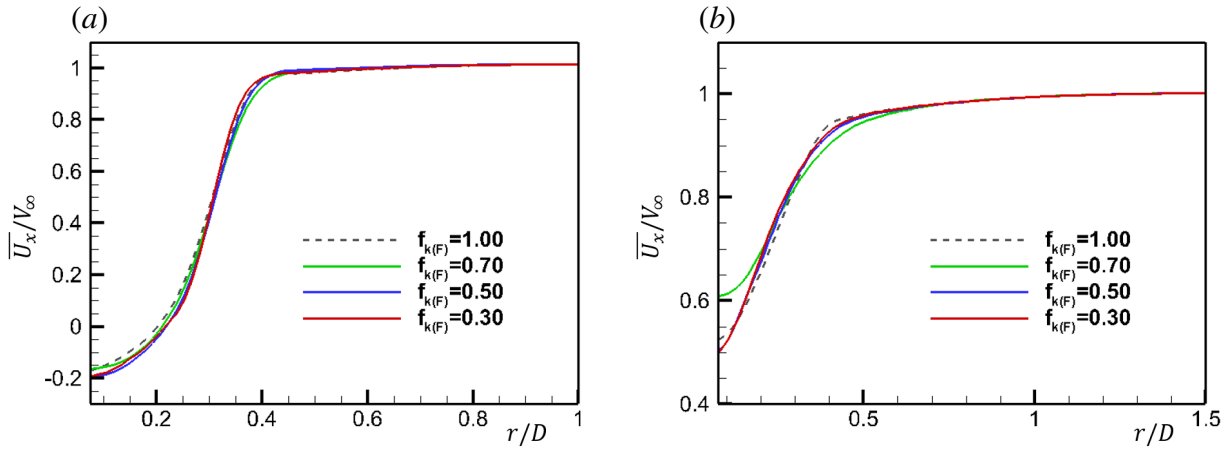

Figure 6.6: Time-averaged streamwise velocity profiles at (a) $x/D = 0.7$ and (b) $x/D = 1.3$ for different $f_{k(F)}$ simulations.

experimental results as the near-wall solution in DES is computed using a RANS model [5].

Fig. 6.7(b) shows the local skin friction distribution around the sphere. The WM-PANS results agree very well with results of the DES simulation for a fully turbulent boundary layer. The results, however, show large deviations between the numerical (WM-PANS and DES) and the experimental results. According to the experiments by Ref. [6], the transition to turbulence occurs in the boundary layers in the flow past a sphere at $Re = 1.14 \times 10^6$. The attached boundary layer stays laminar before the transition to turbulence at $\phi \approx 90^o$ and turbulent separation occurs at $\phi \approx 120^o$. This translates to lower skin friction values captured in the experiments for $\phi \leq 90^o$. In WM-PANS/DES models, the attached boundary layer in the flow is largely in control of the steady RANS region. Therefore, the simulations are unable to capture the complexities associated with transition to turbulence and compute the local skin friction values for a fully turbulent boundary layer case. DES of Ref. [5] uses a method of “controlled transition" to emulate the behavior observed in the experiments. The results seem to improve with this approach, however, differences beyond $\phi \approx 90^0$ are still significant for $Re = 1.14 \times 10^6$. This approach introduces many empirical fixes which are not employed in the present study.

The integral quantities for different WM-PANS simulations are presented in Table. 6.3. The

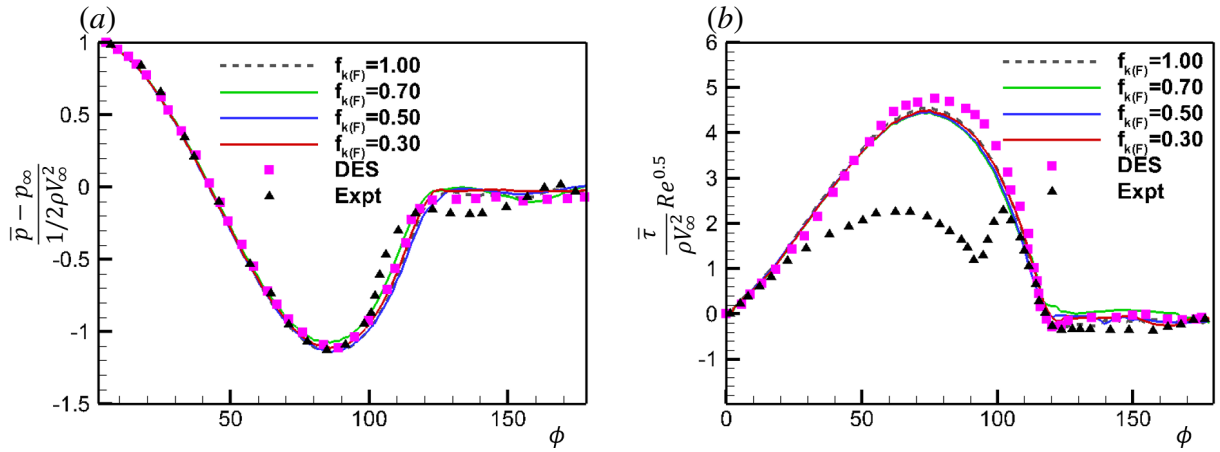

Figure 6.7: (a) Mean pressure coefficient around the sphere; and (b) local skin friction around the sphere for different freestream $f_{k(F)}$ simulations.

Table 6.3: Integral quantities; Time-averaged drag coefficient $\overline{C_d}$, skin friction coefficient C_τ, re-circulation length L_R, time-averaged base pressure coefficient $\overline{C_{pb}}$ and separation angle $\phi_s(^o)$

Study	$\overline{C_d}$	$C_\tau/\overline{C_d}(\%)$	L_R	$\overline{C_{pb}}$	$\phi_s(^o)$
RANS ($f_{k(F)}=1.00$)	0.085	12.1	0.46	-0.038	119.8
PANS ($f_{k(F)}=0.70$)	0.105	14.5	0.46	-0.014	121.5
PANS ($f_{k(F)}=0.50$)	0.095	13.8	0.52	-0.021	119.4
PANS ($f_{k(F)}=0.30$)	0.098	12.2	0.53	-0.041	118.2
DES [5]	0.102	15.2	0.60	-0.069	117
Expt [6]	0.12	7.5	–	-0.037	120

$\overline{C_d}$ values are in good agreement with the DES results. The values are comparable to the RANS simulation ($f_{k(F)}=1.00$) which is expected as the inner region is computed using the RANS model. The ratio of skin friction coefficient (integrated around the sphere) to drag ($C_\tau/\overline{C_d}$) is markedly different from the experimental value but compares better than the DES results. This is again due to the fact that the experimental boundary layer is initially laminar. Other quantities are in good agreement with the studies in literature and the turbulent separation angle of $\phi=120^o$ [6] is well predicted by all cases.

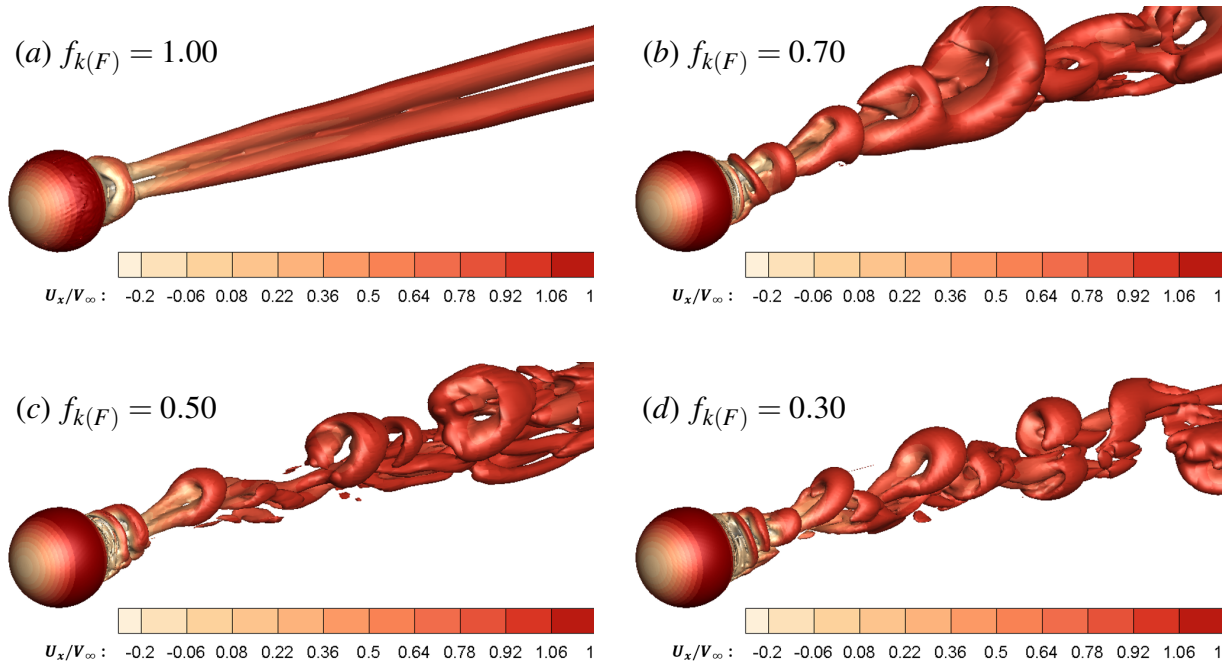

Figure 6.8: Instantaneous Q-factor iso-surfaces for different $f_{k(F)}$ simulations colored with resolved streamwise velocity U_x.

6.4.3 Flow structures

The instantaneous $Q = (S^2 - W^2)/2$ iso-surfaces (S is resolved velocity strain-rate tensor and W is the vorticity-rate tensor) are plotted in Fig. 6.8. The results clearly indicate that hairpin-like vortices are shed in the turbulent wake for $f_{k(F)} = 0.70, 0.50$ and 0.30 cases. The RANS simulation ($f_{k(F)} = 1.00$) does not exhibit any structures in the turbulent wake. An Ω-shaped vortical structure immediately adjacent to the sphere is present in all resolving simulations similar to the flow visualization by Ref. [85]. The iso-surfaces show progressively finer structures as resolution in the wake is increased ($f_{k(F)}$ is reduced).

Based on the first- and second-order flow statistics and flow structures in the wake, it is evident that the results converge for high resolution ($f_{k(F)} = 0.50$ and 0.30) simulations. Therefore, in the subsequent analysis, we would like to further evaluate these high resolution simulations based on their ability to quantitatively capture large-scale structures in the wake.

A spectral proper orthogonal decomposition (POD) approach for analysis of wakes of axisymmetric bodies present in Ref. [61] is employed to evaluate the coherent structures quantitatively in the wake. A Fourier decomposition of streamwise velocity fluctuations ($u_x(r,\theta,t;x)$) at different downstream locations (x/D) is performed in both azimuthal direction (θ) and time. The resulting fluctuating field, $\tilde{u_x}(r,m,f;x)$ is a function of azimuthal mode (m) and frequency (f). A cross-spectral density tensor $\langle \tilde{u_x}(r,m,f;x)\tilde{u_x}(r',m,f;x)\rangle$ is constructed and the eigenvalue problem is solved in the radial direction (r). The modes obtained by this eigvenvalue decomposition in the radial direction are termed as radial modes, n. From the eigendecomposition, the cross-spectral density tensor produces the eigenspectra ($\lambda^{(n)}(m,f;x)$) and the corresponding eigenfunctions ($\psi^{(n)}(r,m,f;x)$). The eigenspectra quantify the modal energy content in different radial (n) and azimuthal (m) modes at corresponding frequencies (f). Similarly, the eigenfunctions delineate the mode shapes of the large-scale structures in the turbulent wake at different fixed downstream locations. A detailed description of this method is present in Ref. [61]. In this study, the first radial mode ($n = 1$) contains almost 95% of the total energy in the radial direction for all frequencies and azimuthal modes (m). Therefore, the large-scale structures are characterized using only the first radial mode for different azimuthal modes and frequencies.

The data for the POD analysis is extracted from three downstream locations; (i) $x/D = 0.7$, inside the recirculation region, (ii) $x/D = 1.3$, outside the recirculation region and (ii) $x/D = 2.5$, the near-wake region. Almost 100 snapshots per shedding cycle are obtained for ten shedding cycles on a polar grid ($r \in [0,\ 1.0D]$, $\theta \in [0^o,\ 360^o]$) with $\Delta r/D = 0.02$ and $\Delta\theta = 2^o$.

The eigenspectrum integrated over frequency ($\xi^{(1)}(m;x)$) value quantifies the total modal energy content in the first radial mode (for all frequencies) as a function of azimuthal mode (m) [61]. This normalized quantity reveals relative dominance of different azimuthal modes at different downstream locations in the wake. The mode, $m = 0$ is the axisymmetric mode loosely linked to the expansion and contraction of the recirculation region. The $m = 1$ mode is the anti-symmetric vortex shedding mode. This mode quantifies the strength of large-scale vortex shedding in the wake of a axisymmetric body. Although, correlation between the $m = 2$ mode and the large-

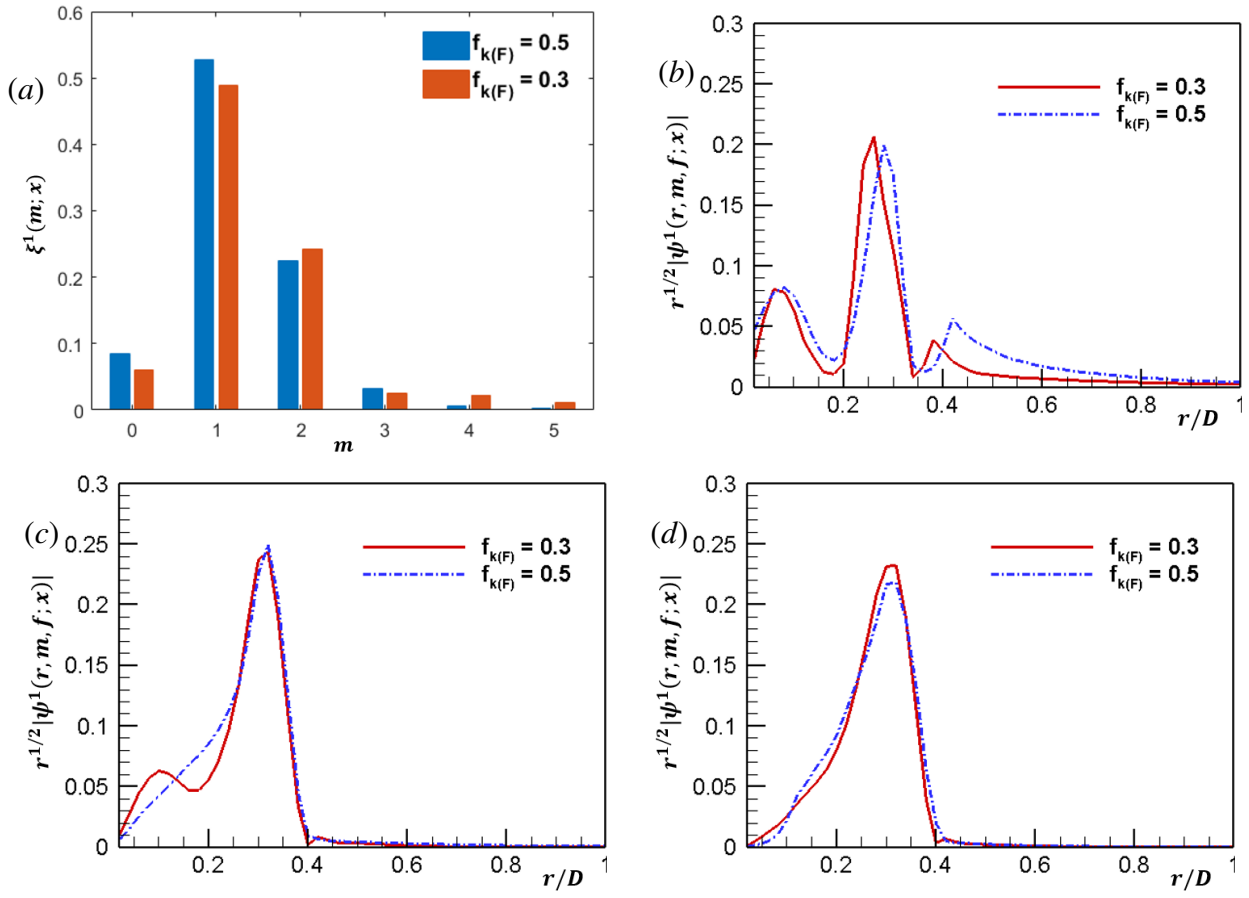

Figure 6.9: (a) Eigenspectrum integrated over frequency ($\xi^{(1)}(m;x)$) as a function of azimuthal mode number (m); Comparison of azimuthal mode shapes ($r^{1/2}|\psi^1(r,m,f;x)|$) for different WM-PANS simulations for azimuthal modes: (b) $m = 0$, (c) $m = 1$ and (d) $m = 2$ at $x/D = 0.7$ (inside the recirculation region).

scale dynamics is unclear, it is found to be dominant at near zero frequencies [74]. Therefore, this mode has a much larger axial scale and the structures at lower modes coalesce in a larger structure at this higher mode as they advect downstream [74].

Fig. 6.9(a) presents the relative contribution of different azimuthal modes ($\xi^{(1)}(m;x)$) inside the recirculation region, i.e., $x/D = 0.7$. In this region, small scales from the separated shear layers coalesce to form the large-scale vortices that are shed in the turbulent wake. The $m = 1$ is the most dominant mode even in this region implying strong vortex shedding begins early in the wake next to the sphere. The $m = 0$ mode has negligible contribution in this region indicating that the recirculation bubble dynamics has a minor contribution in the overall wake configuration. It is evident that both $f_k = 0.50$ and 0.30 simulations capture similar modal energy content in all the mode shapes. The $f_{k(F)} = 0.50$ case captures a slightly higher modal energy content in the $m = 1$ mode and lower content in higher modes due to its inability to resolve smaller scales compared to the $f_{k(F)} = 0.30$ simulation. Comparisons of mode shapes for different azimuthal modes are presented in Figs. 6.9(b), 6.9(c) and 6.9(d) for the two WM-PANS simulations. The mode shapes of the dominant $m = 1$ and $m = 2$ modes are reasonably captured by $f_{k(F)} = 0.50$ simulation compared to the $f_{k(F)} = 0.30$ simulation. The slight disagreement below $r/D \leq 0.25$ can be attributed to the large differences in mesh resolutions between the two simulations (see, Table. 6.1) in the near-wake region.

Figs. 6.10 and 6.11 present the modal energy content and mode shapes at two locations in the near-wake region. At the location $x/D = 1.3$ (just outside the recirculation region), the $m = 1$ mode has the clear anti-symmetric pattern (Fig. 6.10(c)). The shapes and energy content of the dominant modes are predicted very well by the $f_{k(F)} = 0.50$ simulation as compared to the high resolution $f_{k(F)} = 0.30$ simulation. In the wake region, i.e., at $x/D = 2.5$ (Fig. 6.11), the mode shapes present a significant disagreement between the two simulations. At this location, the grid sizes are $\Delta_{x(max)}/D = 0.01$ (G_3) for $f_{k(F)} = 0.50$ case and $\Delta_{x(max)}/D = 0.002$ for $f_{k(F)} = 0.30$ case. Moreover, the effective viscosity ($\nu_{eff} = \nu + \nu_u + \nu_{Tr}$) is substantially higher for the $f_{k(F)} = 0.50$ case. Therefore, the large-scale structures diffuse at a higher rate as they move downstream for

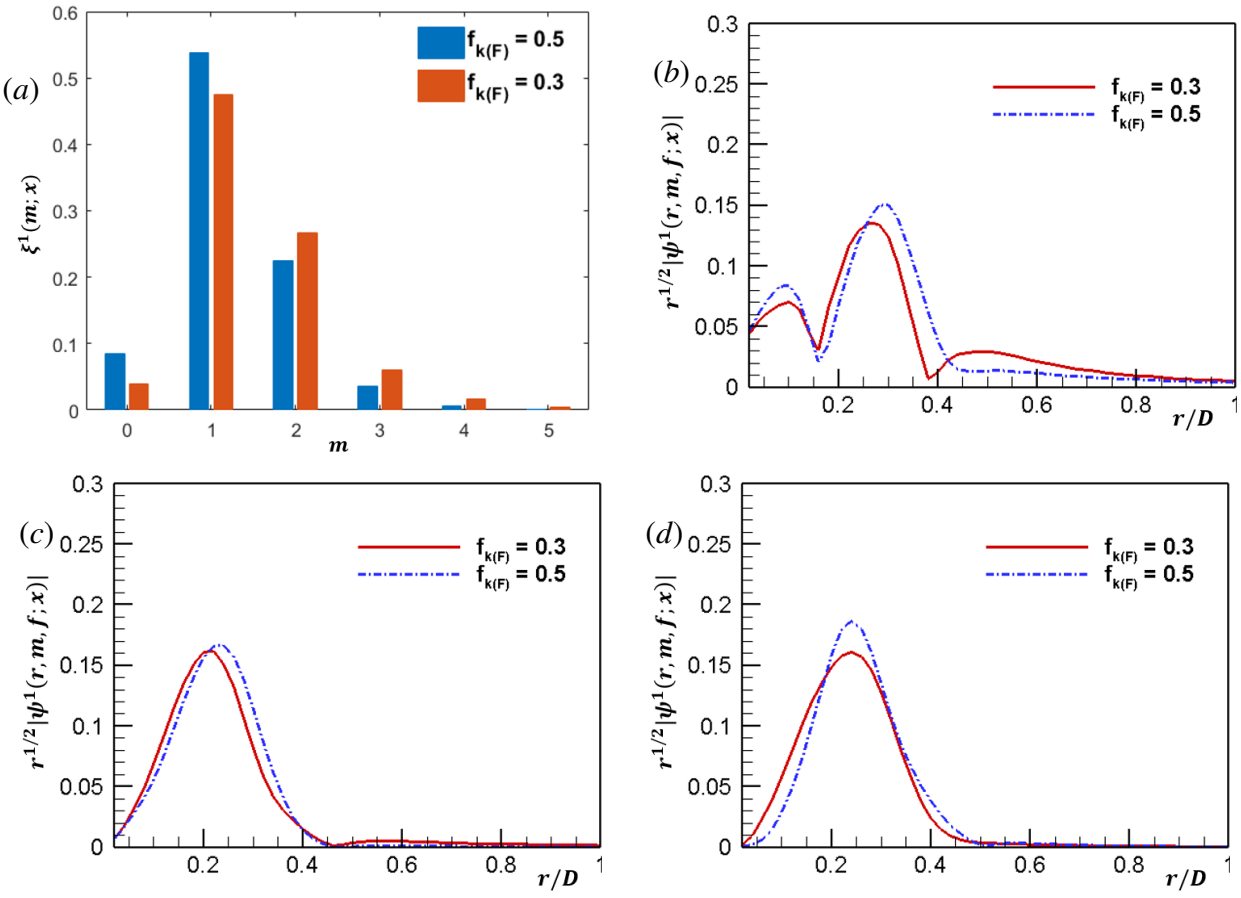

Figure 6.10: Same as Fig. 6.9 at $x/D = 1.3$

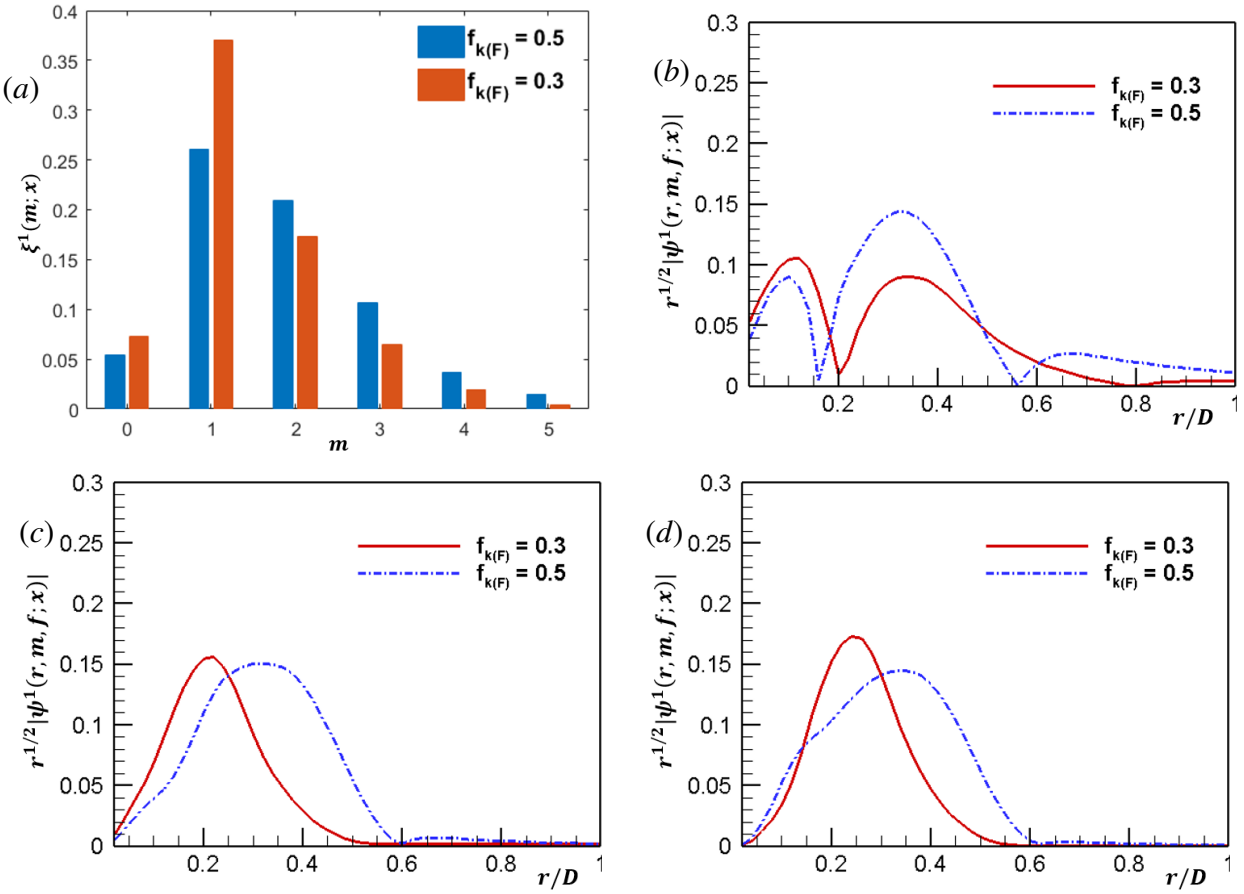

Figure 6.11: Same as Fig. 6.9 at $x/D = 2.5$

the low resolution simulation which has also been observed in the subcritical simulations (See, Ref. [61]). This also leads to a smaller contribution of the $m = 1$ mode captured by the $f_{k(F)} = 0.50$ simulation as POD is unable to recover these weak large-scale correlations.

6.4.3.1 Comparison between subcritical and supercritical regimes

Flow past subcritical and supercritical regimes display distinct differences with respect to the wake configuration. The time-averaged streamlines in both the regimes are presented in Fig. 6.12. The recirculation region near the sphere in the supercritical regime is fully turbulent with a significant shrinkage in the recirculation bubble ($L_R \approx 0.5$) as a result of high turbulent momentum transfer compared to the subcritical region ($L_R \approx 2.72$).

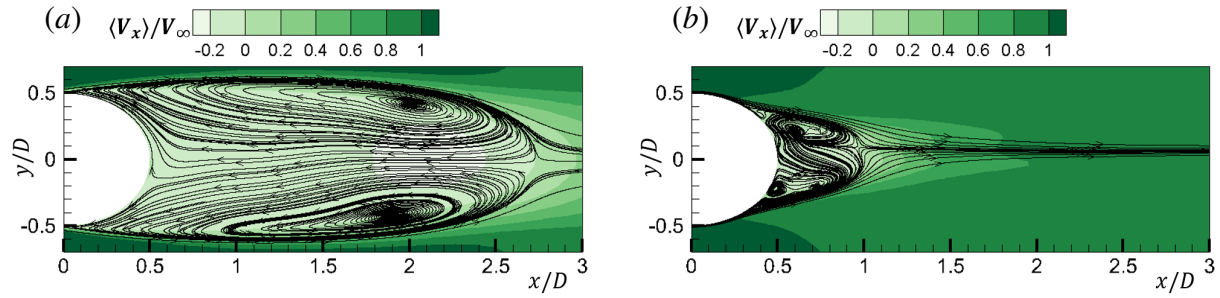

Figure 6.12: Mean streamwise velocity contours overlaid with the time-averaged streamlines for (a) $Re = 3700$ (subcritical) and (b) $Re = 1.14 \times 10^6$ (supercritical)

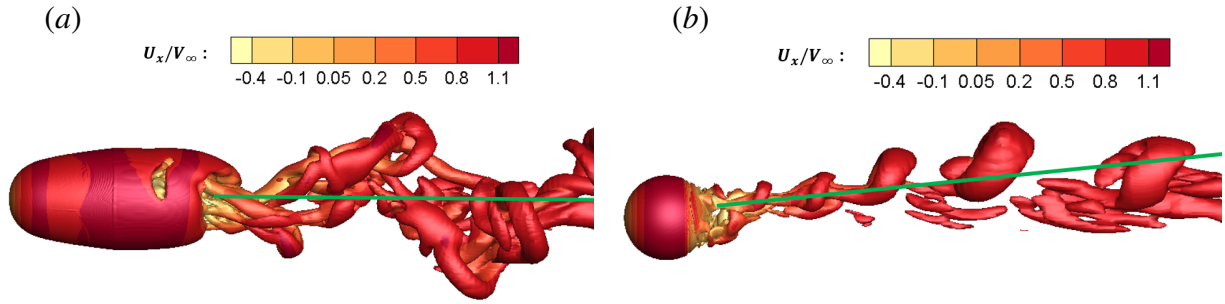

Figure 6.13: Instantaneous Q-factor iso-surfaces for (a) $Re = 3700$ (subcritical) and (b) $Re = 1.14 \times 10^6$ (supercritical). Solid green line represents the average orientation of the wake.

In the supercritical regime, the wake becomes ordered and highly compact (Fig. 6.13(b)). The spiral instability mode responsible for wave-like motion of the wake is absent in the supercritical regime [5] and any progressive wave motion is not discernible as compared to the subcritical wake.

Another distinct difference in the wake configurations is the tilting of the wake in supercritical regime. According to Ref. [85], the flow visualization experiments also confirmed the tilting of the wake due to a side force experienced by the sphere beyond the critical Reynolds number. Ref. [5] speculated that this lateral force on the sphere is due to the successive shedding of hairpin like vortices at a fixed azimuthal angle over long periods of time. Examination of multiple shedding cycles revealed a similar locking of azimuthal location from which the vortices are consistently shed in all WM-PANS simulations. This azimuthal location at which locking of the wake occurs is

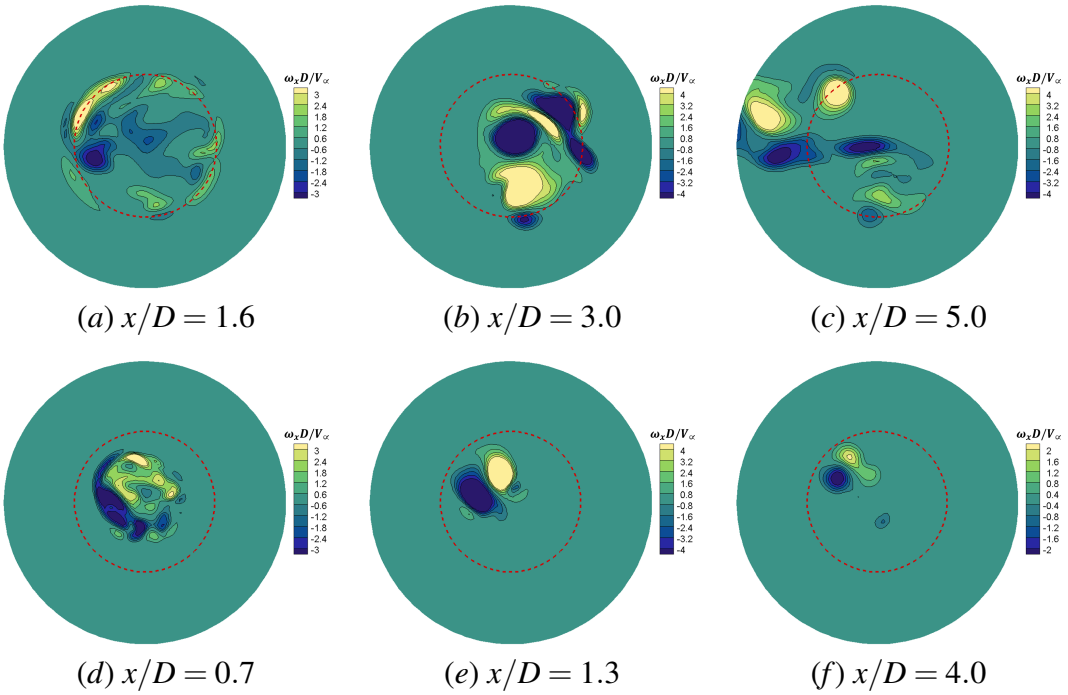

$(a)\ x/D = 1.6$ $(b)\ x/D = 3.0$ $(c)\ x/D = 5.0$

$(d)\ x/D = 0.7$ $(e)\ x/D = 1.3$ $(f)\ x/D = 4.0$

Figure 6.14: Instantaneous streamwise vorticity (ω_x) contours at different locations in the wake for $Re = 3700$ $((a),\ (b),\ (c))$ and $Re = 1.14 \times 10^6$ $((d),\ (e),\ (f))$

different for each simulation. Therefore, it can be deduced that this location is completely random and highly sensitive to initial perturbations in the flow field.

Fig. 6.14 presents the vorticity contours at different locations for both subcritical and supercritical Reynolds number regimes. A chaotic wake with small scale structures inside the recirculation region is evident for both regimes (Fig. 6.14(a) and Fig. 6.14(d)). In the supercritical regime, a pair of counter-rotating vortices beyond the recirculation region can be clearly observed (Fig. 6.14(e)). In subcritical flow regime, vortices are shed from random azimuthal locations every shedding cycle [61]. This can be seen here as different orientations of the vorticity field as the downstream location is changed. However, for the supercritical regime, the orientation of the vorticity field is maintained as the vortices are shed from the same location for extended periods of time creating a lateral force on the sphere.

7. SUMMARY AND CONCLUSIONS

Computational fluid dynamics (CFD)-based numerical wave tanks (CNWTs) are emerging as key design tools for many ocean systems. One of the key challenges toward their development is the need for a variable fidelity turbulence model. The partially-averaged Navier-Stokes (PANS) method is ideally suited to perform multi-fidelity simulations for the CNWTs. The PANS method captures majority of the flow physics rendering them more accurate than the current RANS closures. The computational efficiency and robustness of the PANS closures presented in this dissertation make them highly advantageous compared to the high fidelity simulations, e.g. DNS and LES. Now, a detailed summary and key conclusions from each study are presented.

In the **first study**, we present the development of the PANS two-layer turbulence model. The two-layer turbulence model combines the simplicity and robustness of a one-equation model in the viscous near-wall region with the accuracy of the $k-\varepsilon$ turbulence model in the outer region. The PANS two-layer model equations are derived from their parent RANS counterparts. Closure coefficients and the length scale formulations for the inner layer of the PANS two-layer model have been systematically developed based on the scaling of turbulent quantities in the near-wall and log layer region. The fidelity of this two-layer PANS formulation is investigated in a channel flow with $Re_\tau = 180-950$. One-point statistics predicted by the PANS two-layer turbulence model are found to be in excellent agreement with the DNS data. The PANS two-layer model successfully produces turbulent stresses and vorticity fluctuations in good agreement with the data. The fidelity of the model is further verified via recovery of the prescribed physical resolution and the invariant map.

In the **second study**, we investigate and characterize the wake of the flow past a sphere using the scale-resolving PANS method [31]. In this flow, large-scale vortex shedding and small-scale Kelvin-Helmholtz (KH) instability in the shear layer lead to the formation of complex coherent structures. These wake coherent structures exert a strong influence on flow statistics in nearly all regions of the flow. Hence, it is important to adequately resolve the structures to accurately

determine quantities of engineering interest. The wake flow at subcritical Reynolds number, $Re = 3700$, is simulated at four levels of physical resolution (cut-off): $f_k = 0.5,\ 0.3,\ 0.2$ and 0.1. Lower f_k values correspond to smaller cut-off scales and $f_k = 0.1$ case represents the finest resolution approaching the LES limit.

The focus of the first part of the study is to establish the degree of resolution required for accurately computing various flow features such as coefficients of drag and lift, profiles of one-point statistics, frequency spectra and coherent structures. The key findings are:

1. Flow statistics and integral quantities are captured reasonably well by all physical resolution with $f_k \leq 0.5$. Although the large-scale vortex shedding instability is distinctly captured by all physical resolution cases, the small-scale KH frequency is satisfactorily resolved only for $f_k \leq 0.3$. This indicates that the coarser resolutions simulate lower effective Reynolds number (Re_{eff}) which leads to truncated development of the key instabilities in the flow. These findings also suggest that one-point statistics are more influenced by vortex shedding than the KH instability in most regions of the flow.

2. Convergence of large-scale structures in terms of mode shapes $(\psi^1(r,m,f;x))$ and modal energy content $(\lambda^1(m,f;x))$ is only observed in $f_k \leq 0.2$. This clearly indicates that adequately resolving the KH instability is important to capture the details of the coherent structures.

In the second part of the study, we characterize the coherent structure in the wake of the sphere and compare it with the key features of other axisymmetric wakes. The findings are:

1. An axisymmetric 'bubble-pumping' mode $(m = 0)$ is dominant inside the recirculation region. This mode oscillates at a very low-frequency of $S_t = 0.05$. The contribution of this mode to the overall energy content steadily decreases as the distance from the sphere is increased.

2. Mode $m = 1$ is the anti-symmetric mode related to the large-scale vortex shedding. This mode becomes dominant just outside the recirculation region and its effect continues in the near-wake region.

3. Mode $m = 2$ oscillates at the sub-harmonic of f_{vs} and becomes the second-most dominant mode beyond $x/D \geq 5.0$.

All these features are very similar to the large-scale behavior in the near-wake region of other axisymmetric bodies such as a disk [1]. This study clearly exhibits that PANS is capable of accounting for the effects of coherent structures on key engineering quantities of interest and one-point flow statistics at coarse resolutions compared to LES[78]. On a Cartesian body fitted grid used in this study, the numerical resolution requirement of the PANS simulations are substantially lower than other high fidelity simulations[82]. Further, at sufficient resolution, PANS is shown to capture the details of coherent structure with good precision.

In the **third study**, the near-wall treatment of the PANS-SRS model using spatially varying physical resolution is investigated. The commutation residue originating due to the implicit filter variation is systematically derived based on the energy conservation principle. The results clearly demonstrate the advantage of using WM-PANS approach for coarse grid resolutions compared to the WR-PANS.

The WM-PANS approach is evaluated in two different flow types:

1. WM-PANS is employed to perform simulations of turbulent channel flow at Reynolds number of $Re_\tau = 950, 8000$. It is shown that the WM-PANS reasonably captures the flow physics at $Re_\tau = 8000$ without discernible log-layer mismatch. The underlying reason for a small twitch observed in the first- and second-order statistics is explained using a computational buffer region analogy. It is also shown that the flow structures are adequately resolved sufficiently away from the switch-over region irrespective of the location of the switch-over.

2. WM-PANS is further investigated in the flow past a sphere at $Re = 3700$. WM-PANS captures the integral quantities and first- and second-order flow statistics with significant accuracy on coarse grids. WM-PANS results on the coarsest mesh (1.5 million cells) are shown to be comparable to the results of the finest grid (6.90 million cells) on WR-PANS allowing for significant computational savings.

In the **fourth** study, the WM-PANS approach from Study 3 is employed to compute flow past a sphere at a very high Reynolds number of $Re = 10^6$. The resolution of near-wall region in thin boundary layers at high Reynolds numbers is a major computational challenge for wall-resolved turbulence models such as WR-SRS and LES. The near-wall region of these boundary layers is fully modeled in the WM-PANS strategy reducing the overall computational burden.

Flow around a sphere at high Reynolds number of $Re = 1.14 \times 10^6$ is selected due to its inherent complexities: (i) thin turbulent boundary layer development, (ii) turbulent separation and (iii) a fully turbulent three dimensional wake. The wake characteristics are investigated at different freestream $f_{k(F)}$ values: (i) $f_{k(F)} = 1.00$, (ii) $f_{k(F)} = 0.70$, (iii) $f_{k(F)} = 0.50$ and (iv) $f_{k(F)} = 0.30$. The integral quantities and flow statistics are first analyzed. The conclusions are:

1. The model, to a large-extent, is insensitive to the switch-over region. However, the f_k variation must ensure reasonable manifestation of underlying instabilities.

2. The simulations recover the prescribed physical resolution, $f_{k(F)}$ adequately thereby establishing the model's fidelity.

3. The integral quantities are captured reasonably well by all WM-PANS simulations compared to the DES simulations of a fully turbulent boundary layer by Ref. [5] and the first- and second-order flow statistics converge for $f_{k(F)} \leq 0.50$.

The flow structures are further verified both qualitatively and quantitatively. The quantitative comparison between the $f_{k(F)} = 0.50$ and $f_{k(F)} = 0.30$ cases is performed using the POD approach outlined in Ref. [61]. The key findings are:

1. Large-scale structures agree well for both cases in terms of mode shapes ($\psi^1(r,m,f;x)$) and modal energy content ($\lambda^1(m,f;x)$). Some disagreement is seen at $x/D = 2.5$ as the vortices diffuse at a higher rate for the $f_{k(F)} = 0.50$ case due to a coarse grid resolution in the wake compared to the $f_{k(F)} = 0.30$ case.

2. The anti-symmetric shedding mode, $m = 1$ is found to be the most dominant mode at all locations in the wake considered in this study. It has 50% contribution to the total kinetic energy

content unlike the subcritical regime where $m = 0$ mode is dominant inside the recirculation region [61].

3. The qualitative analysis of the wake reveals that the wake organizes in a similar configuration as was observed in the numerical studies [5].

Each of the studies presented in this dissertation establishes PANS models as highly accurate and computationally efficient tools to overcome different challenges faced in the simulation of NWTs as given below:

1. The two-layer modelling strategy presented in the first study requires relatively lesser number of grid points near the wall compared to the other WR-PANS models. This model can easily replace the popular RANS $k-\varepsilon$ closures used in CNWTs whilst providing increased accuracy.

2. The second study reveals that the large-scale coherent structures in the flow field are accurately captured by WR-PANS. This is essential as the wake dynamics of ship's superstructure, flexible marine risers or offshore wind turbines can largely affect their stability and structural integrity. Moreover, accurate wake predictions are important in determining responses of the structures in the downstream of the wake.

3. The third and fourth studies evaluate the efficacy of a WM-PANS approach in computing practical flows at high Reynolds number. WM-PANS approach is shown to be reasonably accurate at very coarse numerical resolutions. This is desirable for simulations of full-scale marine vehicles where the operating Reynolds numbers are very large and the near-wall region of the thin boundary layer must be modeled.

REFERENCES

[1] E. Berger, D. Scholz, and M. Schumm, "Coherent vortex structures in the wake of a sphere and a circular disk at rest and under forced vibrations," *Journal of Fluids and Structures*, vol. 4, no. 3, pp. 231–257, 1990.

[2] I. Rodriguez, R. Borell, O. Lehmkuhl, C. D. Perez Segarra, and A. Oliva, "Direct numerical simulation of the flow over a sphere at $Re = 3700$," *Journal of Fluid Mechanics*, vol. 679, p. 263–287, 2011.

[3] I. Rodríguez, O. Lehmkuhl, R. Borrell, and A. Oliva, "Flow dynamics in the turbulent wake of a sphere at sub-critical Reynolds numbers," *Computers & Fluids*, vol. 80, pp. 233–243, 2013.

[4] Y. Yamamoto and Y. Tsuji, "Numerical evidence of logarithmic regions in channel flow at $Re_\tau = 8000$," *Physical Review Fluids*, vol. 3, no. 1, p. 012602, 2018.

[5] G. Constantinescu and K. Squires, "Numerical investigations of flow over a sphere in the subcritical and supercritical regimes," *Physics of fluids*, vol. 16, no. 5, pp. 1449–1466, 2004.

[6] E. Achenbach, "Experiments on the flow past spheres at very high Reynolds numbers," *Journal of Fluid Mechanics*, vol. 54, no. 3, pp. 565–575, 1972.

[7] C. Windt, J. Davidson, and J. V. Ringwood, "Investigation of turbulence modeling for point-absorber-type wave energy converters," *Energies*, vol. 14, no. 1, p. 26, 2021.

[8] S. A. Brown, V. Magar, D. M. Greaves, and D. C. Conley, "An evaluation of RANS turbulence closure models for spilling breakers," *Coastal Engineering Proceedings*, no. 34, pp. 5–5, 2014.

[9] A. Calderer, X. Guo, L. Shen, and F. Sotiropoulos, "Fluid–structure interaction simulation of floating structures interacting with complex, large-scale ocean waves and atmospheric turbu-

lence with application to floating offshore wind turbines," *Journal of Computational Physics*, vol. 355, pp. 144–175, 2 2018.

[10] M. Silva, M. Vitola, P. Esperança, S. Sphaier, and C. Levi, "Numerical simulations of wave–current flow in an ocean basin," *Applied Ocean Research*, vol. 61, pp. 32–41, 2016.

[11] A. Davies and J. Lawrence, "Examining the influence of wind and wind wave turbulence on tidal currents, using a three-dimensional hydrodynamic model including wave–current interaction," *Journal of Physical Oceanography*, vol. 24, no. 12, pp. 2441–2460, 1994.

[12] G. Failla and F. Arena, "New perspectives in offshore wind energy," *Philosophical Transactions of the Royal Society A: Mathematical, Physical and Engineering Sciences*, vol. 373, no. 2035, p. 20140228, 2015.

[13] H. Chen, L. Qian, Z. Ma, W. Bai, Y. Li, D. Causon, and C. Mingham, "Application of an overset mesh based numerical wave tank for modelling realistic free-surface hydrodynamic problems," *Ocean Engineering*, vol. 176, pp. 97–117, 3 2019.

[14] F. Stern, J. Yang, Z. Wang, H. Sadat-Hosseini, M. Mousaviraad, S. Bhushan, and T. Xing, "Computational ship hydrodynamics: Nowadays and way forward," *International Shipbuilding Progress*, vol. 60, no. 1-4, pp. 3–105, 2013.

[15] J. Westphalen, D. M. Greaves, C. J. Williams, A. C. Hunt-Raby, and J. Zang, "Focused waves and wavestructure interaction in a numerical wave tank," *Ocean Engineering*, vol. 45, pp. 9–21, 5 2012.

[16] X. Tian, Q. Wang, G. Liu, W. Deng, and Z. Gao, "Numerical and experimental studies on a three-dimensional numerical wave tank," *IEEE Access*, vol. 6, pp. 6585–6593, 1 2018.

[17] A. M. Miquel, A. Kamath, M. A. Chella, R. Archetti, and H. Bihs, "Analysis of different methods for wave generation and absorption in a CFD-based numerical wave tank," *Journal of Marine Science and Engineering*, vol. 6, 6 2018.

[18] B. Sanderse, S. Van der Pijl, and B. Koren, "Review of computational fluid dynamics for wind turbine wake aerodynamics," *Wind energy*, vol. 14, no. 7, pp. 799–819, 2011.

[19] D. C. Wilcox, *Turbulence modeling for CFD*, vol. 2. DCW industries La Canada, CA, 1998.

[20] P. R. Spalart, "Detached-eddy simulation," *Annual review of fluid mechanics*, vol. 41, pp. 181–202, 2009.

[21] M. Young and A. Ooi, "Comparative assessment of LES and URANS for flow over a cylinder at a Reynolds number of 3900," *16th Australasian Fluid Mechanics Conference*, 2007.

[22] T. Nishino, G. Roberts, and X. Zhang, "Unsteady RANS and detached-eddy simulations of flow around a circular cylinder in ground effect," *Journal of Fluids and Structures*, vol. 24, no. 1, pp. 18–33, 2008.

[23] P. Moin and K. Mahesh, "Direct numerical simulation: a tool in turbulence research," *Annual review of fluid mechanics*, vol. 30, no. 1, pp. 539–578, 1998.

[24] U. Piomelli and E. Balaras, "Wall-layer models for large-eddy simulations," *Annual review of fluid mechanics*, vol. 34, no. 1, pp. 349–374, 2002.

[25] P. R. Spalart, "Comments on the feasibility of LES for wings, and on a hybrid RANS/LES approach," in *Proceedings of first AFOSR international conference on DNS/LES*, Greyden Press, 1997.

[26] M. S. Gritskevich, A. V. Garbaruk, J. Schütze, and F. R. Menter, "Development of DDES and IDDES formulations for the k-ω shear stress transport model," *Flow, turbulence and combustion*, vol. 88, no. 3, pp. 431–449, 2012.

[27] J. Kok, H. Dol, B. Oskam, and H. van der Ven, "Extra-large eddy simulation of massively separated flows," in *42nd AIAA Aerospace Sciences Meeting and Exhibit*, p. 264, 2004.

[28] F. R. Menter, "Best practice: scale-resolving simulations in ANSYS CFD," *ANSYS Germany GmbH*, vol. 1, 2012.

[29] F. Menter, M. Kuntz, and R. Bender, "A scale-adaptive simulation model for turbulent flow predictions," in *41st aerospace sciences meeting and exhibit*, p. 767, 2003.

[30] B. Chaouat and R. Schiestel, "A new partially integrated transport model for subgrid-scale stresses and dissipation rate for turbulent developing flows," *Physics of Fluids*, vol. 17, no. 6, p. 065106, 2005.

[31] S. S. Girimaji, "Partially-averaged Navier-Stokes model for turbulence: A Reynolds-averaged Navier-Stokes to direct numerical simulation bridging method," *Journal of Applied Mechanics*, vol. 73, pp. 413– 421, 2006.

[32] S. S. Girimaji, R. Srinivasan, and E. Jeong, "PANS turbulence model for seamless transition between RANS and LES: fixed-point analysis and preliminary results," in *Fluids Engineering Division Summer Meeting*, vol. 36975, pp. 1901–1909, 2003.

[33] S. Girimaji and K. Abdol-Hamid, "Partially-averaged Navier-Stokes model for turbulence: Implementation and validation," in *43rd AIAA Aerospace Sciences Meeting and Exhibit*, p. 502, 2005.

[34] S. S. Girimaji, E. Jeong, and R. Srinivasan, "Partially averaged Navier-Stokes method for turbulence: Fixed point analysis and comparison with unsteady partially averaged navier-stokes," *Journal of Applied Mechanics, Transactions ASME*, 2006.

[35] M. Germano *et al.*, "Turbulence - the filtering approach," *Journal of Fluid Mechanics*, vol. 238, no. 1, pp. 325–336, 1992.

[36] C. G. Speziale, "On nonlinear kl and k-ε models of turbulence," *Journal of Fluid Mechanics*, vol. 178, pp. 459–475, 1987.

[37] W. Rodi, "A new algebraic relation for calculating the Reynolds stresses," in *Gesellschaft Angewandte Mathematik und Mechanik Workshop Paris France*, vol. 56, p. 219, 1976.

[38] D. A. Reyes, J. M. Cooper, and S. S. Girimaji, "Characterizing velocity fluctuations in partially resolved turbulence simulations," *Physics of Fluids*, vol. 26, no. 8, p. 085106, 2014.

[39] S. S. Girimaji and S. Wallin, "Closure modeling in bridging regions of variable-resolution (VR) turbulence computations," *Journal of Turbulence*, vol. 14, no. 1, pp. 72–98, 2013.

[40] P. Razi, "Partially-averaged Navier-Stokes (PANS) method for turbulence simulations: Near-wall modeling and smooth-surface separation computations," 2017.

[41] P. Tazraei and S. S. Girimaji, "Scale-resolving simulations of turbulence: Equilibrium boundary layer analysis leading to near-wall closure modeling," *Physical Review Fluids*, vol. 4, no. 10, p. 104607, 2019.

[42] F. S. Pereira, L. Eça, G. Vaz, and S. S. Girimaji, "Challenges in scale-resolving simulations of turbulent wake flows with coherent structures," *Journal of Computational Physics*, vol. 363, pp. 98–115, 2018.

[43] C. S. Song and S. O. Park, "Numerical simulation of flow past a square cylinder using partially-averaged Navier-Stokes model," *Journal of Wind Engineering and Industrial Aerodynamics*, vol. 97, no. 1, pp. 37–47, 2009.

[44] E. Jeong and S. S. Girimaji, "Partially averaged Navier-Stokes (PANS) method for turbulence simulations-flow past a square cylinder," *Journal of Fluids Engineering, Transactions of the ASME*, vol. 132, 2010.

[45] S. Lakshmipathy and S. S. Girimaji, "Partially averaged Navier-Stokes (PANS) method for turbulence simulations: Flow past a circular cylinder," *Journal of Fluids Engineering, Transactions of the ASME*, vol. 132, 2010.

[46] F. S. Pereira, G. Vaz, L. Eça, and S. S. Girimaji, "Simulation of the flow around a circular cylinder at $Re = 3900$ with partially-averaged Navier-Stokes equations," *International Journal of Heat and Fluid Flow*, vol. 69, pp. 234–246, 2 2018.

[47] F. S. Pereira, L. Eça, G. Vaz, and S. S. Girimaji, "On the simulation of the flow around a circular cylinder at $Re = 140,000$," *International Journal of Heat and Fluid Flow*, vol. 76, pp. 40–56, 2019.

[48] A. Frendi, A. Tosh, and S. Girimaji, "Flow Past a Backward-Facing Step: Comparison of PANS, DES and URANS Results with Experiments," *International Journal for Computational Methods in Engineering Science and Mechanics*, vol. 8, no. 1, pp. 23–38, 2006.

[49] R. Huang, X. Luo, B. Ji, and Q. Ji, "Turbulent flows over a backward facing step simulated using a modified partially averaged Navier–Stokes model," *Journal of Fluids Engineering*, vol. 139, no. 4, 2017.

[50] B. Basara, S. Krajnovi, S. Girimaji, and Z. Pavlovic, "Near-wall formulation of the partially averaged Navier-Stokes turbulence model," *AIAA Journal*, vol. 49, pp. 2627–2636, 12 2011.

[51] J. M. Ma, S. H. Peng, L. Davidson, and F. J. Wang, "A low Reynolds number variant of partially-averaged Navier-Stokes model for turbulence," *International Journal of Heat and Fluid Flow*, vol. 32, pp. 652–669, 6 2011.

[52] D. Luo, C. Yan, and X. Wang, "Computational study of supersonic turbulent-separated flows using partially averaged Navier-Stokes method," *Acta Astronautica*, vol. 107, pp. 234–246, 2015.

[53] S. Krajnović, R. Lárusson, and B. Basara, "Superiority of PANS compared to LES in predicting a rudimentary landing gear flow with affordable meshes," *International Journal of Heat and Fluid Flow*, vol. 37, pp. 109–122, 2012.

[54] Y. Wang, B. Song, W. Song, and Z.-h. Han, "Partially-averaged Navier-Stokes simulations of unsteady flow around a NACA 0021 airfoil at 60 degrees angle of attack," in *2018 Applied Aerodynamics Conference*, p. 4210, 2018.

[55] B. Ji, X. Luo, Y. Wu, X. Peng, and H. Xu, "Partially-averaged Navier-Stokes method with modified $k-\varepsilon$ model for cavitating flow around a marine propeller in a non-uniform wake," *International Journal of Heat and Mass Transfer*, vol. 55, pp. 6582–6588, 2012.

[56] J. Zhang, G. Minelli, A. N. Rao, B. Basara, R. Bensow, and S. Krajnović, "Comparison of PANS and LES of the flow past a generic ship," *Ocean Engineering*, vol. 165, pp. 221–236, 2018.

[57] B. Basara, S. Krajnovic, Z. Pavlovic, and P. Ringqvist, "Performance analysis of partially-averaged Navier-Stokes method for complex turbulent flows," in *6th AIAA Theoretical Fluid Mechanics Conference*, p. 3106, 2011.

[58] Y. Qian, T. Wang, Y. Yuan, and Y. Zhang, "Comparative study on wind turbine wakes using a modified partially-averaged Navier-Stokes method and large eddy simulation," *Energy*, vol. 206, 9 2020.

[59] H. C. Chen and V. C. Patel, "Near-wall turbulence models for complex flows including separation," *AIAA Journal*, vol. 26, pp. 641–648, 1988.

[60] C. Kamble, S. S. Girimaji, and H.-C. Chen, "Partially averaged Navier-Stokes formulation of a two-layer turbulence model," *AIAA Journal*, vol. 58, no. 1, pp. 174–183, 2020.

[61] C. Kamble and S. Girimaji, "Characterization of coherent structures in turbulent wake of a sphere using partially averaged Navier-Stokes (PANS) simulations," *Physics of Fluids*, vol. 32, no. 10, p. 105110, 2020.

[62] S. Lakshmipathy and S. S. Girimaji, "Partially-averaged Navier-Stokes method for turbulent flows: $k-\omega$ model implementation," in *Collection of Technical Papers - 44th AIAA Aerospace Sciences Meeting*, vol. 3, pp. 1504–1518, 2006.

[63] A. Rao, G. Minelli, B. Basara, and S. Krajnović, "On the two flow states in the wake of a hatchback Ahmed body," *Journal of Wind Engineering and Industrial Aerodynamics*, vol. 173, pp. 262 – 278, 2018.

[64] F. R. Menter, "Two-equation eddy-viscosity turbulence models for engineering applications," *AIAA Journal*, vol. 32, pp. 1598–1605, 1994.

[65] W. Rodi, "Experience with two-layer models combining the $k-\varepsilon$ model with a one-equation model near the wall," in *29th Aerospace Sciences Meeting*, p. 216, 1991.

[66] M. Wolfshtein, "The velocity and temperature distribution in one-dimensional flow with turbulence augmentation and pressure gradient," *International Journal of Heat and Mass Transfer*, vol. 12, pp. 301–318, 1969.

[67] E. R. V. Driest, "On turbulent flow near a wall," *Journal of the Aeronautical Sciences*, vol. 23, no. 11, pp. 1007–1011, 1956.

[68] D. R. Chapman and G. D. Kuhn, "The limiting behaviour of turbulence near a wall," *Journal of Fluid Mechanics*, vol. 170, pp. 265–292, 1986.

[69] R. D. Moser, J. Kim, and N. N. Mansour, "Direct numerical simulation of turbulent channel flow up to $Re_\tau = 590$," *Physics of Fluids*, vol. 11, pp. 943–945, 1999.

[70] S. Hoyas and J. Jiménez, "Reynolds number effects on the Reynolds-stress budgets in turbulent channels," *Physics of Fluids*, vol. 20, no. 10, p. 101511, 2008.

[71] R. I. Issa, "Solution of the implicitly discretised fluid flow equations by operator-splitting," *Journal of computational physics*, vol. 62, no. 1, pp. 40–65, 1986.

[72] P. Moin and J. Kim, "Numerical investigation of turbulent channel flow," *Journal of fluid mechanics*, vol. 118, pp. 341–377, 1982.

[73] J. L. Lumley, "The structure of inhomogeneous turbulent flows," *Atmospheric turbulence and radio wave propagation*, 1967.

[74] H. V. Fuchs, E. Mercker, and U. Michel, "Large-scale coherent structures in the wake of axisymmetric bodies," *Journal of Fluid Mechanics*, vol. 93, no. 1, pp. 185–207, 1979.

[75] S. Gamard, W. K. George, D. Jung, and S. Woodward, "Application of a "slice" proper orthogonal decomposition to the far field of an axisymmetric turbulent jet," *Physics of Fluids*, vol. 14, no. 7, pp. 2515–2522, 2002.

[76] J. H. Citriniti and W. K. George, "Reconstruction of the global velocity field in the axisymmetric mixing layer utilizing the proper orthogonal decomposition," *Journal of Fluid Mechanics*, vol. 418, pp. 137–166, 2000.

[77] H. Sakamoto and H. Haniu, "A study on vortex shedding from spheres in a uniform flow," *Journal of Fluids Engineering*, vol. 112, pp. 386–392, 12 1990.

[78] G. Yun, D. Kim, and H. Choi, "Vortical structures behind a sphere at subcritical Reynolds numbers," *Physics of Fluids*, vol. 18, no. 1, p. 015102, 2006.

[79] I. Rodriguez, O. Lehmkuhl, M. Soria, S. Gómez, M. Domínguez-Pumar, and L. Kowalski, "Fluid dynamics and heat transfer in the wake of a sphere," *International Journal of Heat and Fluid Flow*, vol. 76, pp. 141–153, 2019.

[80] H. Kim and P. Durbin, "Observations of the frequencies in a sphere wake and of drag increase by acoustic excitation," *Physics of fluids*, vol. 31, no. 11, pp. 3260–3265, 1988.

[81] Y. Bazilevs, J. Yan, M. De Stadler, and S. Sarkar, "Computation of the flow over a sphere at $Re = 3700$: A comparison of uniform and turbulent inflow conditions," *Journal of Applied Mechanics*, vol. 81, no. 12, 2014.

[82] A. Pal, S. Sarkar, A. Posa, and E. Balaras, "Direct numerical simulation of stratified flow past a sphere at a subcritical Reynolds number of 3700 and moderate Froude number," *Journal of Fluid Mechanics*, vol. 826, p. 5–31, 2017.

[83] K. Chongsiripinyo, A. Pal, and S. Sarkar, "On the vortex dynamics of flow past a sphere at $Re = 3700$ in a uniformly stratified fluid," *Physics of Fluids*, vol. 29, no. 2, p. 020704, 2017.

[84] E. Achenbach, "Vortex shedding from spheres," *Journal of Fluid Mechanics*, vol. 62, no. 2, pp. 209–221, 1974.

[85] S. Taneda, "Visual observations of the flow past a sphere at Reynolds numbers between 10^4 and 10^6," *Journal of Fluid Mechanics*, vol. 85, no. 1, pp. 187–192, 1978.

[86] P. B. Johansson and W. K. George, "The far downstream evolution of the high-Reynolds-number axisymmetric wake behind a disk. Part 2. Slice proper orthogonal decomposition," *journal of Fluid Mechanics*, vol. 555, pp. 387–408, 2006.

[87] G. Berkooz, P. Holmes, and J. L. Lumley, "The proper orthogonal decomposition in the analysis of turbulent flows," *Annual review of fluid mechanics*, vol. 25, no. 1, pp. 539–575, 1993.

[88] A. Towne, O. T. Schmidt, and T. Colonius, "Spectral proper orthogonal decomposition and its relationship to dynamic mode decomposition and resolvent analysis," *Journal of Fluid Mechanics*, vol. 847, pp. 821–867, 2018.

[89] G. Rigas, A. Oxlade, A. Morgans, and J. Morrison, "Low-dimensional dynamics of a turbulent axisymmetric wake," *Journal of Fluid Mechanics*, vol. 755, 2014.

[90] G. Pavia, M. Varney, M. Passmore, and M. Almond, "Three dimensional structure of the unsteady wake of an axisymmetric body," *Physics of Fluids*, vol. 31, no. 2, p. 025113, 2019.

[91] H. G. Weller, G. Tabor, H. Jasak, and C. Fureby, "A tensorial approach to computational continuum mechanics using object-oriented techniques," *Computers in physics*, vol. 12, no. 6, pp. 620–631, 1998.

[92] P. Welch, "The use of fast Fourier transform for the estimation of power spectra: a method based on time averaging over short, modified periodograms," *IEEE Transactions on audio and electroacoustics*, vol. 15, no. 2, pp. 70–73, 1967.

[93] S. Kawai and J. Larsson, "Wall-modeling in large eddy simulation: Length scales, grid resolution, and accuracy," *Physics of Fluids*, vol. 24, no. 1, p. 015105, 2012.

[94] S. T. Bose and G. I. Park, "Wall-modeled large-eddy simulation for complex turbulent flows," *Annual Review of Fluid Mechanics*, vol. 50, pp. 535–561, 2018.

[95] C. B. da Silva, J. C. Hunt, I. Eames, and J. Westerweel, "Interfacial layers between regions of different turbulence intensity," *Annual review of fluid mechanics*, vol. 46, pp. 567–590, 2014.

[96] Y. I. Jang and S. J. Lee, "PIV analysis of near-wake behind a sphere at a subcritical Reynolds number," *Experiments in Fluids*, vol. 44, no. 6, pp. 905–914, 2008.

[97] C. Kamble, P. Razi, P. Tazraei, and S. Girimaji, "Scale resolving simulations of turbulence: Closure modeling in near-wall region of steep resolution variation," *Manuscript submitted*, 2021.

APPENDIX A

WM-PANS: DERIVATION OF UNRESOLVED KINETIC ENERGY (k_u) EQUATION

Following the methodology proposed in Ref. [31] for uniform f_k, we begin with the RANS k equation and multiply it with a spatio-temporally varying f_k.

$$f_k\left(\frac{\partial k}{\partial t}+\overline{U_j}\frac{\partial k}{\partial x_j}=P-\beta^* k\omega+\frac{\partial}{\partial x_j}\left[(\nu+\nu_t/\sigma_k)\frac{\partial k}{\partial x_j}\right]\right) \tag{A.1}$$

Here, $\overline{U_j}$ is the Reynolds-averaged (or mean) velocity. Applying f_k to each term in the equation, we get

$$f_k\left(\frac{\partial k}{\partial t}+\overline{U_j}\frac{\partial k}{\partial x_j}\right)=f_k(P-\beta^* k\omega)+f_k\left(\frac{\partial}{\partial x_j}\left[(\nu+\nu_t/\sigma_k)\frac{\partial k}{\partial x_j}\right]\right) \tag{A.2}$$

The advective term evolves as:

$$f_k\left(\frac{\partial k}{\partial t}+\overline{U_j}\frac{\partial k}{\partial x_j}\right)=\frac{\partial k_u}{\partial t}+U_j\frac{\partial k_u}{\partial x_j}-k\left(\frac{\partial f_k}{\partial t}+\overline{U_j}\frac{\partial f_k}{\partial x_j}\right)+(\overline{U_j}-U_j)\frac{\partial k_u}{\partial x_j} \tag{A.3}$$

where the P_{Tr} term is defined as:

$$P_{Tr}\equiv\frac{k_u}{f_k}\left(\frac{\partial f_k}{\partial t}+\overline{U_j}\frac{\partial f_k}{\partial x_j}\right) \tag{A.4}$$

Assuming the resolved fluctuations don't contribute to sub-filter stress transport, the final term $(\overline{U_j}-U_j)\frac{\partial k_u}{\partial x_j}$ can be neglected [31]. Further, according to the results of Ref. [41], $\sigma_{ku}=\frac{f_k}{f_\omega}\sigma_{k,RANS}$. Therefore, we can write ν_t/σ_k as ν_u/σ_{ku} where $\nu_u=(f_k/\ f_\omega)\nu_t$. Now, let $\nu_u^*=\nu+\nu_u/\ \sigma_{ku}$, then the diffusion term can be written as,

$$f_k\left(\frac{\partial}{\partial x_k}\left[\nu_u^*\frac{\partial k}{\partial x_k}\right]\right)=\frac{\partial}{\partial x_k}\left[\nu_u^*\frac{\partial k_u}{\partial x_k}\right]-2\nu_u^*\frac{\partial k}{\partial x_j}\frac{\partial f_k}{\partial x_j}-\frac{k_u}{f_k}\frac{\partial}{\partial x_j}\left(\nu_u^*\frac{\partial f_k}{\partial x_j}\right) \tag{A.5}$$

which leads to,

$$f_k\left(\frac{\partial}{\partial x_k}\left[\nu_u^*\frac{\partial k}{\partial x_k}\right]\right)=\frac{\partial}{\partial x_k}\left[\nu_u^*\frac{\partial k_u}{\partial x_k}\right]-\frac{2\nu_u^*}{f_k^2}\frac{\partial f_k}{\partial x_j}\left(f_k\frac{\partial k_u}{\partial x_j}-k_u\frac{\partial f_k}{\partial x_j}\right)-\frac{k_u}{f_k}\frac{\partial}{\partial x_j}\left(\nu_u^*\frac{\partial f_k}{\partial x_j}\right) \quad \text{(A.6)}$$

Therefore, the diffusion term can be written as

$$f_k\left(\frac{\partial}{\partial x_k}\left[\nu_u^*\frac{\partial k}{\partial x_k}\right]\right)=\frac{\partial}{\partial x_k}\left[\nu_u^*\frac{\partial k_u}{\partial x_k}\right]+D_{Tr} \quad \text{(A.7)}$$

where the commutation residue due to the diffusion term is derived as:

$$D_{Tr}\equiv-\frac{k_u}{f_k}\frac{\partial}{\partial x_j}\left(\nu_u^*\frac{\partial f_k}{\partial x_j}\right)-\frac{2\nu_u^*}{f_k}\left(\frac{\partial k_u}{\partial x_j}-\frac{k_u}{f_k}\frac{\partial f_k}{\partial x_j}\right)\frac{\partial f_k}{\partial x_j};\;\; \nu_u^*=\nu+\frac{\nu_u}{\sigma_{ku}} \quad \text{(A.8)}$$

The remaining production, dissipation and transport terms are modeled according to the framework outlined in Ref. [31]. The final unresolved kinetic energy (k_u) equation is:

$$\frac{\partial k_u}{\partial t}+U_j\frac{\partial k_u}{\partial x_j}=P_u-\beta^* k_u\omega_u+P_{Tr}+D_{Tr}+\frac{\partial}{\partial x_j}\left[\left(\nu+\nu_u/\sigma_{ku}\right)\frac{\partial k_u}{\partial x_j}\right] \quad \text{(A.9)}$$

APPENDIX B

WM-PANS: DERIVATION OF UNRESOLVED SPECIFIC DISSIPATION RATE (ω_u) EQUATION

The unresolved dissipation (ε_u) remains unaffected due to spatial variations of f_k if the cut-off is outside the dissipation range [39]. Therefore, in order to derive the specific rate of dissipation (ω_u) equation, a transformation from the ε_u equation is needed. The evolution equation for the unresolved dissipation (ε_u) is [31]:

$$\frac{\partial \varepsilon_u}{\partial t} + U_j \frac{\partial \varepsilon_u}{\partial x_j} = C_{e1} \frac{P_u \varepsilon_u}{k_u} - C_{e2}^* \frac{\varepsilon_u^2}{k_u} + \frac{\partial}{\partial x_j} \left[(\nu + \nu_u/\sigma_{\varepsilon u}) \frac{\partial \varepsilon_u}{\partial x_j} \right] \tag{B.1}$$

Now, using the relation $\varepsilon_u = \beta^* k_u \omega_u$, the above equation can be transformed as:

$$\frac{\partial \beta^* k_u \omega_u}{\partial t} + U_j \frac{\partial \beta^* k_u \omega_u}{\partial x_j} = C_{e1} \frac{P_u \beta^* k_u \omega_u}{k_u} - C_{e2}^* \frac{(\beta^* k_u \omega_u)^2}{k_u} + \frac{\partial}{\partial x_j} \left[(\nu + \nu_u/\sigma_{\varepsilon u}) \frac{\partial \beta^* k_u \omega_u}{\partial x_j} \right] \tag{B.2}$$

Simplifying, we get,

$$\frac{\partial k_u \omega_u}{\partial t} + U_j \frac{\partial k_u \omega_u}{\partial x_j} = C_{e1} P_u \omega_u - C_{e2}^* \beta^* k_u \omega_u^2 + \frac{\partial}{\partial x_j} \left[(\nu + \nu_u/\sigma_{\varepsilon u}) \frac{\partial k_u \omega_u}{\partial x_j} \right] \tag{B.3}$$

Assuming $P_{ut} = P_u + P_{Tr} + D_{Tr}$ and adding $-P_{ut}\omega_u + \varepsilon_u \omega_u$ to both sides, we can simplify the advective terms on the left hand side as:

$$\frac{\partial k_u \omega_u}{\partial t} + U_j \frac{\partial k_u \omega_u}{\partial x_j} - P_{ut}\omega_u + \varepsilon_u \omega_u = k_u \left(\frac{\partial \omega_u}{\partial t} + U_j \frac{\partial \omega_u}{\partial x_j} \right) + \omega_u \left(\frac{\partial k_u}{\partial t} + U_j \frac{\partial k_u}{\partial x_j} - P_{ut} + \varepsilon_u \right) \tag{B.4}$$

From Eq. A.9, we get

$$\frac{\partial k_u \omega_u}{\partial t} + U_j \frac{\partial k_u \omega_u}{\partial x_j} - P_{ut}\omega_u + \varepsilon_u \omega_u = k_u \left(\frac{\partial \omega_u}{\partial t} + U_j \frac{\partial \omega_u}{\partial x_j} \right) + \omega_u \left((\nu + \nu_u/\sigma_{ku}) \frac{\partial k_u}{\partial x_j} \right) \tag{B.5}$$

Similarly, the transport terms in the right hand side of Eq. B.3 are simplified as:

$$\begin{aligned}\frac{\partial}{\partial x_j}\left[(\nu+\nu_u/\sigma_{\varepsilon u})\frac{\partial k_u\omega_u}{\partial x_j}\right] &= \frac{\partial}{\partial x_j}\left[(\nu+\nu_u/\sigma_{\varepsilon u})k_u\frac{\partial \omega_u}{\partial x_j}+(\nu+\nu_u/\sigma_{\varepsilon u})\omega_u\frac{\partial k_u}{\partial x_j}\right]\\ &= \frac{\partial}{\partial x_j}\left[(\nu+\nu_u/\sigma_{\varepsilon u})k_u\frac{\partial \omega_u}{\partial x_j}\right]+\frac{\partial}{\partial x_j}\left[(\nu+\nu_u/\sigma_{\varepsilon u})\omega_u\frac{\partial k_u}{\partial x_j}\right]\\ &= 2(\nu+\nu_u/\sigma_{\varepsilon u})\frac{\partial k_u}{\partial x_j}\frac{\partial \omega_u}{\partial x_j}+k_u\frac{\partial}{\partial x_j}\left[(\nu+\nu_u/\sigma_{\varepsilon u})\frac{\partial \omega_u}{\partial x_j}\right]\\ &+\omega_u\frac{\partial}{\partial x_j}\left[(\nu+\nu_u/\sigma_{\varepsilon u})\frac{\partial k_u}{\partial x_j}\right]\end{aligned} \tag{B.6}$$

Substituting in Eq. B.3, we get,

$$\begin{aligned}k_u\left(\frac{\partial \omega_u}{\partial t}+U_j\frac{\partial \omega_u}{\partial x_j}\right) &= C_{e1}P_u\omega_u-C^*_{e2}\beta^*k_u\omega_u^2-P_{ut}\omega_u+\beta^*k_u\omega_u\omega_u\\ &+2(\nu+\nu_u/\sigma_{\varepsilon u})\frac{\partial k_u}{\partial x_j}\frac{\partial \omega_u}{\partial x_j}+k_u\frac{\partial}{\partial x_j}\left[(\nu+\nu_u/\sigma_{\varepsilon u})\frac{\partial \omega_u}{\partial x_j}\right]\end{aligned} \tag{B.7}$$

Rearranging the terms in the above equation,

$$\begin{aligned}\frac{\partial \omega_u}{\partial t}+U_j\frac{\partial \omega_u}{\partial x_j} &= (C_{e1}-1)\frac{P_u\omega_u}{k_u}-\frac{(P_{Tr}+D_{Tr})\omega_u}{k_u}-(C^*_{e2}-1)\beta^*\omega_u^2\\ &+\frac{\partial}{\partial x_j}\left[(\nu+\nu_u/\sigma_{\varepsilon u})\frac{\partial \omega_u}{\partial x_j}\right]+\frac{2}{k_u}(\nu+\nu_u/\sigma_{\varepsilon u})\frac{\partial k_u}{\partial x_j}\frac{\partial \omega_u}{\partial x_j}\end{aligned} \tag{B.8}$$

The additional term arising due to spatial variation of f_k in the ω_u equation is $D_{Tr\omega}=-(P_{Tr}+D_{Tr})\omega_u/\,k_u$. Therefore, the final ω_u equation in the PANS $k_u-\omega_u$ model [62] is modified as:

$$\frac{\partial \omega_u}{\partial t}+U_j\frac{\partial \omega_u}{\partial x_j}=\alpha\frac{P_u\omega_u}{k_u}+D_{Tr\omega}-\beta'\omega_u^2+\frac{\partial}{\partial x_j}\left[(\nu+\nu_u/\sigma_{\omega u})\frac{\partial \omega_u}{\partial x_j}\right] \tag{B.9}$$